

Dissertation

submitted to the
Combined Faculties for Natural Sciences and for Mathematics
of the Ruperto-Carola University of Heidelberg, Germany
for the degree of
Doctor of Natural Sciences

presented by

Dipl.–Phys. Matthias Stute
born in Münster/Westphalia, Germany

Oral examination: October 22nd, 2004

Formation and Propagation of Jets in Symbiotic Stars

Referees:

Professor Dr. Max Camenzind

Privatdozent Dr. Hans Martin Schmid

Abstract

Although jets are ubiquitous phenomena in many different astrophysical objects, their formation is relatively unclear. The necessary components seem to be well known and identical in all objects. A more careful investigation of one certain class of objects should promise new insights also for the mechanisms in the other classes. From the observational point of view, one needs observations with a high spatial resolution and kinematic informations from regions as near as possible to the jet source. These points make the class of symbiotic stars, interacting binaries consisting of a cool red giant (RG) and a white dwarf (WD), ideal testbeds.

In the first part of this thesis the propagation of the jet in the unique system MWC 560, where the jet axis is practically parallel to the line of sight, is investigated numerically. This special orientation provides the opportunity to observe the outflowing gas as line absorption in the source spectrum. Therefore MWC 560 can be used to probe the short term evolution and the propagation of the gas outflow in jets from WD. We present model results concerning the structure and emission of the jets and theoretical absorption line profile which are compared with observations of MWC 560.

In the second part, we focus on the formation and collimation process of jets from WD. We mainly investigate the effect of a solid surface of the central, accreting object and of the creation of a boundary layer around it.

Zusammenfassung

Obwohl Jets allgegenwärtig in vielen verschiedenen astrophysikalischen Objekten sind, ist ihre Bildung relativ unverstanden. Die notwendigen Komponenten scheinen gut bekannt und identisch in allen Objekten zu sein. Eine genauere Untersuchung einer einzigen Klasse von Objekten sollte neue Einsichten auch für die Mechanismen in den anderen liefern. Vom Standpunkt eines Beobachters, benötigt man eine hohe räumliche Auflösung und kinematische Informationen, möglichst nahe an der Jetquelle. Dies macht die Klasse der Symbiotischen Sterne, Binärsysteme bestehend aus einem Roten Riesen (RG) und einem Weißen Zwerg (WZ), zu idealen Prüfständen.

Im ersten Teil der Arbeit wird die Ausbreitung des Jets im einzigartigen System MWC 560, bei dem die Jetachse praktisch parallel zur Sichtlinie liegt, numerisch untersucht. Diese besondere Ausrichtung ermöglicht die Beobachtung des ausströmenden Gases in Absorptionslinien. MWC 560 kann somit als Sonde der kurzzeitigen Entwicklung und Ausbreitung von Jets um WZ benutzt werden. Wir zeigen Resultate der Struktur und Emission der Jets und theoretische Absorptionslinienprofile, die mit Beobachtungen von MWC 560 verglichen werden.

Im zweiten Teil konzentrieren wir uns auf die Bildung und Kollimation der Jets um WZ. Hauptsächlich untersuchen wir den Effekt einer festen Oberfläche des zentralen, akkretierenden Objekts sowie der Bildung eines Boundary Layers um dieses.

Contents

1	Introduction	11
1.1	What's all about	11
1.2	Structure of this thesis	13
2	Symbiotic Stars and their Jets	15
2.1	Historical remarks	15
2.2	Classification of Symbiotic Stars	15
2.3	Theoretical models of Symbiotic Stars	16
2.4	Jets in Symbiotic Stars	17
2.4.1	The Object R Aquarii	17
2.4.2	The Object CH Cygni	17
2.4.3	The Object MWC 560	19
2.5	Observations of MWC 560 in detail	20
2.5.1	Parameters of the binary system	20
2.5.2	The velocity structures	21
2.5.3	First interpretations	22
3	The Models of propagating Jets	26
3.1	Geometric model	26
3.2	Parameters for the pulsed jet	27
3.3	A model with Cooling	28
3.4	Structure of the jets	29
3.4.1	Adiabatic jet models	29
	Bow shock geometry	29
	Internal jet structure	30
	Radial profiles	36
3.4.2	The model with radiative cooling	43
	Bow shock evolution	43
	Internal structure	43
	Radial profiles	43
3.5	Emission of the jets	48
3.5.1	Adiabatic jet models	48
3.5.2	The model with radiative cooling	51
3.6	Discussion I	53
3.6.1	Model calculations	53
3.6.2	Comparison with symbiotic systems	54
4	Theoretical absorption line profiles	56
4.1	Model calculation	56
4.1.1	Absorption profiles	56
4.1.2	Model parameters	59
4.2	Results for different model parameters	59

4.2.1	Size of the emission region and system inclination	59
4.2.2	The velocity bin size	61
4.2.3	The ionization problem	64
4.3	Time variability of the absorption line	64
4.4	Jet absorption profile: comparison with observations	68
4.4.1	Jet absorption profile	68
4.4.2	Structure and evolution of the high velocity absorptions	69
4.5	Discussion II	69
5	Large scale simulations	74
5.1	The numerical models	74
5.2	Validating the cooling treatment	74
5.3	Jet structure	76
5.3.1	Bow shock geometry and evolution	76
5.3.2	Internal jet structure	76
5.3.3	Radial profiles	78
5.4	Jet emission	78
5.5	The absorption line profiles	81
5.6	Discussion III	81
6	Jet formation in white dwarf systems	87
6.1	Formation of jets by MHD processes	87
6.1.1	Approaching the problem	88
6.1.2	Jet formation scenarios	89
6.2	Formation of jets by thermal pressure in <i>SPLASHs</i>	92
6.3	Estimates and reliability	93
6.3.1	The magnetic model	95
6.3.2	The pressure model	96
6.3.3	The outburst period of pulsed jet formation	96
7	Simulations of Jet Formation	97
7.1	Attempts to reproduce the results of Casse & Keppens (2002)	97
7.1.1	Initial conditions	97
7.1.2	Boundary conditions	99
7.2	Torus simulations	100
7.2.1	Initial conditions	100
7.2.2	The effect of a solid surface onto the jet formation process	101
The accretion and ejection components	103	
The jet emission efficiency	103	
Structure of the accretion flow	104	
7.2.3	Structure of the BL ejection component	105
7.3	Implications for symbiotic stars	105
8	Discussion and Outlook	110
8.1	What we have done	110
8.2	What we have to do	111
A	The numerical codes	113
A.1	NIRVANA_C	113
A.2	NIRVANA2.0	114
B	Publications	115
	List of Figures	117

List of Tables	119
Bibliography	121
Danksagung	127

Chapter 1

Introduction

1.1 What's all about

Jets are highly collimated plasma outflows with high (supersonic) velocities. They are phenomena which are very common in a variety of astrophysical objects on very different size and mass scales. They can be produced by supermassive black holes in the case of active galactic nuclei (AGN, Fig. 1.1, left), by stellar black holes in black hole X-ray binaries (BHXBs), by neutron stars in X-ray binaries, by pre-main sequence stars in young stellar objects (YSO, Fig. 1.1, right) – and by white dwarfs in symbiotic binaries.

Symbiotic Stars are interacting binaries with orbital periods in the range of years. These systems show outbursts similar to classical novae. The stellar component is a cool Red Giant (RG), the hot component a White Dwarf (WD) with temperatures of 50000 – 200000 K. Both stars show mass loss through supersonic winds. Wind material from the RG is captured by the WD to form an accretion disc. The accretion then causes thermonuclear explosions of the WD surface leading to an increase in magnitude followed by jet emission. A sketch of symbiotic star system can be found in Fig. 1.2.

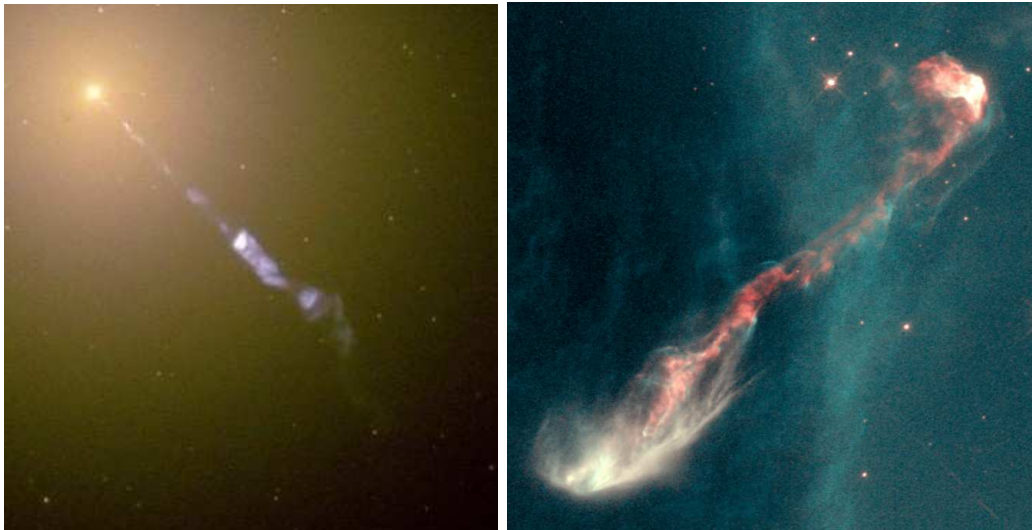


Figure 1.1: Examples of astrophysical jets; an extragalactic jet in Messier 87 (left) and a protostellar jet in HH 47 (right); Courtesy: Hubble Heritage



Figure 1.2: Sketch showing all constituents of a symbiotic star system; Courtesy: Instituto de Astrofísica de Canarias and Romano Corradi (Isaac Newton Group of Telescopes)

Up to now, theoretical investigations – concerning the propagation as well as their formation – has been confined to the first cases, jets in symbiotic systems are neglected in numerical simulations of jets. The first two-dimensional numerical study of propagating jets was done by Rayburn (1977), which was a pioneering starting point of a new era. In the following years, triggered by improved computational opportunities, this research area quickly expanded. Norman et al. (1982, 1983) performed studies varying the three fundamental jet parameters density contrast $\eta = \rho_{\text{jet}}/\rho_{\text{ambient}}$, Mach number $M = v_{\text{jet}}/c_s$ and pressure contrast $K = p_{\text{jet}}/p_{\text{ambient}}$. The latter is often set to unity, as observations do not show contraction or expansion. They established the now valid picture of astrophysical jets consisting of the supersonic jet beam, the terminal shock (bow shock) and the cocoon. Three-dimensional simulations followed soon (e.g. Williams & Gull 1985). In the same time period, also magnetohydrodynamical effects were first considered by Clarke, Norman & Burns (1986). Blondin, Fryxell & Königl (1990) performed the first simulations with cooling included, intended to investigate protostellar jets and the formation of Herbig-Haro (HH) objects. A good review of the mentioned simulations, their parameter regimes and their results was given by M. L. Norman in Burgarella et al. (1993).

All these simulations are examinations of extragalactic or protostellar jets. Due to the fact, that their parameters are in a different regime compared to those in symbiotic stars, studying the latter should promise new insights. The density contrast η is about $10^{-3} - 10^{-2}$ in symbiotic stars (e.g. Kenyon 1986; Schmid et al. 2001) while $\eta = 1 - 10$ in YSO (e.g. Mundt, Brugel & Bührke 1987) and therefore similar to those in AGN (e.g. Scheck et al. 2002, and references therein). The outflow velocities are, however, similar to those in YSO of $100 - 1000 \text{ km s}^{-1}$ (e.g. Garcia et al. 2001; Paresce & Hack 1994), while of the order of c in black hole systems (e.g. Mirabel & Rodríguez 1999). Their absolute densities of $10^6 - 10^9 \text{ cm}^{-3}$ (e.g. Schmid et al. 2001) are much higher than in the other objects ($10^3 - 10^4 \text{ cm}^{-3}$ in YSO, $10^{-2} - 10^6 \text{ cm}^{-3}$ in AGN, e.g. Bacciotti 1997; Scheck et al. 2002, and references therein), a fact which makes cooling effects much more important.

Further reasons why jets in symbiotic systems are of special interest in comparison with the other jet sources are:

- the underlying physics of the jet formation and propagation should be the same in principle, in spite of the different parameters
- there is an intense mass loss from the late red giant
- a large amount of circumstellar material is present, therefore the interaction of the jet with its environment can be studied.

Unfortunately, the last point is also a disadvantage, because the circumstellar material with its emission is mostly too bright. Therefore jets in Symbiotic Stars are detected so far only in systems with lower nebular luminosity.

From the observational point of view, one needs observations with a high spatial resolution and kinematic informations from regions as near as possible to the jet source. This points make the class of symbiotic stars ideal testbeds, as they are among the nearest known jet sources. Furthermore a more careful investigation of one certain class of objects should provide new insights also for the mechanisms of propagation and formation of jets in the other classes.

To find these new effects and new results is the aim of the first part of this thesis.

Although jets are ubiquitous in astrophysics, often observed providing a large amount of data, their formation is relatively unclear. The mass loss rate of the jet is found to be connected to the mass accretion rate of the underlying disc found in most objects. Therefore the necessary components seem to be well known and identical in all objects. The mostly accepted mechanism is magneto-centrifugal acceleration according to Blandford & Payne (1982). However, the details of jet formation are still nebulous. A recently proposed scenario goes without the existence of large magnetic fields, assuming that the material is accelerated due to thermal pressure inside a boundary layer (BL) around the central object with a solid surface (Soker & Regev 2003) and is only collimated by smaller magnetic fields. This scenario was introduced in analytic estimates and now has to be verified qualitatively and quantitatively in numerical simulations.

The BL is the region in which the accreting matter is decelerated from its Keplerian rotation to the much smaller stellar rotation and which is likely in weakly magnetized Neutron Stars and White Dwarfs. It is a relatively small, but hot region which is optically thick at high and optically thin at low accretion rates. The rotational support against gravity is replaced by thermal pressure. Up to one half of the gain in potential energy is radiated in this small region – the other half has been already lost in the accretion disc. The structure of BLs was investigated in semi-analytic and numerical one- dimensional stationary models (Popham & Sunyaev 2001, and references therein), as well as in two-dimensional time-dependant numerical simulations (e.g. Steinacker & Papaloizou 2002; Armitage 2002), but without considering a mass outflow.

To find its advantages or disadvantages in comparison with the scenario of magnetically driven jets, is then our goal in the last chapters. We want to perform investigations of jets in symbiotic stars from their formation on scales of a few solar radii to their propagation into the interstellar medium on scales of a few hundreds of AU.

1.2 Structure of this thesis

In chapter 2, we describe the class of symbiotic stars, their classification and models of them. After that we introduce the most famous jet sources among them, which serve as template for our simulations of jet propagation in the case of MWC 560 and for comparison in the cases of R Aqr and CH Cyg. Due to the special role of MWC 560 for our studies, we investigate the observational data, available for it, in a more detailed way in section 2.5. We cite model parameters and first interpretations, which are used to build our models described in chapter 3. In the following two sections 3.4 and 3.5, we then present the first results obtained from our simulations, namely the global structure of the jets and their emission, respectively. In chapter 4, we calculate synthetical

absorption line profiles and compare them with the observed ones, which are the observations of MWC 560 with the largest content of information. In the first generation of simulations, we were limited by computational constraints. With reduced efforts to calculate the radiative cooling, we were then able to perform largescale simulations of the jets, which are presented and compared with our former results in chapter 5.

Up to then, we focused on the propagation of jets in symbiotic stars. In the following chapters, we intend to examine the process of jet formation and collimation. In chapter 6, we introduce the theory of jet formation, different jet formation scenarios and observational hints for our class of jet sources. They triggered our simulations of jet formation, which are presented in chapter 7.

Finally, a discussion and outlook are given.

Chapter 2

Symbiotic Stars and their Jets

2.1 Historical remarks

Beside “normal” stars having very simple spectra with a bright continuum and few absorption lines, Fleming (1912) detected stars whose spectra have bright emission lines in addition to or in place of the absorption features. He published the first list of these “stars with peculiar spectra” and categorized them into

1. novae
2. O-type stars
3. stars with bright hydrogen lines
4. long-period variables .

Seven years later, Merrill (1919) investigated the long-period variable R Aqr with one of the first systematic spectroscopic studies. He found [O III] lines – characteristic for planetary nebulae – and the spectrum of a Md variable with strong TiO absorption bands and sharp, bright H I lines. From 1926 to 1933, strong emission lines of He II, C III and N III were observed in the spectrum of this object (Merrill 1936). During this period, the amplitude of the Mira-like brightness variations decreased, while the period of the oscillations remained unchanged. After disappearance of the lines of highly ionized gas, the M-type spectrum and normal Mira-like pulsations returned.

Plaskett (1928) identified in the spectrum of Z And two sources – a stellar one with narrow emission lines of Fe II, Ti II and other single ionized metals plus a nebula one with wider emission lines of He II, N III and [O III]. After the suggestion of Merrill, Hogg (1932) re-investigated Plaskett’s data and detected additionally TiO absorption bands.

Merrill & Humason (1932) discovered at Mt. Wilson Observatory three “stars with combination spectra” – CI Cyg, RW Hya and AX Per – with the TiO bands of M4 giant stars, an unusually strong He II $\lambda 4686$ emission line, Balmer lines as intense emission features and again nebular lines as [O III] and [Ne III] in CI Cyg and Ax Per. Each of these stars was found to be a long-period variable.

In the following years new objects were added to this group – some with the radial velocity signature of binary systems and some with the random fluctuations of single stars. Despite of the last point, all these systems are suspected to be binary stars. In 1941, Merrill introduced the term “symbiotic star”.

2.2 Classification of Symbiotic Stars

Most of the characteristic features of symbiotic stars were already given in section 2.1. The exact definition of this class highly depends of the choice of prototype stars. Merrill originally chose Z

And, BF Cyg, CI Cyg, RW Hya and AX Per as example stars, and therefore Y CrA, V443 Her, AR Pav and AG Peg had to be included. In the past fifty years, different authors tried to improve this sample by adding new criteria, but all of them were violated – at certain times – by all known symbiotic stars. The specific properties of the stars in the original sample are, according to Kenyon (1986),

1. absorption features of a *late-type giant star* (Ca I, Ca II, Na I, Fe I, H₂O, CN, CO, TiO, VO and others)
2. bright H I and He I *emission lines* with either
 - (a) additional *bright lines* of ions with an ionization potential > 20 eV and an equivalent width $> 1 \text{ \AA}$, or
 - (b) an A- or F-type continuum with additional *absorption lines* from H I, He I and single ionized metals (outburst state) .

Until today, around 200 symbiotic stars were found (see e.g. Kenyon 1986, or the AAVSO database). Their spatial distribution is concentrated to the galactic plane which suggests that they are members of the intermediate or old disk population. No symbiotic stars associated with star clusters were discovered. Recently, also extragalactic symbiotic stars were identified: five in the Magellanic Clouds and one in the Draco dwarf galaxy.

2.3 Theoretical models of Symbiotic Stars

The first authors who explained the combination spectra – a bright red continuum, strong TiO absorption bands, prominent high ionization emission lines and a weak blue continuum – with a binary system were Berman (1932) and Hogg (1934). They suggested an M-type giant with a faint O- or B-type companion star (like in *o Ceti*). The companion would produce the weak blue continuum and the emission-line region would be a surrounding nebula. They explained the small line fluctuations with the binary motion and the larger flares with instabilities in the hot source.

Kuiper (1940) introduced another system consisting of a normal main sequence star and a Roche lobe-filling companion. The matter falling from the giant onto its companion would then create a hot emission region. Here the flares would be due to instabilities in the *mass-losing* component.

As mentioned in section 2.1, not all symbiotic stars show the periodic variations of binary stars. Therefore alternatives with only a single star were developed. Menzel (1946) suggested an evolved long-period variable with a condensed stellar core to produce the emission lines and a cool atmosphere as absorber.

Other ideas were a normal red giant with an active corona or chromosphere, the same with a shock-heated corona or a K giant with a large star spot and the associated magnetic activity. These models, which try to explain the emission lines in these objects with a corona, can be excluded by X-ray observations and line ratio measurements of N V / C IV (Stencel et al. 1982).

The now commonly accepted model for symbiotic stars is a binary system consisting of a late-type giant star, a hot component and an ionized nebula. The hot component is thought to be either a hot stellar source as the central star of a planetary nebula, an accreting white dwarf or an accreting main sequence star. With theoretical arguments about the mass loss rates and energetics symbiotic stars can be divided into two categories – systems containing a lobe-filling giant and a low mass main sequence star and systems containing a white dwarf or sub-dwarf and a red giant losing mass through a stellar wind. The majority of all known symbiotic stars are of the second configuration (see again Fig. 1.2).

These systems are excellent laboratories to study e.g. the mass loss of the red giant, the formation of planetary nebulae, the accretion onto compact objects, the evolution of nova-like outbursts, the photoionization and radiative transfer within the nebulae.

2.4 Jets in Symbiotic Stars

Symbiotic binaries are a very heterogeneous class of objects, showing different types of nova-like activity. Jets are only expected in systems with substantial accretion from the red giant via a disk. The presence of a disk can be inferred from strong, short term (\sim hour) flickering of the hot component. However, flickering is only observed in very few objects (Sokoloski, Bildsten & Ho 2001). In many systems an accretion disk may not be visible due to the much stronger emission from the cool giant, the nebula or the accreting white dwarf. Further the disk may be hidden by a larger scale circumbinary disk. In some systems the jet emission seems to be a transient phenomenon, connected with an active phase of the hot component - perhaps due to an accretion disk instability. However, such transient features are difficult to study observationally.

More than hundred symbiotic stars are known, but only about ten systems show jet activity. The most famous systems are R Aquarii, CH Cyg and MWC 560, for which we summarize the main observational results in this section.

2.4.1 The Object R Aquarii

R Aquarii with a distance of about 200 pc is one of the nearest symbiotic stars and a well known jet source. The system contains a Mira-like variable with a pulsation period of 387 days. The hot, ionizing companion is not resolved, but it is presumably a white dwarf or sub-dwarf with an accretion disk. An orbital period of \approx 44 years has been suggested, but this value is highly uncertain (Wallerstein 1986). The system is seen at an inclination of around 70° . The jet has been extensively observed in the optical, at radio wavelengths and with X-ray observations (e.g. Solf & Ulrich 1985; Paresce & Hack 1994; Hollis et al. 1985a,b; Kellogg, Pedelty & Lyon 2001). R Aqr shows a jet and a counter-jet extending about $10''$ each. The jets are embedded in an extended and complex nebulosity. Individual jet features are morphologically and photometrically variable with time. In observations with HST (Fig. 2.1, Paresce & Hack 1994), the jet can be traced down to a distance of only 15 AU from the Mira where it is already collimated with an opening angle of $< 15^\circ$. After a straight propagation of 50 AU, it hits a dense clump and produces a radiative bow shock (feature N2; notation as in Paresce & Hack 1994). The flow stream extends around 700 AU towards feature A1, further a series of parallel features (N3 - N6) are detected downstream of N2, orthogonal to the original flow. HST observations taken at different epochs revealed that the transverse velocity (proper motion) of the different features increases from about 40 to 240 km s^{-1} with increasing distance from the central jet (Hollis et al. 1985b). In Chandra images (Kellogg, Pedelty & Lyon 2001), the knots are not as well resolved as in optical observations (Fig. 2.2). Only larger clumps are visible, corresponding to the central source M, the feature A1 and the feature S3 in Paresce & Hack (1994). VLA observations (Hollis et al. 1985a) show similar structures.

For R Aqr a major problem for the interpretation of the jet observations is the blending of jet features with emission from the surrounding nebulosity (Fig. 2.3, Solf & Ulrich 1985). Therefore it is not clear, whether the observed features are due to the jet gas, due to the ambient medium which is shock-excited by the jet outflow, or just circumstellar material ionized by the radiation from the accreting component.

2.4.2 The Object CH Cygni

CH Cygni is a binary where the hot component shows strong, short term flickering as expected for a bright accretion disk. The cool companion is an extended M6 III giant of $3 M_\odot$ with a radius of about $200 R_\odot$. The binary period is 5700 d (Crocker et al. 2002) and eclipses of the flickering component indicate a system inclination near 90° (Mikolajewski, Mikolajewska & Tomov 1987). In 1984/85, the system showed a strong radio outburst, during which a double-sided jet with multiple components was ejected (Fig. 2.4, Taylor, Seaquist & Mattei 1986). This event allowed an accurate measurement of the jet expansion with an apparent proper motion of 1.1 arcsec per year. Considering a distance of 268 pc (HIPPARCOS, Crocker et al. 2001), this leads to a jet velocity near 1500 km s^{-1} . The spectral energy distribution derived from the radio observations suggest

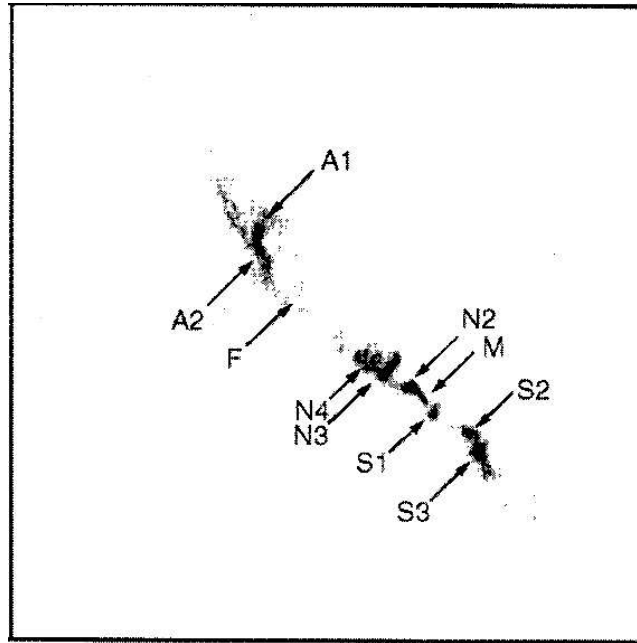


Figure 2.1: HST image of the jet and counter-jet of R Aquarii; the binary is located at feature M; adopted from Paresce & Hack (1994)

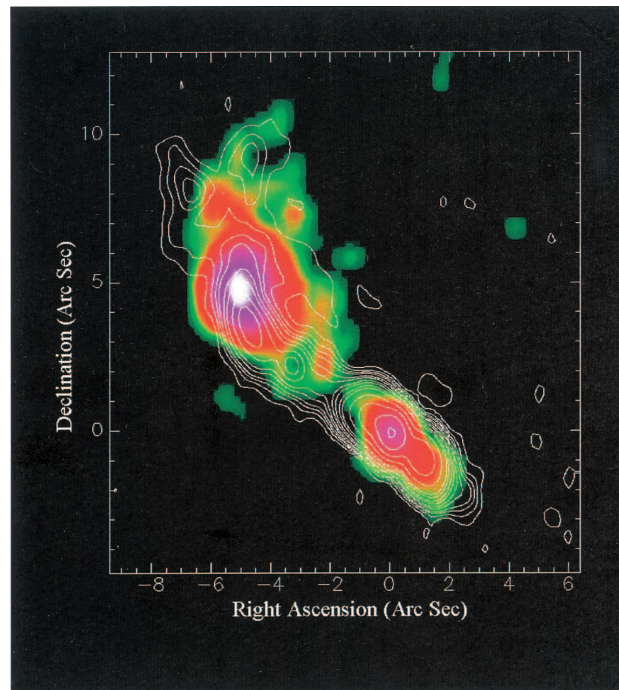


Figure 2.2: Chandra image of the jet and counter-jet of R Aquarii; adopted from Kellogg, Pedelty & Lyon (2001)

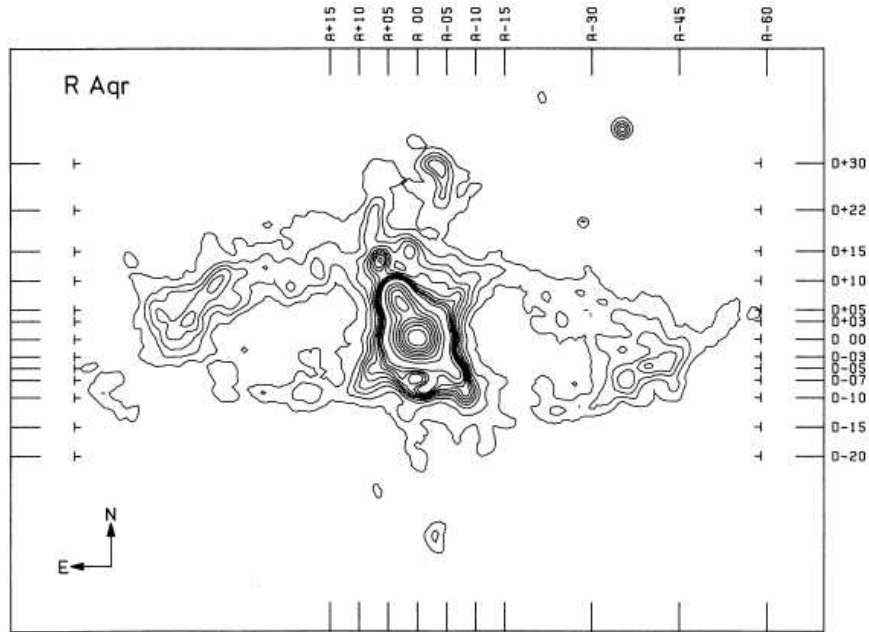


Figure 2.3: Outer and inner nebulosity around R Aquarii; adopted from Solf & Ulrich (1985)

a gas temperature of about 7000 K for the propagating jet gas (Taylor, Seaquist & Mattei 1986). HST observations (Eyres et al. 2002) show arcs, which could again be produced by episodic ejection events. The X-Ray spectrum taken with ASCA (Ezuka, Ishida & Makino 1998) is composed of three components which are associated with the hot source and the secondary or the radio jet. X-Ray imaging is not yet available.

2.4.3 The Object MWC 560

The first notice of the peculiar nature of the object MWC 560 was made by Merrill & Burwell (1943) in their catalogue of Be and Ae stars. They found emission lines of H I and Ca II K which have absorption features on their blue sides displaced by about 1000 km s^{-1} . Sanduleak & Stephenson (1973) also confirmed the presence of Balmer emission, blue shifted absorption and observed additionally TiO bands. Therefore this object was classified by them as a peculiar M4 emission line star. Bond et al. (1984) detected the blue shifted absorption to have complex structures extending to -3000 km s^{-1} . These structures were strongly variable on time scales of a day.

In early 1990, MWC 560 attracted attention with a photometric outburst of 2 mag. With spectroscopic observations it was found that the system exhibits strongly variable, blue shifted absorptions with outflow velocities (RV) up to 6000 km s^{-1} (Tomov et al. 1990). Unlike in normal P Cygni profiles from a stellar wind the blue absorption components are detached from the emission component. After the initial outburst phase the outflow showed a low velocity phase with a velocity of -300 km s^{-1} for about a year (Tomov & Kolev 1997; Buckley 1992). At the same time, the UV continuum was weakened by a zoo of absorption lines (Maran et al. 1991; Shore, Aufdenberg & Michalitsianos 1994). This pointed towards a highly increased density of the outflow. Since September 1991, the “normal” outflow mode was re-established, with strongly variable, detached absorption components and a typical outflow velocity of $\approx 1500 \text{ km s}^{-1}$ (Tomov & Kolev 1997).

The absorption line structure can be explained as a jet outflow whose axis is parallel to the line of sight (Tomov et al. 1990; Schmid et al. 2001). This very special system orientation is

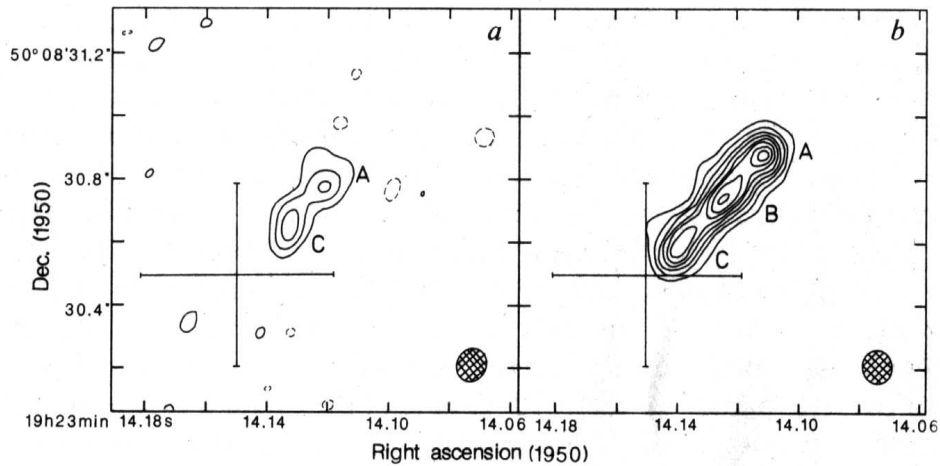


Figure 2.4: Multi-component jet of CH Cygni as observed in November 1984 and January 1985; adopted from Taylor, Seaquist & Mattei (1986)

supported by the absence of measurable radial velocity variations for the red giant indicating that the orbital plane and therefore presumably also the accretion disk are perpendicular to the line of sight. Moreover strong flickering is present as expected for an accretion disk of a strong jet source seen pole on. Up to now, this is the only stellar object known with this special jet orientation. Therefore MWC 560 is most useful for studying the acceleration and dynamical evolution of small scale structures in a stellar jet. Studying the variable gas absorptions yields information about the outflowing gas at very small distances < 10 AU from the source.

The jet gas dynamics in MWC 560 was investigated in detail during 56 nights between Nov. 1998 to Jan. 1999 by Schmid et al. (2001) with the high resolution FEROS echelle spectrograph at the ESO 1.52m telescope at La Silla. The observational data revealed highly variable absorption components from which the structure of the jet was determined. Schmid et al. (2001) also estimated various jet parameters for MWC 560 from the observations. In particular it was possible to derive values for the velocity and the gas density for the “normal” jet outflow, but also for phases with strong high velocity components. These determinations of hydrodynamical parameters of the initial jet gas in MWC 560 will serve as input parameter for the numerical simulations of the propagation of pulsed jets in symbiotic systems. These observations will be presented in the next chapter in a more detailed way.

2.5 Observations of MWC 560 in detail

Before describing the absorption structures in detail in section 2.5.2, the parameters of this system inferred from the observations of Schmid et al. (2001) need to be shown. They are important for setting free parameters of the models.

2.5.1 Parameters of the binary system

The orbital period of this object is not yet known. Mürset & Schmid (1999) derived an relation between the orbital period and the spectral type of the red giant using IR spectra. This relation and the measured spectral type of the red giant in MWC 560 (M5.5) portend to an orbital period larger than 840 days.

Schmid et al. (2001) detected a transient obscuration of the red giant by the jet in the H α absorption which could be interpreted as a periodic eclipse effect. The egress phase was only observed within about 2 months by Schmid et al. (2001), other observations of the He I λ 10831 line, made by Meier et al. (1996) in April 1990 and January 1991, showed a full duration of the eclipse of 10 months, and therefore the orbital period must be $P \approx 8.5$ years or an integer fraction of it.

Combining these two arguments, the possible values are 8.5, 4.25 and 2.83 years, but the last one can be excluded by the long duration of the eclipse event.

With the orbital period, an assumption of the masses of both stars and the third Kepler law one can estimate the binary separation by

$$a^3 = \frac{P^2 (m_{hc} + m_{rg}) G}{4 \pi^2}. \quad (2.1)$$

Assuming $2 M_{\odot}$ for the sum of the two masses this yields $a = 5.2$ AU for $P = 8.5$ yr and $a = 3.3$ AU for $P = 4.25$ yr.

An upper limit for the inclination of the jet and also of the orbital plane – assuming that both are perpendicular to each other – can be estimated by using radial velocity (RV) variations. The orbital velocities with respect to the center of mass can be calculated by

$$v_{hc} = \frac{2 \pi}{P} a \frac{m_{rg}}{m_{hc} + m_{rg}} \quad v_{rg} = \frac{2 \pi}{P} a \frac{m_{hc}}{m_{hc} + m_{rg}}. \quad (2.2)$$

With the maximum amplitude for the orbital RV variations δ for the red giant in MWC 560, the maximum inclination is

$$\sin i < \frac{\delta}{2 v_{rg}}. \quad (2.3)$$

From the observation follows the estimate $\delta = 2.5 \text{ km s}^{-2}$ (Schmid et al. 2001). Assuming $m_{hc} = m_{rg} = 1 M_{\odot}$, the maximum inclination is $i < 8^{\circ}$. With $m_{hc} = 0.5 M_{\odot}$ and $m_{rg} = 1.5 M_{\odot}$, the same calculation yields $i < 16^{\circ}$.

The spectral type of the red giant in MWC 560 was measured by different groups to M5.5 (Meier et al. 1996; Mürset & Schmid 1999). Several empirical relations between the spectral type and radius (Dumm & Schild 1998; van Belle et al. 1999) can be used to derive the size of the red giant. The radius is $140 \pm 40 R_{\odot}$ which corresponds to 0.65 ± 0.19 AU (Schmid et al. 2001).

The distance to the object MWC 560 can be derived from the radial velocity of interstellar absorption lines. Schmid et al. (2001) found that Na I and Ca II both have an absorption structure with four component at +14.1, +41.2, +49.1 and +66.3 km s^{-2} . Following Brand & Blitz (1993) the features at +41.2 km s^{-2} and +49.1 km s^{-2} show that the distance is $d \geq 2.5$ kpc. The last feature seems to be created by an absorbing cloud.

The IR-brightness of the assumed M5.5 III giant with its typical luminosity confirmed this value.

2.5.2 The velocity structures

During the campaigns mentioned in section 2.4.3, Schmid et al. (2001) detected highly variable absorption features which are very different from classical P Cygni profiles of stellar winds and which were interpreted as created by a jet outflow parallel to the line of sight (Tomov et al. 1990). They can be separated into three different components (Fig. 2.5). The first component is relatively stable with RV of $\approx -1200 \pm 300 \text{ km s}^{-1}$. In this absorption trough, saturation is visible in the H I Balmer lines over a wide velocity range. The metal lines (Na I, Fe II, Ca II) are not saturated and several subcomponents can be resolved. The residual flux in this range is always increasing or constant towards higher outflow velocities which indicates that gas of higher velocities covers the hot continuum source less than that with lower velocities. Focusing on the Na I line, one realizes that no absorptions with $\text{RV} \leq -1000 \text{ km s}^{-1}$ are present. This suggests that this low velocity gas

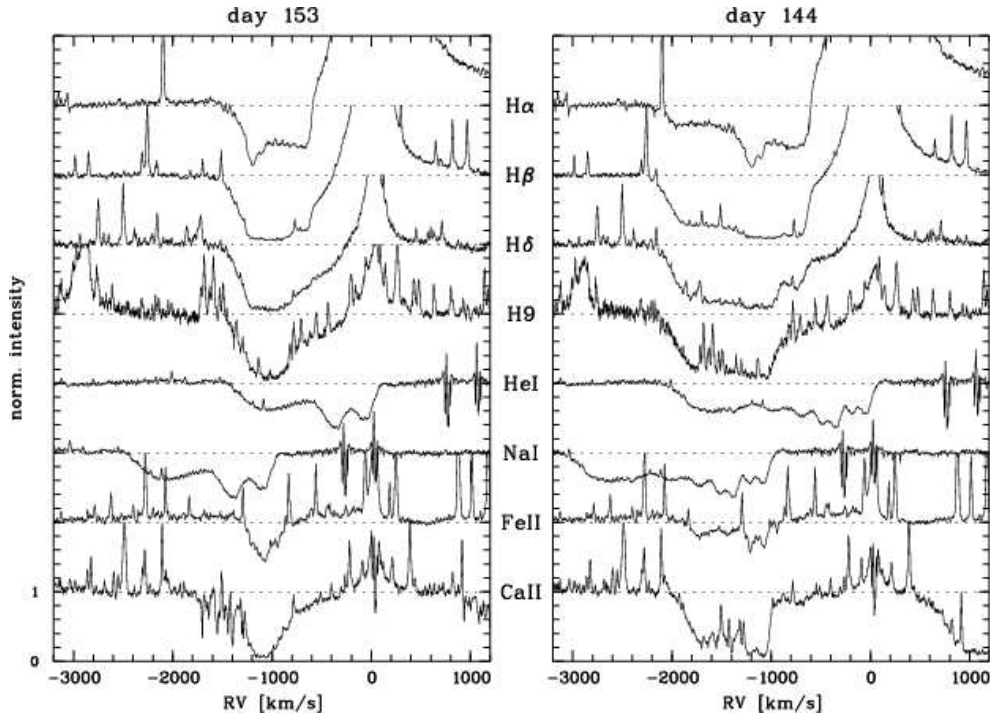


Figure 2.5: Jet absorption line structure; adopted from Schmid et al. (2001)

is too highly ionized to produce absorptions. Absorption components of the Ca II line in the RV range of ≈ -1800 to 1200 km s^{-1} could be created by shocks in the jet.

Highly blue-shifted components with RV up to -2000 km s^{-1} appear repeatedly on timescales of a few days. These can be seen simultaneously in H I and in the metal lines. They reach their maximum extend within one or two days and decay within the following few days. The decay of the fast component happens faster in He I than in H I, moreover they are stronger in He I with respect to the absorption around $\approx -1200 \pm 300$ km s^{-1} than those in H I. The He I transitions have a higher excitation potential, therefore the He I features can be associated with hotter and higher ionized gas.

At the same time as the appearance of the high velocity component, the absorptions in the RV range of ≈ -900 to -400 km s^{-1} are weakened. These two components are well anti-correlated (Fig. 2.6).

Examining the strong H α and H β lines, one can see that the blue wing of these lines are absorbed by a stable trough. Therefore the zone of Raman scattering of the L α and L β photons must be located behind H I gas. Also at this low velocity edge of the absorption, the fluxes become larger for higher Balmer transitions, the line opacities seem not to be very high.

2.5.3 First interpretations

The internal structure of the emitting regions and of the jet outflow can be derived by interpreting the observational data described in the last section (Fig. 2.7). The emission region can be divided into three distinct components. A variable hot component which is identified with the accreting white dwarf and the inner parts of the accretion disk. Furthermore, it is possible that additionally emission from a more outer part of the disk is present which is created by irradiation and reflection near the white dwarf. The temporal correlation suggests that the Fe II emission line region is also connected with this hot continuum source.

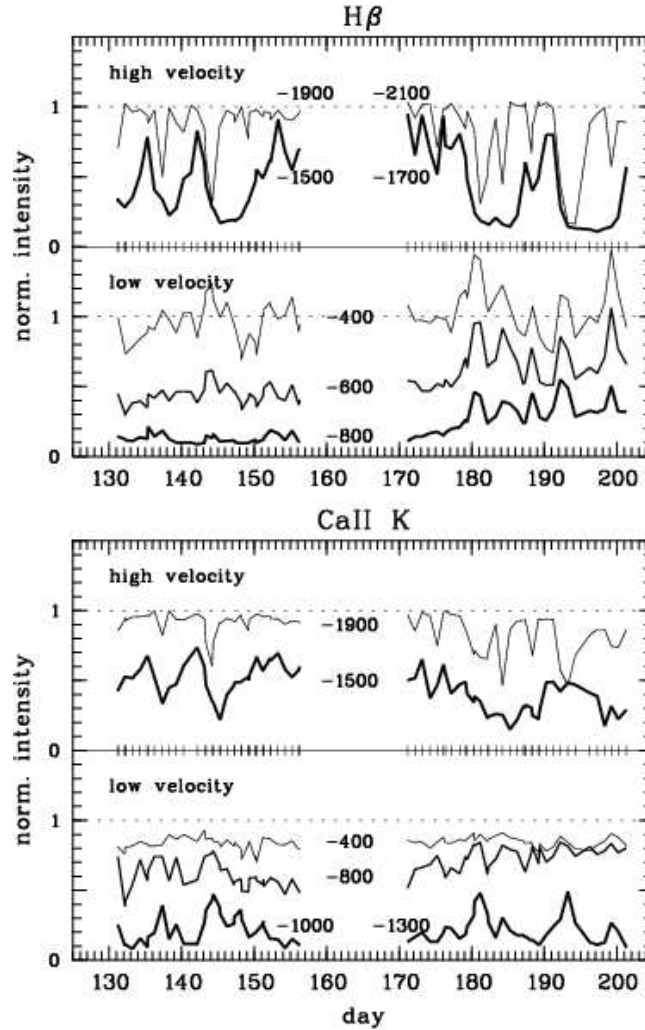


Figure 2.6: Anti-correlation between the high and low velocity components; adopted from Schmid et al. (2001)

A narrow line emission region can be identified with the upper layers of a neutral disk – similar to a chromosphere – which is irradiated by the hot continuum source. It emits mainly in allowed lines of single ionized heavy elements. The observed variations in the first component can therefore change the irradiation on the second and with it the ionization fraction of the partly ionized emission region. Again their variations are in step with each other. This model for the emission process requires a layered accretion disk. The disk structure is not yet known and is also subject of future simulations.

The third emission region is the red giant companion. The measured spectral type of this cool giant (M5.5 III, section 2.5.1) suggests the existence of an extended photospheric emission.

The outflow along the jet axis can also be categorized into three different parts. The initial acceleration region is located near the white dwarf. Its spectral signatures are those features with RVs of $\approx -400 \text{ km s}^{-1}$. The continuum source and the H I emission line region are only partly covered by this outflow region.

A region of the repeatedly transient high velocity components with RVs of -2000 km s^{-1} is found completely in front of the hot continuum source and partly covering the narrow line region.

see collisions of high velocity jet components with previously ejected gas that has already slowed down. This mechanism is expected for variable jet outflows whose velocity amplitudes are larger than the sound speed in the medium.

Chapter 3

The Models of propagating Jets

In this chapter, we describe the model geometry and the chosen jet parameters. We also discuss the simplifications and approximations made due to the constraints set by the available computer resources. We performed simulations of pulsed jets which were either adiabatic or cooled jets.

3.1 Geometric model

In order to combine a large computational domain with high spatial resolution it was not possible to perform model simulations in three dimensions. Therefore we had to choose a two-dimensional slice of the full domain and assumed axisymmetry. This kind of simulation is often called 2.5D simulations. The geometry of this slice in the examined system is shown in Figure 3.1. The dimensions of this two-dimensional slice are set to 50 AU in polar direction perpendicular to the orbital plane of the binary and 30 AU in the direction of the orbital plane – Figure 3.1 is not drawn to scale. The hot component is located in the origin of the coordinate frame. Due to axisymmetry the companion is expanded into a “Red Giant Ring”. In the two-dimensional slice, only half of the cross-section of this ring is included. The binary separation is chosen to 4 AU which is within the range of the estimated separations of 3.3 - 5.2 AU. The density of the red giant is set to $2.8 \cdot 10^{-5} \text{ g cm}^{-3}$ and its radius to 1 AU.

Surrounding the red giant, a stellar wind is implemented. The wind has a constant velocity of $v = 10 \text{ km s}^{-1}$, a gas temperature of $T = 50 \text{ K}$ and a mass loss rate of $10^{-6} \text{ M}_{\odot} \text{ yr}^{-1}$. The density of the red giant wind at the surface of the star is then $2.2 \cdot 10^{-14} \text{ g cm}^{-3}$. The density of the external medium is given by an $1/r_{\text{rg}}^2$ -law for a spherical wind where r_{rg} is the distance from the center of the red giant. The density of red giant wind near the jet nozzle is about 200 times higher than the initial jet density. At a distance of 50 AU from the symbiotic system, i.e. at the boundary of the integration domain, the wind density is about equal to the jet density at the nozzle.

In 3D this density distribution corresponds to a torus-like structure for small z ($< 5 \text{ AU}$) which becomes a slightly flattened but quasi-spherical distribution $\approx 1/r^2$ centered on the jet nozzle for large z ($> 10 \text{ AU}$). This seems to be a reasonable approximation for the z -direction. In the r -direction we introduce by this procedure artificially a density symmetry around the jet axis, what may be a qualitative important difference compared to real jets in binary systems.

The gravitational potential of the two stars with assumed masses of 1 M_{\odot} each is taken into account. However, the effect of the gravitational potential on the resulting jet structure is marginal.

The numerical resolution is chosen to 20 grid cells per AU, therefore our computational domain was 1000×600 grid cells. To account for the counter-jet and the other part of the jet, respectively, the boundary conditions in the equatorial plane and on the jet axis are set to reflection symmetry. On the other boundaries, outflow conditions are chosen.

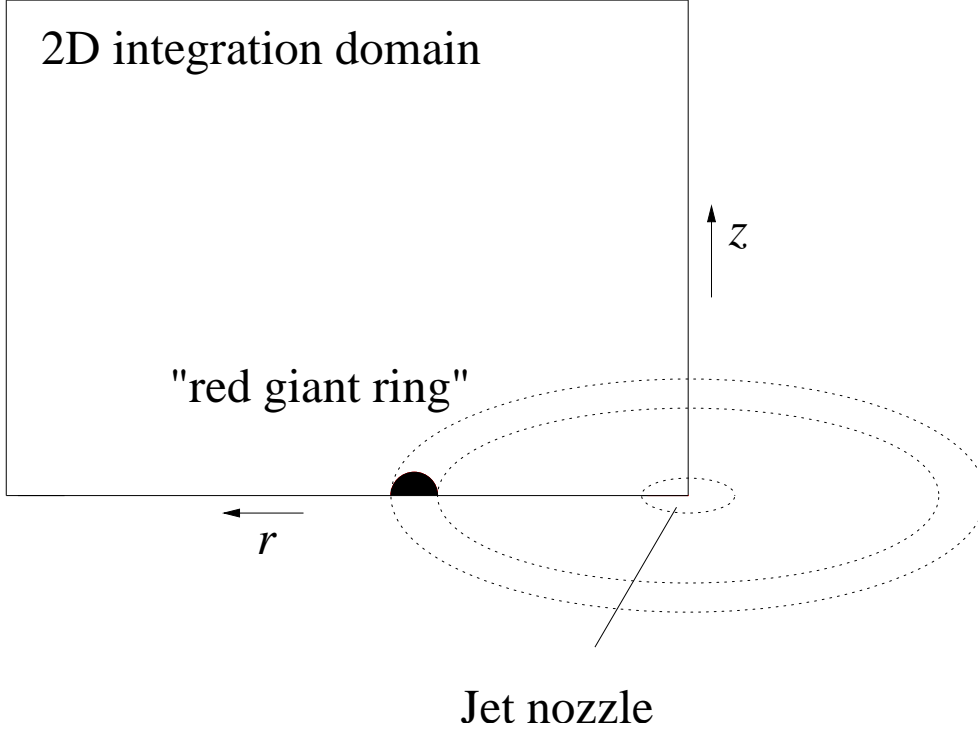


Figure 3.1: Sketch of the reduction from 3D to 2.5D simulations

3.2 Parameters for the pulsed jet

The jet is injected within a thin jet nozzle with a radius of 1 AU. Because we want to investigate with these simulations the propagation of small scale structures in the jet and not the formation and collimation of the jet outflow, this ansatz is appropriate. We assume that the jet is already completely collimated when leaving the nozzle. To simulate the stable velocity component mentioned in section 2.5.2, the initial velocity of the jet is chosen to 1000 km s^{-1} or 0.578 AU d^{-1} and its density is set to $8.4 \cdot 10^{-18} \text{ g cm}^{-3}$ (equal to a hydrogen number density of $5 \cdot 10^6 \text{ cm}^{-3}$). These parameters lead to a density contrast η of $5 \cdot 10^{-3}$, a Mach number of ≈ 60 in the nozzle and a mass loss rate of $\approx 10^{-8} M_{\odot} \text{ yr}^{-1}$.

Repeatedly each seventh day, the velocity and density values in the nozzle are changed to reflect the jet pulses which are seen in the observations of MWC 560 (section 2.5.2). The effects of different pulse densities and speeds are investigated with a parameter study for adiabatic jet models.

Table 3.1 lists the main parameters of the models: the model number, the density of the pulse in the nozzle n_{pulse} , the velocity of the pulse in the nozzle v_{pulse} , the mass loss during the pulse \dot{M} and the kinetic jet luminosity during the pulse. Each pulse lasts for one day. Thus the first 4 models have pulses with enhanced velocity and lower, the same or higher density as the “regular” outflow. In the models v to viii only the density is changed, except for the special model vii which has no pulses at all. The mass loss and the jet power depend on these values by

$$\begin{aligned} \dot{M} &= \pi R_{\text{jet}}^2 m_H n_{\text{jet}} v_{\text{jet}} \\ L_{\text{jet}} &= \frac{1}{2} \dot{M} v_{\text{jet}}^2 = \frac{1}{2} \pi R_{\text{jet}}^2 m_H n_{\text{jet}} v_{\text{jet}}^3. \end{aligned}$$

Table 3.1: Parameters of the jet pulses: the model number, the density of the pulse in the nozzle n_{pulse} in cm^{-3} , the velocity of the pulse in the nozzle v_{pulse} in cm s^{-1} , the mass loss during the pulse \dot{M} in g s^{-1} and in $M_{\odot} \text{ yr}^{-1}$, the kinetic jet luminosity during the pulse in erg s^{-1} and the axial and radial extent of the bow shock after 380 days of simulation time. Model vii is a special case, because no pulses are present. Therefore “pulse” values given for this model are identical to the jet parameters out of pulses valid for each model

model	$n_{\text{pulse}} [\text{cm}^{-3}]$	$v_{\text{pulse}} [\text{cm s}^{-1}]$	$\dot{M} [\text{g s}^{-1}]$	$\dot{M}' [M_{\odot} \text{ yr}^{-1}]$	$L_{\text{jet}} [\text{erg s}^{-1}]$
i	$1.25 \cdot 10^6$	$2.0 \cdot 10^8$	$2.94 \cdot 10^{17}$	$4.66 \cdot 10^{-9}$	$5.88 \cdot 10^{33}$
ii	$2.5 \cdot 10^6$	$2.0 \cdot 10^8$	$5.88 \cdot 10^{17}$	$9.33 \cdot 10^{-9}$	$1.18 \cdot 10^{34}$
iii	$5.0 \cdot 10^6$	$2.0 \cdot 10^8$	$1.18 \cdot 10^{18}$	$1.87 \cdot 10^{-8}$	$2.35 \cdot 10^{34}$
iv	$1.0 \cdot 10^7$	$2.0 \cdot 10^8$	$2.35 \cdot 10^{18}$	$3.73 \cdot 10^{-8}$	$4.70 \cdot 10^{34}$
v	$1.25 \cdot 10^6$	$1.0 \cdot 10^8$	$1.47 \cdot 10^{18}$	$2.33 \cdot 10^{-9}$	$7.35 \cdot 10^{32}$
vi	$2.5 \cdot 10^6$	$1.0 \cdot 10^8$	$2.94 \cdot 10^{17}$	$4.66 \cdot 10^{-9}$	$1.47 \cdot 10^{33}$
vii*	$5.0 \cdot 10^6$	$1.0 \cdot 10^8$	$5.88 \cdot 10^{17}$	$9.33 \cdot 10^{-9}$	$2.93 \cdot 10^{33}$
viii	$1.0 \cdot 10^7$	$1.0 \cdot 10^8$	$1.18 \cdot 10^{18}$	$1.87 \cdot 10^{-8}$	$5.88 \cdot 10^{33}$

* equivalent to no pulses, these values represent the jet parameters out of pulses valid for each model

3.3 A model with Cooling

The available computer resources set strong constraints to the microphysics which can be included in our models. A high spatial resolution is important for jet simulations in order to resolve the fine structure.

The parameter study for pulsed jets is therefore restricted to adiabatic simulations, where we neglect both the cooling term Λ in the energy equation (A.1c) and the interaction equations (A.2).

It is well known from previous simulations of protostellar and extragalactic jets e.g. by Stone & Norman (1993) and Steffen et al. (1997) that the resulting jet structure differs strongly between purely hydrodynamical models and models using radiation hydrodynamics. This should also be the case in the parameter region of jets in symbiotic stars.

Therefore we performed one pulsed jet simulations including radiative cooling. For this we have chosen the same parameters as for the hydrodynamical model i, in which the jet velocity during the pulse phase is doubled from 1000 km s^{-1} to 2000 km s^{-1} while the particle number density is reduced by a factor of 4 from $5 \cdot 10^6 \text{ cm}^{-3}$ to $1.25 \cdot 10^6 \text{ cm}^{-3}$ in the jet beam. Thus the kinetic energy of the jet gas in the nozzle remains constant.

Radiative cooling is treated with a simple procedure. The cooling by metals is described by a general cooling function $\Lambda(T)$ adopted from Sutherland & Dopita (1993) and bremsstrahlung emission is considered. In addition we determined for each grid point the density of H I, H II and e^- from the rate equations and calculate the cooling due to collisional ionization and line excitation of H I.

The expensive computational costs of the additional terms and equations to solve, together with an increased demand for memory, made it impossible to perform this simulation on a normal workstation. Therefore the already vectorized code was modified to run on the NEC SX-5 supercomputer at the High Performance Computing Center (HLRS) in Stuttgart (Krause 2001).

Table 3.2: Axial and radial extent of the bow shock after 380 days of simulation time and its aspect ratio

model	z_{bowshock} [AU]	r_{bowshock} [AU]	aspect ratio r/z
i	41.2	15.2	0.3689
ii	42.0	15.4	0.3666
iii	46.0	17.1	0.3717
iv	50.0	18.4	0.3680
v	43.8	14.4	0.3288
vi	48.6	14.6	0.3004
vii	48.0	14.4	0.3000
viii	38.7	14.5	0.3747

3.4 Structure of the jets

3.4.1 Adiabatic jet models

Bow shock geometry

First, we focus on the bow shock geometry and morphology obtained from our jet simulations. In figures 3.2-3.5 the logarithm of density is plotted for the eight hydrodynamical models listed in Table 3.1. These are the model results for day 380 of the simulations, at which the first model (model iv) reaches the outer boundary.

In the models i–iv with the higher jet pulse velocity of 2000 km s^{-1} , the axial extent of the bow shock after 380 days – and therefore its averaged velocity – increases with increasing jet pulse density and mass loss of the white dwarf (see Table 3.2). This seems to be a trend in the simulations which is also valid for the radial extent of the bow shock. No clear trend is present in models v–viii, where the jet velocity is constant and only the jet pulse density is varied. The models with the highest and lowest pulse density have a lower averaged bow shock velocity than the intermediate models. The radial extent of the bow shock, however, is practically equal for all four models v–viii. Thus we can say that the shock front expansion velocity is about equal within 10 – 20 per cent for all our adiabatic jet simulations. The average expansion velocity of the bow shock during the 380 days is about 200 km s^{-1} in axial direction and about 75 km s^{-1} in radial direction. This has to be compared with the gas velocity in the jet nozzle, which is 1000 km s^{-1} .

However, a closer look at the model results shows a somewhat more complicated behavior. The aspect ratios of the bow shocks – the maximum radial extent divided by the maximum axial extent – evolves linear in time during the starting phase, later – when the density of the local external medium decreases – the axial extent of the bow shock increases faster than its radial extent (Fig. 3.6,top). Therefore the aspect ratio becomes smaller with increasing evolution time and jet length. This behavior is sometimes called bubble and cigar phase, respectively. The slopes of the linear function have been fitted and are listed in Table 3.3. The linear function fits only until a certain axial turning point P_0 , where the bow shock expansion leaves the linear domain. This can be seen in the residual plot (Fig. 3.6, bottom). P_0 is defined as point on the z-axis where the residuals become larger than 0.3 AU.

The evolution of the bow shock geometry is plotted for model i in Fig. 3.7. The bow shock shape is created by the Kelvin-Helmholtz(KH)-instabilities, detectable in its bumpiness, which increases with time.

In Fig. 3.8 all shocks along the jet axis are plotted as function of time. The bow-shock evolution on the axis follows from the uppermost diamond for a given time. It can be seen that the bow shock velocity is almost constant, only slightly decreasing with time. This is consistent with a constant bow shock velocity which is found in self-similar models with a density profile of $\rho \sim r^{-2}$

Table 3.3: Slope of the radial vs. axial extent of the bow shock in the linear regime, fitted by $r = r_0 + az$, axial turning point P_0 from the linear function

model	r_0 [AU]	a	P_0 [AU]
i	2.21212	0.310644	47.2
ii	1.82992	0.322483	48.3
iii	1.18299	0.347285	> 49.5
iv	1.00693	0.349425	> 49.5
v	2.06176	0.289732	43.7
vi	1.83805	0.315015	37.4
vii	2.61516	0.274120	37.6
viii	1.05978	0.374761	34.7

(Carvalho & O’Dea 2002). Using the formula

$$v_{\text{bowshock}} = v_{\text{beam}} \frac{\sqrt{\eta\varepsilon}}{1 + \sqrt{\eta\varepsilon}} \quad (3.1)$$

with $\eta = \rho_{\text{jet}}/\rho_{\text{ambient}}$ the density contrast and $\varepsilon = A_{\text{head}}/A_{\text{beam}}$ the ratio of the jet head area to jet beam area, a constant bow shock velocity means that the product of $\eta\varepsilon$ remains constant. The decrease in η is compensated by an increase of the jet head area (Fig. 3.7).

Internal jet structure

From our simulations we can investigate in detail the internal structure of the model jets. For this we have plotted in Fig. 3.9 - 3.10 the structure of the beam along the jet axis for the hydrodynamical variables Mach number M (model i alone and as a comparison of model i and vii), parallel velocity component v_z , density ρ , pressure p and the temperature T for model i at day 380. The diamonds represent the locations of the pulses derived from the slice of the Mach number by searching for extremal points in Fig. 3.9.

The simulations show that the structure of the jet beam is strongly affected by the periodic jet pulses. This follows from the comparison of the Mach number of the pulsed jet model i with the pulse-free model vii. The latter model shows a rather smooth Mach number structure with only 5 strong shock discontinuities. In the pulsed jet model i many more and much stronger shocks are present.

After 380 days of simulation time, 54 pulses with higher velocity were injected, but only 22 are visible in the slice for the Mach number. The rest of the shocks merged (Fig. 3.8). During the first 50 days of simulation time, each pulse propagates with its initial injection velocity, until it reaches and merges with the Mach disk. At later stages, the situation becomes more complex: additionally to the shocks created by the pulsed injection, the transition from a laminar phase to a turbulent phase occurs, which is a normal feature in jet simulations with open boundary condition in the equatorial plane. Using reflection symmetry as boundary condition, the simulations start turbulent (Kössl & Müller 1988). The fact, that we see a laminar phase, could be a result of the red giant and its wind. They block partly the backflow which is responsible for the turbulences. There KH-instabilities are excited, grow nonlinearly and interact violently with the beam producing cross-shaped shocks inside the beam.

The internal pulses seem to be reflected by the cross-shaped shocks and run backwards until hitting and reflecting the next pulse and being reflected a second time. The situation in the other adiabatic jet models is qualitatively the same.

The density, pressure and temperature structure of the jet beam in model i shows a large scale structure with strong maxima near 25 AU and the bow shock region near 40 AU. These two regions coincide with velocity minima, thus these are regions where the jet material is strongly piled up.

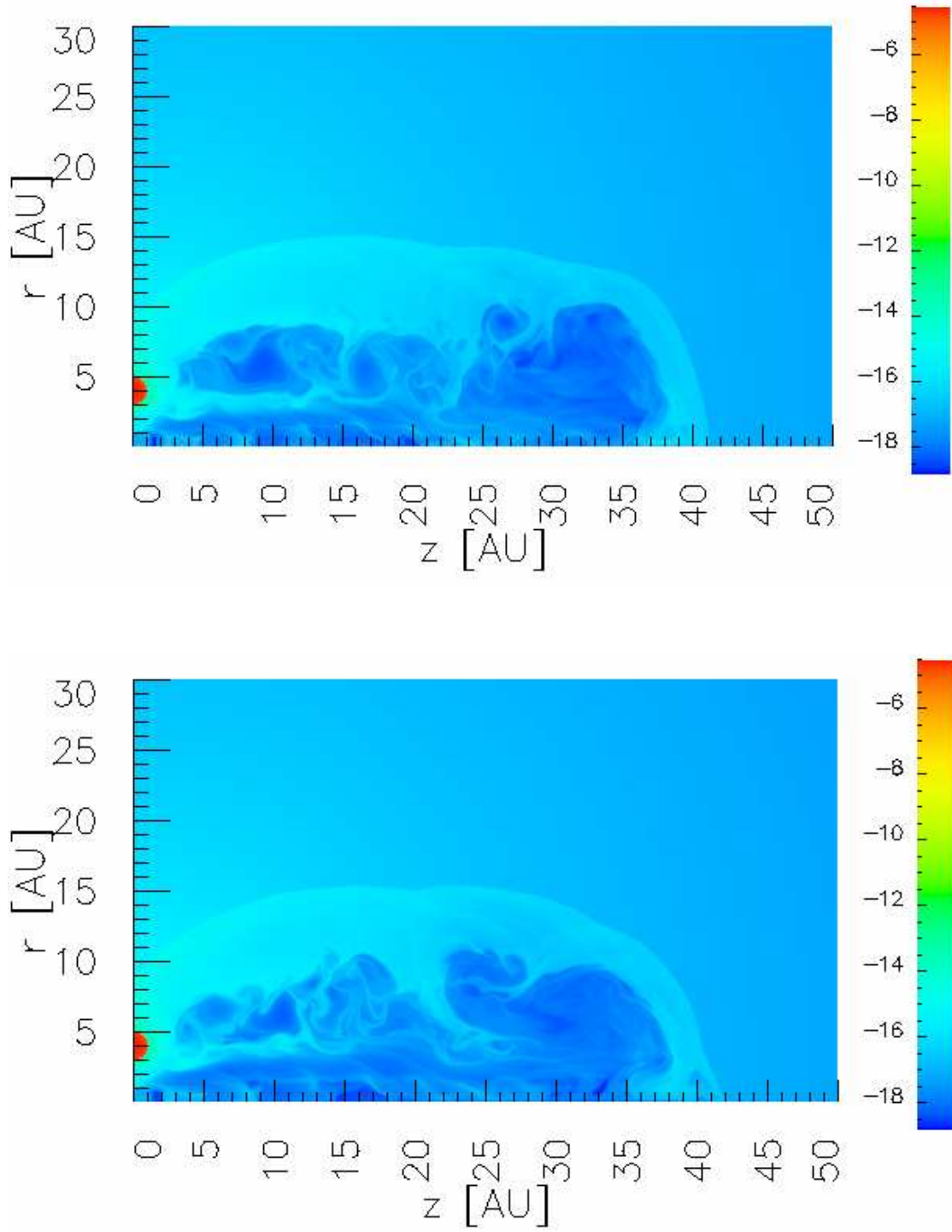


Figure 3.2: Color plot of the logarithm of density at day 380; top: model i ($v_{\text{pulse}} = 2000 \text{ km s}^{-1}$, $n_{\text{pulse}} = 1.25 \cdot 10^6 \text{ cm}^{-3}$), bottom: model ii ($v_{\text{pulse}} = 2000 \text{ km s}^{-1}$, $n_{\text{pulse}} = 2.5 \cdot 10^6 \text{ cm}^{-3}$)

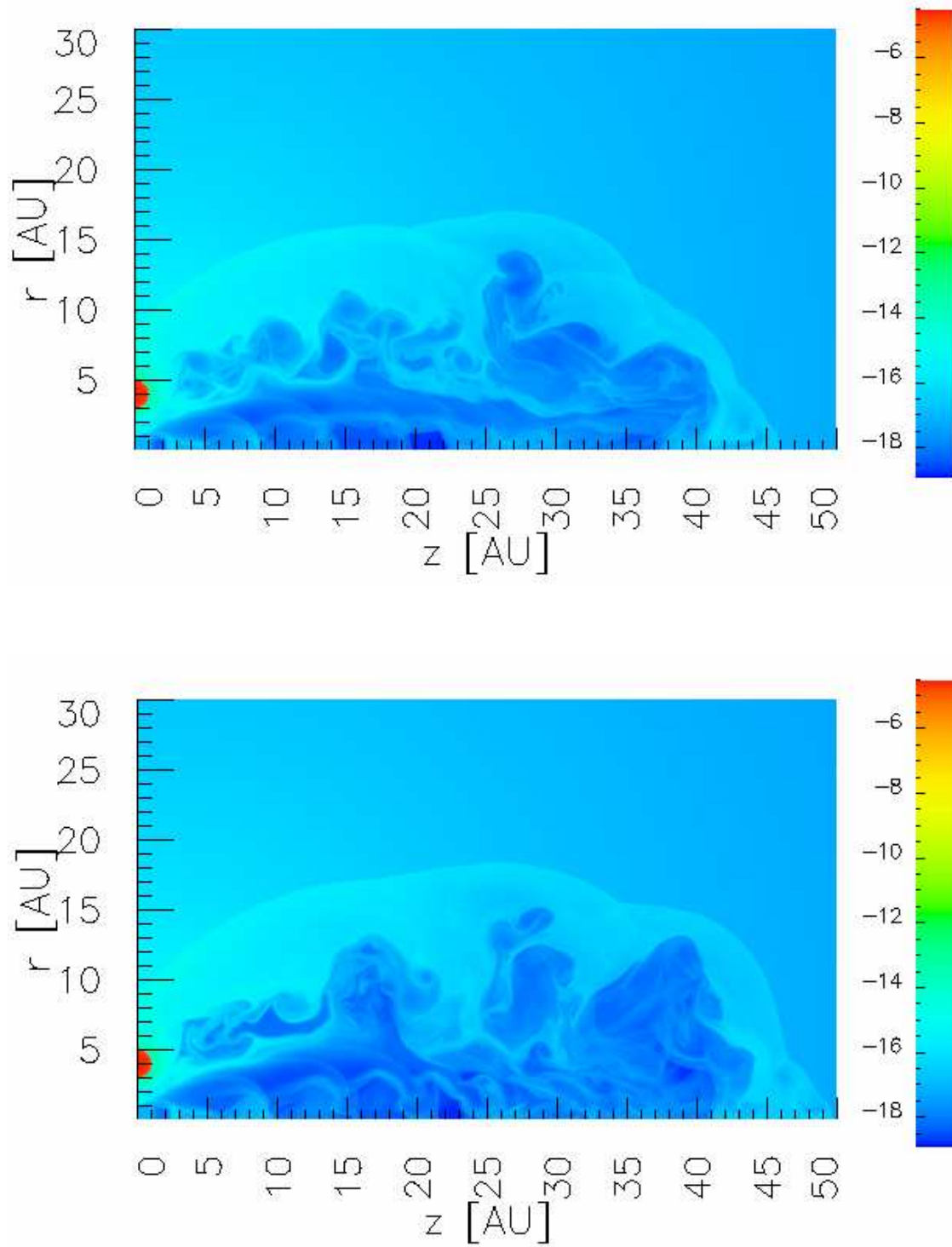


Figure 3.3: Color plot of the logarithm of density at day 380; top: model iii ($v_{\text{pulse}} = 2000 \text{ km s}^{-1}$, $n_{\text{pulse}} = 5 \cdot 10^6 \text{ cm}^{-3}$), bottom: model iv ($v_{\text{pulse}} = 2000 \text{ km s}^{-1}$, $n_{\text{pulse}} = 1 \cdot 10^7 \text{ cm}^{-3}$)

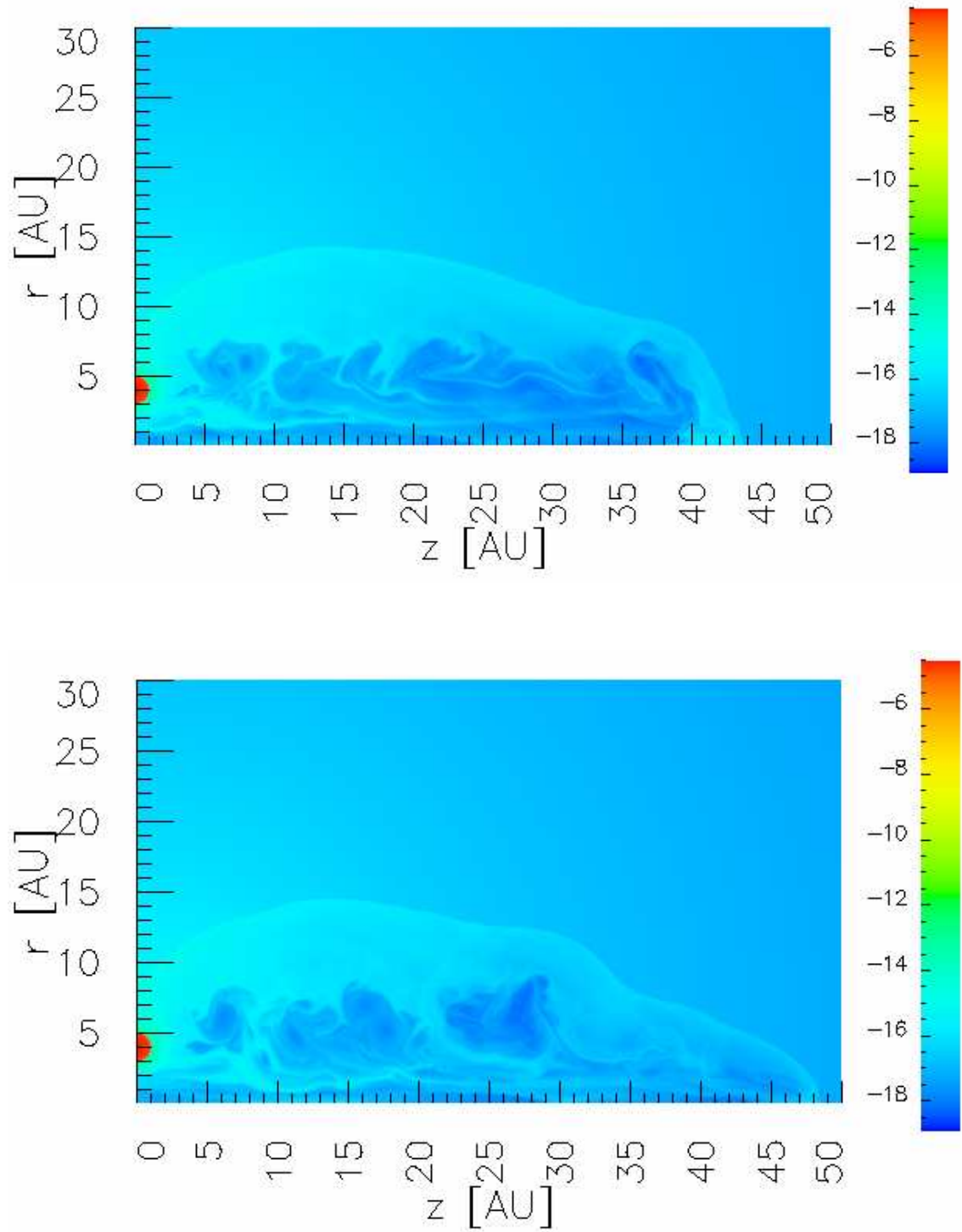


Figure 3.4: Color plot of the logarithm of density at day 380; top: model v ($v_{\text{pulse}} = 1000 \text{ km s}^{-1}$, $n_{\text{pulse}} = 1.25 \cdot 10^6 \text{ cm}^{-3}$), bottom: model vi ($v_{\text{pulse}} = 1000 \text{ km s}^{-1}$, $n_{\text{pulse}} = 2.5 \cdot 10^6 \text{ cm}^{-3}$)

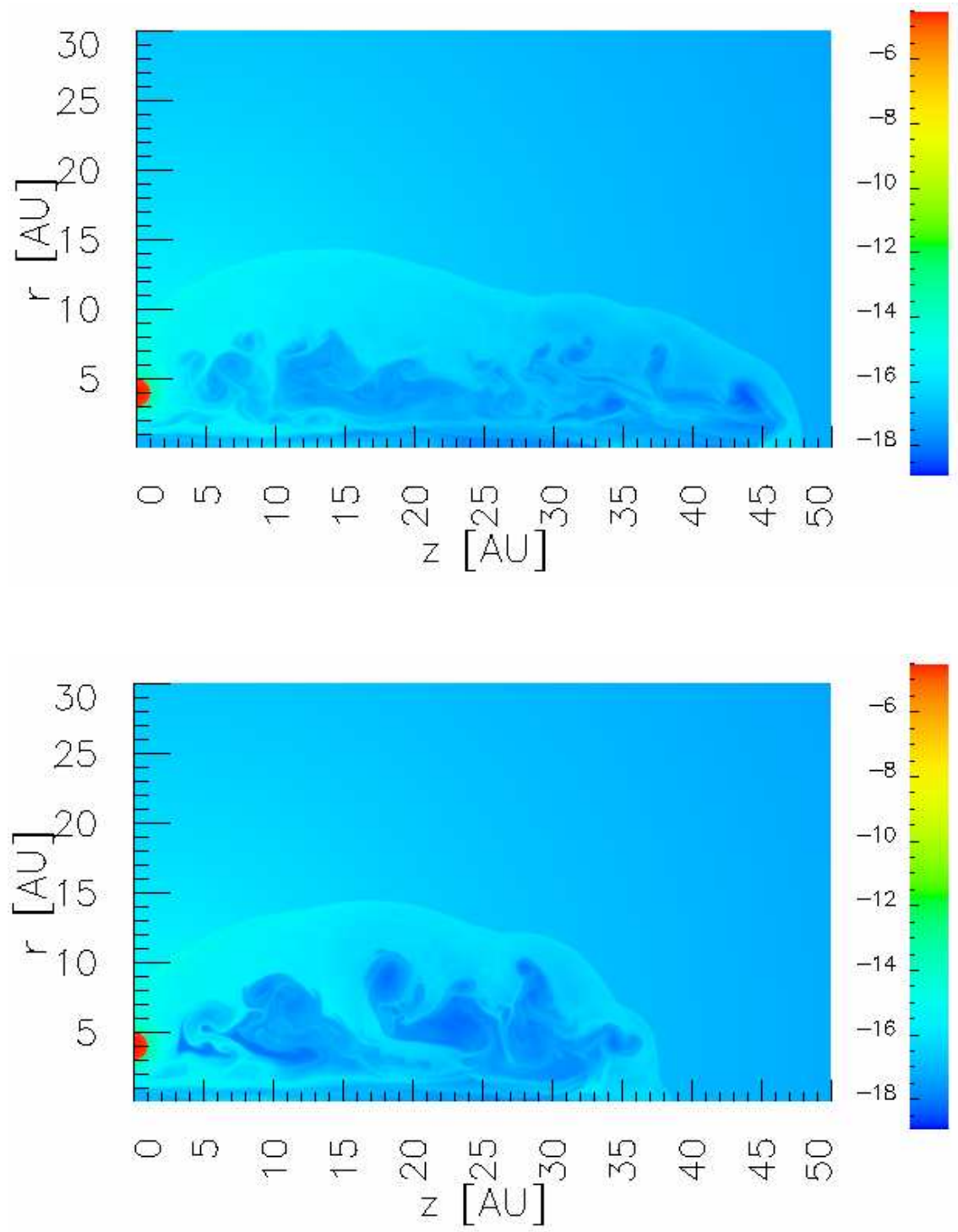


Figure 3.5: Color plot of the logarithm of density at day 380; top: model vii ($v_{\text{pulse}} = 1000 \text{ km s}^{-1}$, $n_{\text{pulse}} = 5 \cdot 10^6 \text{ cm}^{-3}$), bottom: model viii ($v_{\text{pulse}} = 1000 \text{ km s}^{-1}$, $n_{\text{pulse}} = 1 \cdot 10^7 \text{ cm}^{-3}$)

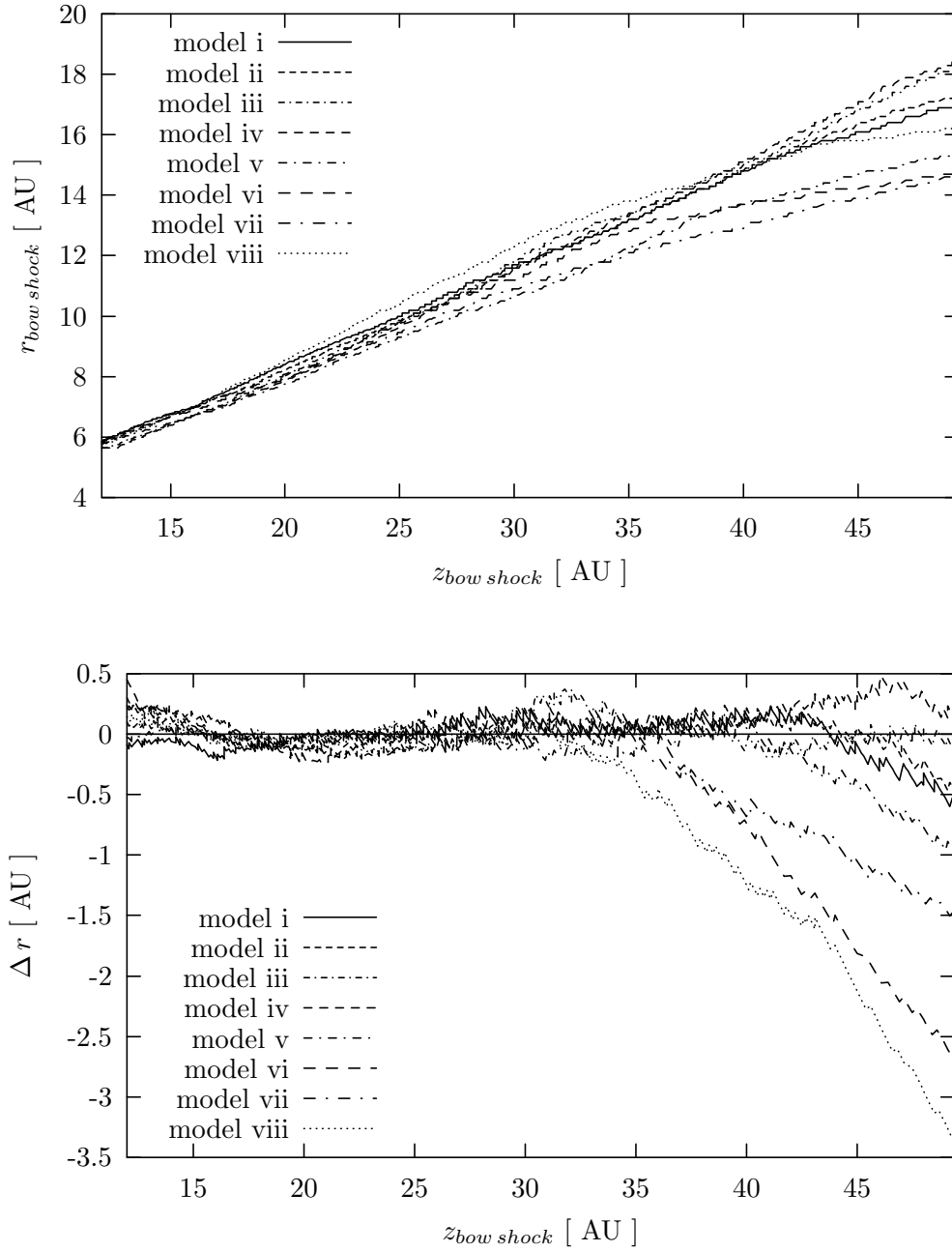


Figure 3.6: Aspect ratio of the bow shocks in the different models (top) and residuals from the linear function (bottom)

Superimposed are numerous small scale features. The gas temperature is, apart from the initial beam $z < 6$ AU, always above 10^5 K, typically between 10^6 K and 10^7 K. The density on the beam axis is in most places significantly lower than the initial jet density of $8.4 \cdot 10^{-18}$ g cm $^{-3}$ except for the strong shock regions near 25 AU, the bow shock near 40 AU and a shock near 8 AU.

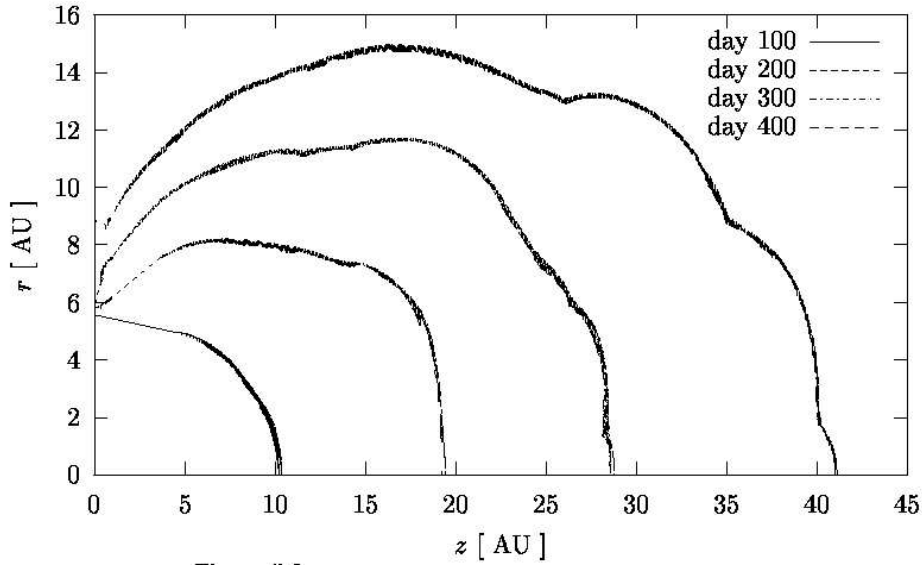


Figure 3.7: Shape of the bow shock for the model i; the jet head spreads with time, which leads, together with the decreasing η , to a constant bow shock velocity (Fig. 3.8)

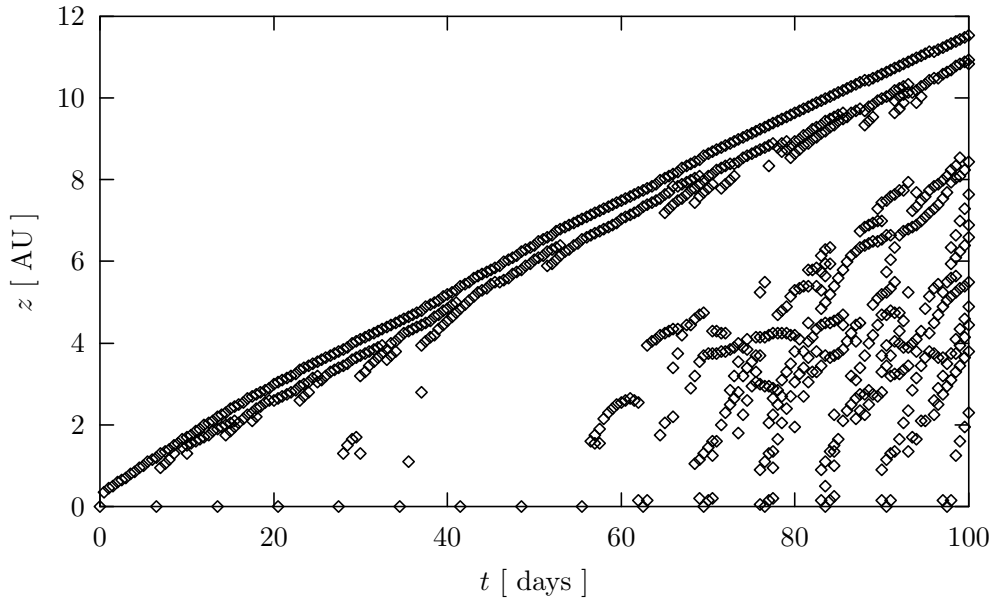


Figure 3.8: Evolution of the pulses (model i); the bow shock velocity remains constant as predicted in self-similar models with a density profile of $\rho \sim r^{-2}$

Radial profiles

In Fig. 3.11 - 3.12 radial profiles of the hydrodynamical variables are plotted for axial distances from the system of 10, 20, 30 and 40 AU for model i at day 380. Fig. 3.11 (top) shows the high velocity beam and a second peak with lower velocity outside the beam at distances near the jet source whose position is variable over the jet length. The backflow at again larger distances from

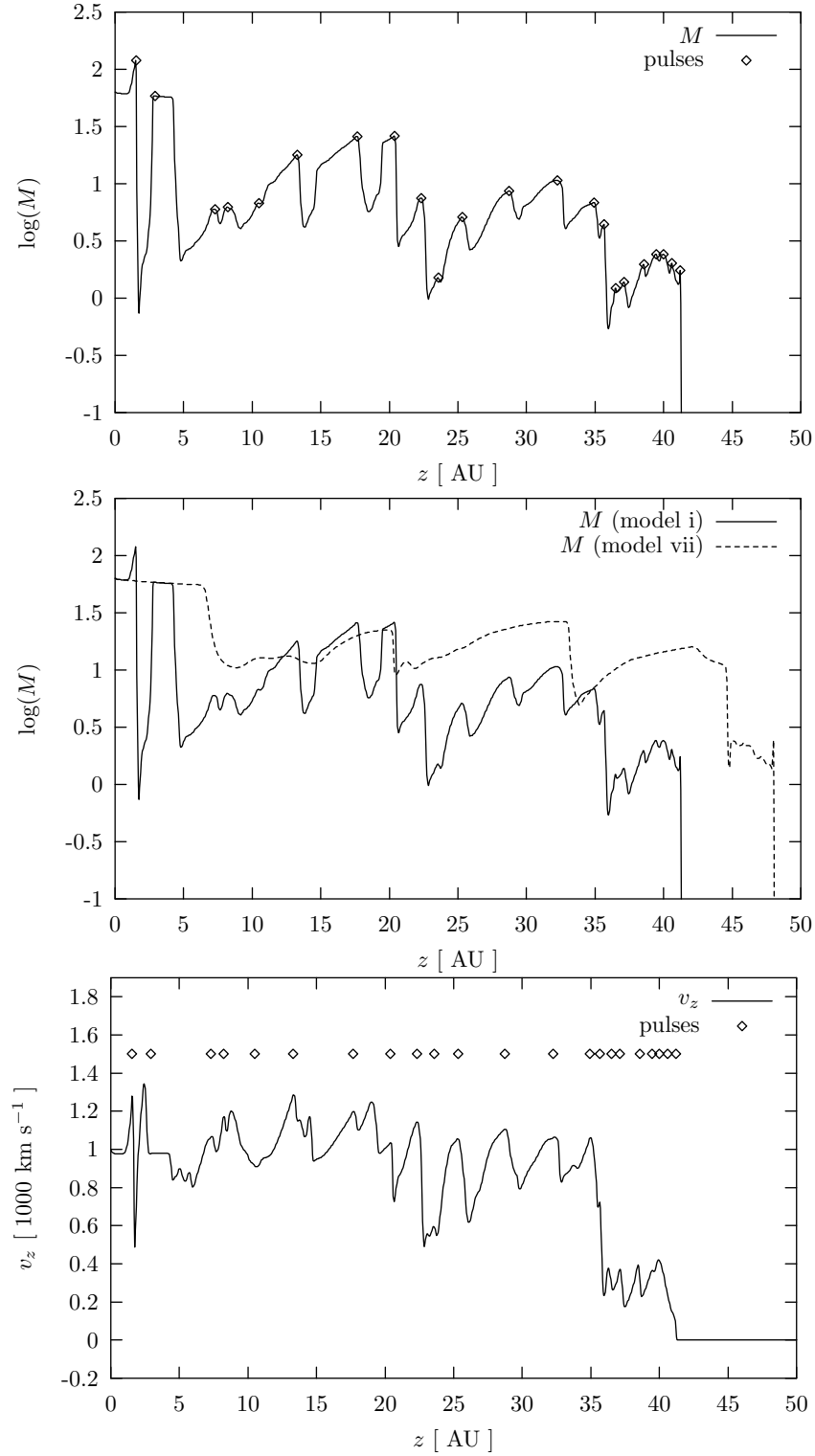


Figure 3.9: Slice of the logarithm of Mach number $M = v_z/c_s$ – for model i alone (top) and as a comparison of model i with pulses and vii without pulses (middle) – and of the parallel velocity component v_z (bottom) along the jet axis for model i at day 380; the diamonds represent the locations of the internal shocks derived from the slice of the Mach number by searching for extremal points

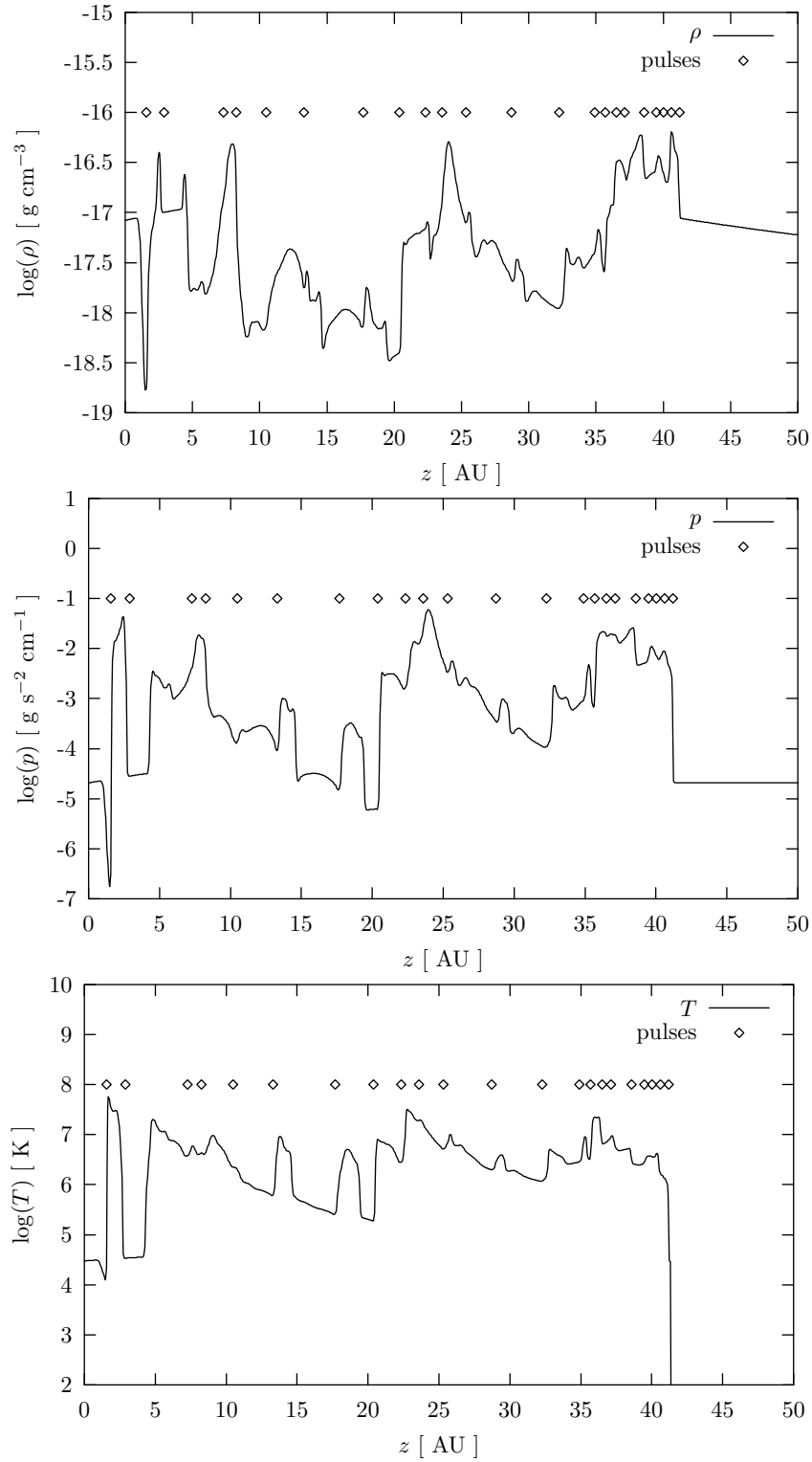


Figure 3.10: Slice of the logarithm of density ρ (top), logarithm of pressure p (middle) and of the logarithm of temperature T (bottom) along the jet axis for model i at day 380; the diamonds represent the locations of the internal shocks derived from the slice of the Mach number

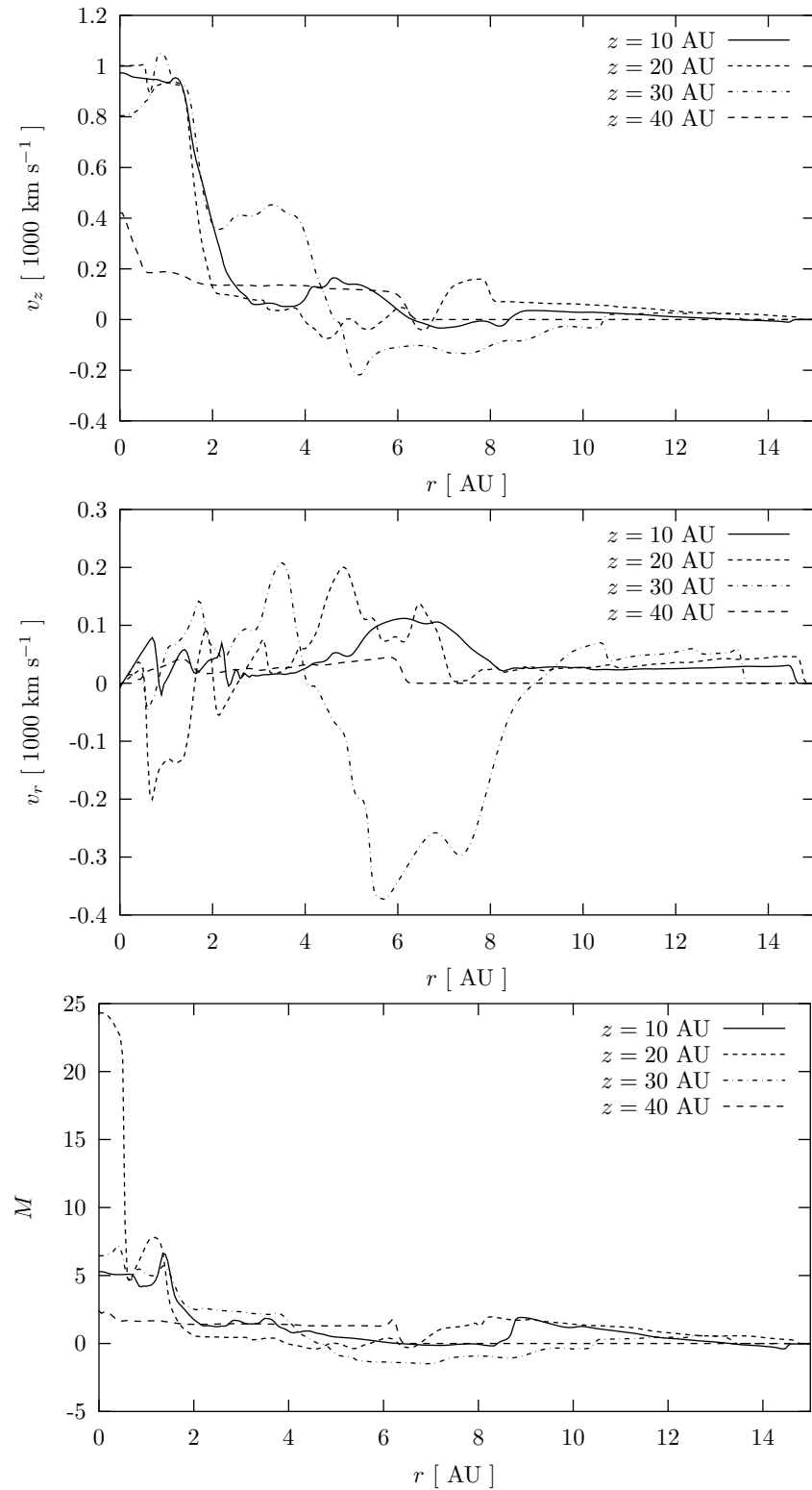


Figure 3.11: Radial profiles of the parallel velocity component (top), the radial velocity component (middle) and of the Mach number (bottom) of model i at day 380

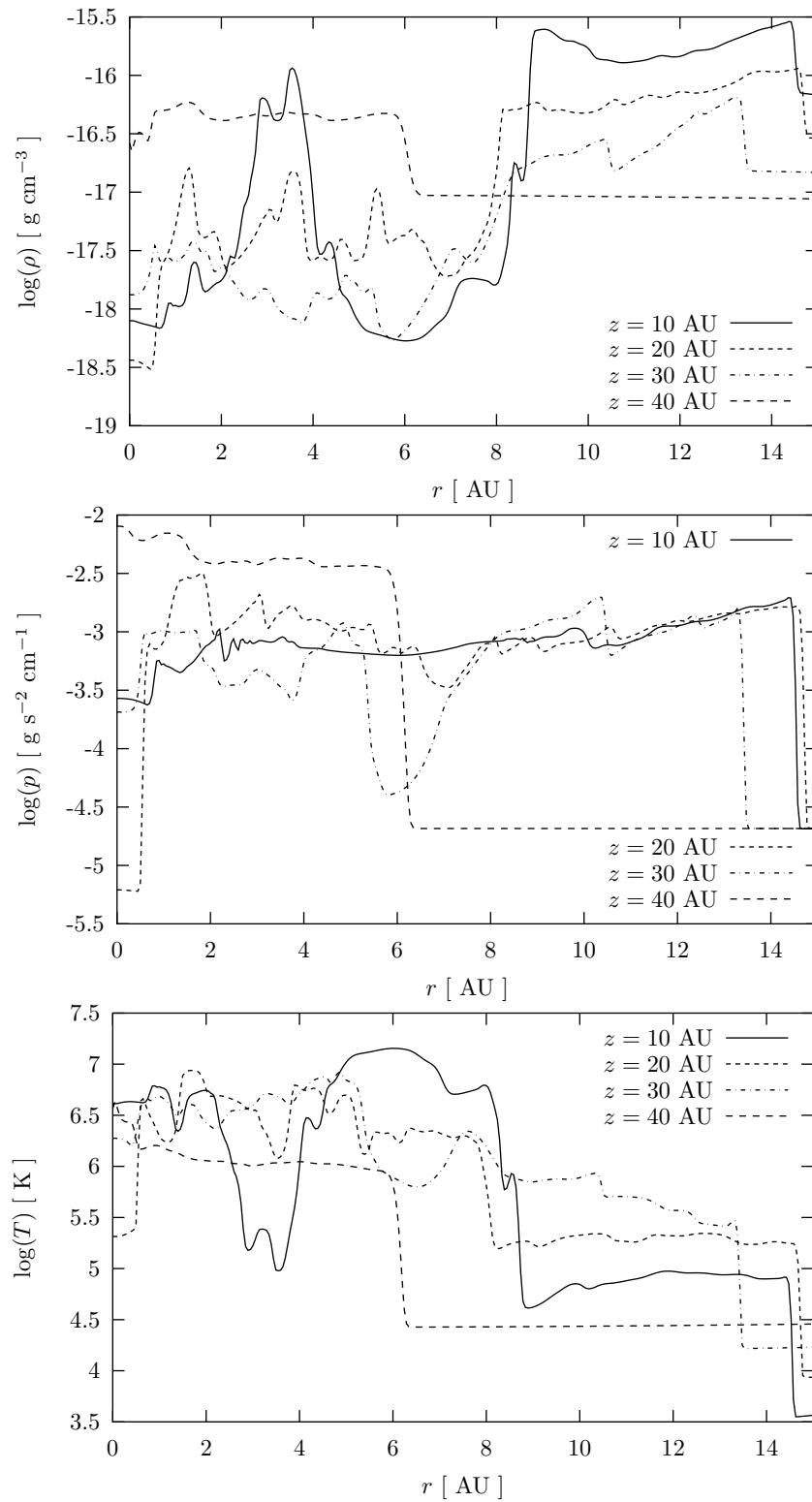


Figure 3.12: Radial profiles of the logarithm of density (top), logarithm of pressure (middle) and of the logarithm of temperature (bottom) of model i at day 380

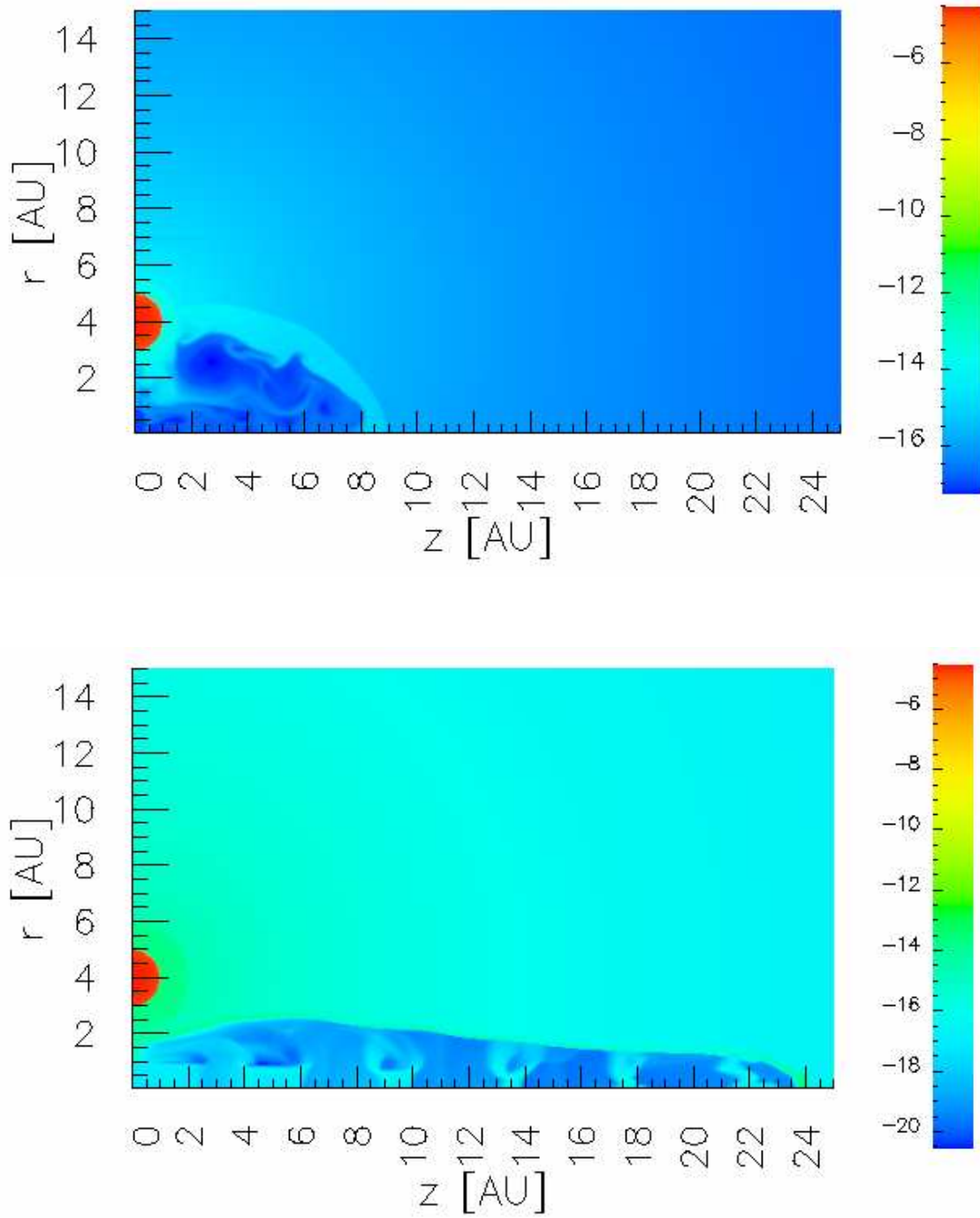


Figure 3.13: Color plot of the logarithm of density at day 74; model i ($v_{\text{pulse}} = 2000 \text{ km s}^{-1}$, $n_{\text{pulse}} = 1.25 \cdot 10^6 \text{ cm}^{-3}$) without cooling (top) and including cooling (bottom)

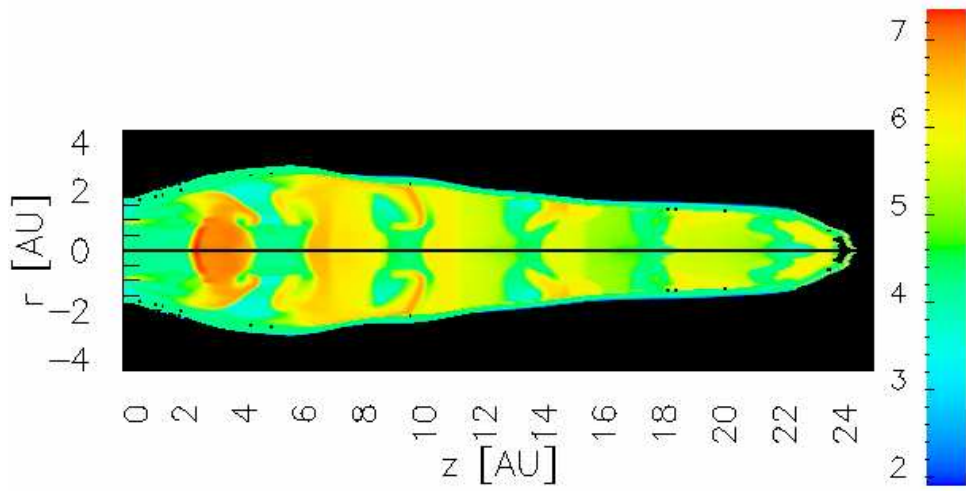


Figure 3.14: Logarithm of temperature of the model i with cooling; again the highest temperatures are present in the shocked ambient medium and jet beam, the region of medium temperatures is reduced with respect to model i without cooling

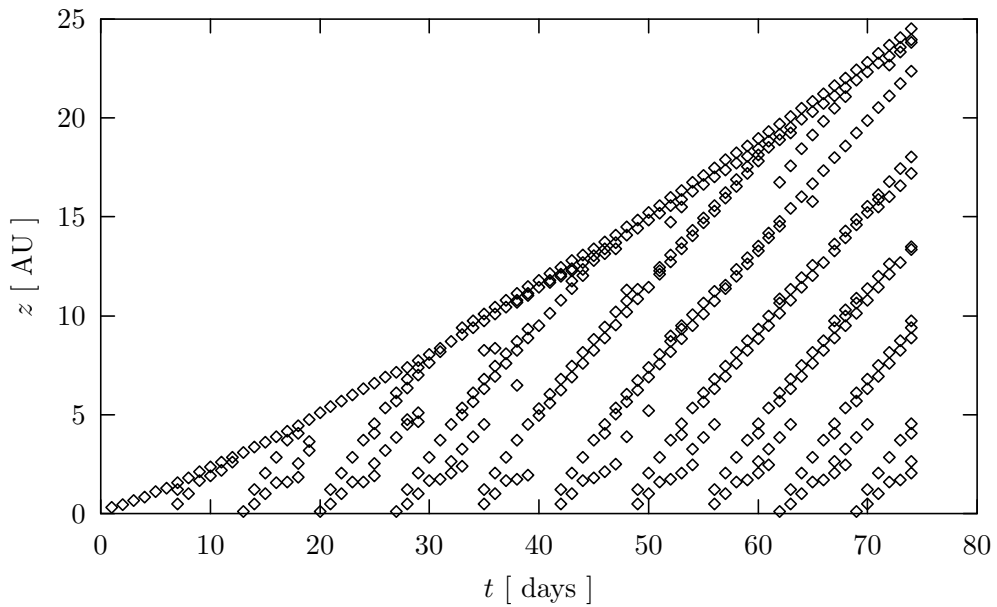


Figure 3.15: Evolution of the pulses (model i with cooling); all pulses can be traced easily due to the absence of the KH-instabilities seen in model i without cooling (Fig. 3.8)

the axis is clearly visible at intermediate axial distance of 30 AU. The backflow is coupled with a large velocity towards the axis at the same position representing the main vortex near the bow shock (Fig. 3.11, middle), also visible in Fig. 3.2 (top). The jet beam is highly supersonic with Mach numbers up to 25, while the material inside the cocoon moves transonic or subsonic.

In Fig. 3.12 (top) the double peak structure of the radial bow shock is visible, analog to the two shocks at the jet head formed by the pulses. The density inside the radial shock structure is enhanced by more than two orders of magnitudes with respect to the material in the jet beam and cocoon and by a factor of ten with respect to the density inside the jet beam near the jet head. The pressure is more or less constant inside the cocoon, while lowered in the jet beam with respect to the former. However, near the jet head the plateau in pressure also includes the jet beam.

The temperature is peaked inside the cocoon where the pressure is equal to its environment, but the density is small.

3.4.2 The model with radiative cooling

After 2000 CPU hours, the simulation reached only the 74th day, much less than the 380 days considered in the purely hydrodynamical simulations. However, the jet propagates much faster than without cooling (Fig. 3.13), and the resulting jet structure seems to be sufficiently evolved for a meaningful characterization of the jet properties.

Bow shock evolution

The cooled jet loses energy through radiation which instantaneously lowers the pressure and the temperature (Fig. 3.14). Therefore the radial extension of the jet, the cross section and the resistance exerted by the external medium are lessened. This leads to a faster propagation velocity. The bow shock velocity shows a steady increase from about 500 km s^{-1} during the first days to about 730 km s^{-1} after 70 days. The average bow shock velocity during the 74 days is 570 km s^{-1} . The bow shock velocity increases with time, because the jet head area remains almost constant and is therefore not able to compensate the decreasing local density contrast as in the simulations without cooling. The maximum radial extend of the jet cocoon is about 2.5 AU.

Internal structure

Fig. 3.15 shows the evolution of the internal shocks along the jet axis. The propagation of all pulses can be traced in the plot, indicating that the jet is still in its laminar phase.

Each new pulse is instantaneously slowed down from 2000 km s^{-1} to about 1200 km s^{-1} within the first two days. Without the disturbance of the KH-instabilities, the distance between the internal shocks created by the periodic velocity pulses stays constant. It remains to be investigated whether this situation changes if the kinetic energy for the jet gas in the pulses and the “normal” beam in the nozzle are not the same as in this model.

The very simple, periodic jet structure can also be seen in the axial cuts of the Mach number, axial velocity, density, pressure and temperature (Figs. 3.16-3.17). The internal shocks, which have not yet merged with the bow shocks from Fig. 3.15 can be identified with well defined discontinuities in all parameters.

The resulting jet flow thus shows two very different states of gas parameters which we call knots and hot beam. In the knots the density is high $\approx 10^{-16} \text{ g cm}^{-3}$ and the temperature low $\approx 10^4 \text{ K}$. Contrary to this the density in the hot beam is about 1000 times lower or $\approx 10^{-19} \text{ g cm}^{-3}$ while the temperature is much higher in the range of $10^{5.5} \text{ K}$ to 10^7 K .

Radial profiles

In Figs. 3.18-3.19, the same radial profiles are plotted for model i with cooling at day 74 as in Figs. 3.11- 3.12 for the adiabatic model i at day 380. Again, they show the significant differences between the adiabatic model(s) and the model including cooling. The parallel velocity stays almost

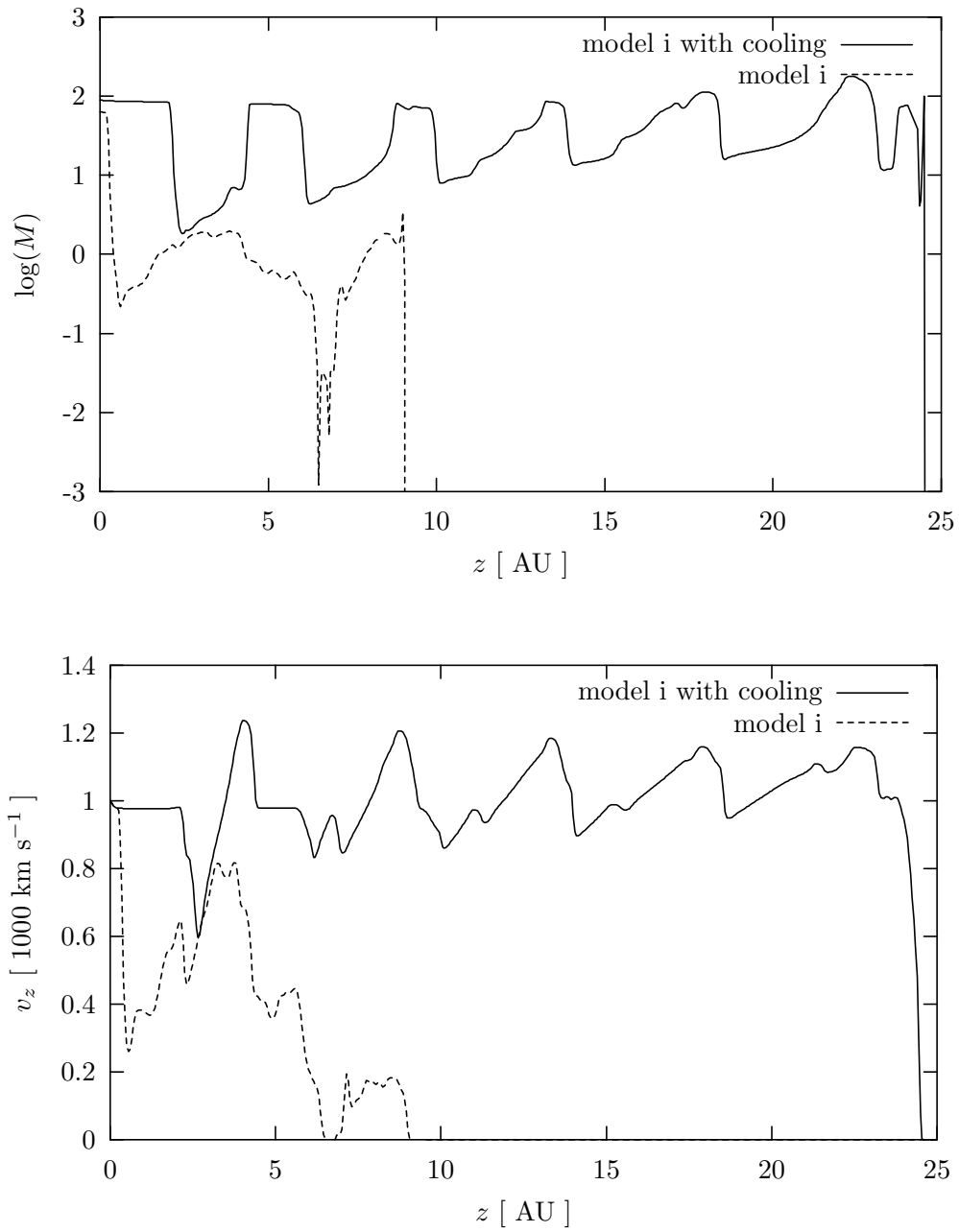


Figure 3.16: Slice of the logarithm of Mach number (top) and of the parallel velocity component along the jet axis for model i with cooling and without cooling, respectively. Results for both models are for day 74 in the simulation, for which 2D maps are plotted in Fig. 3.13

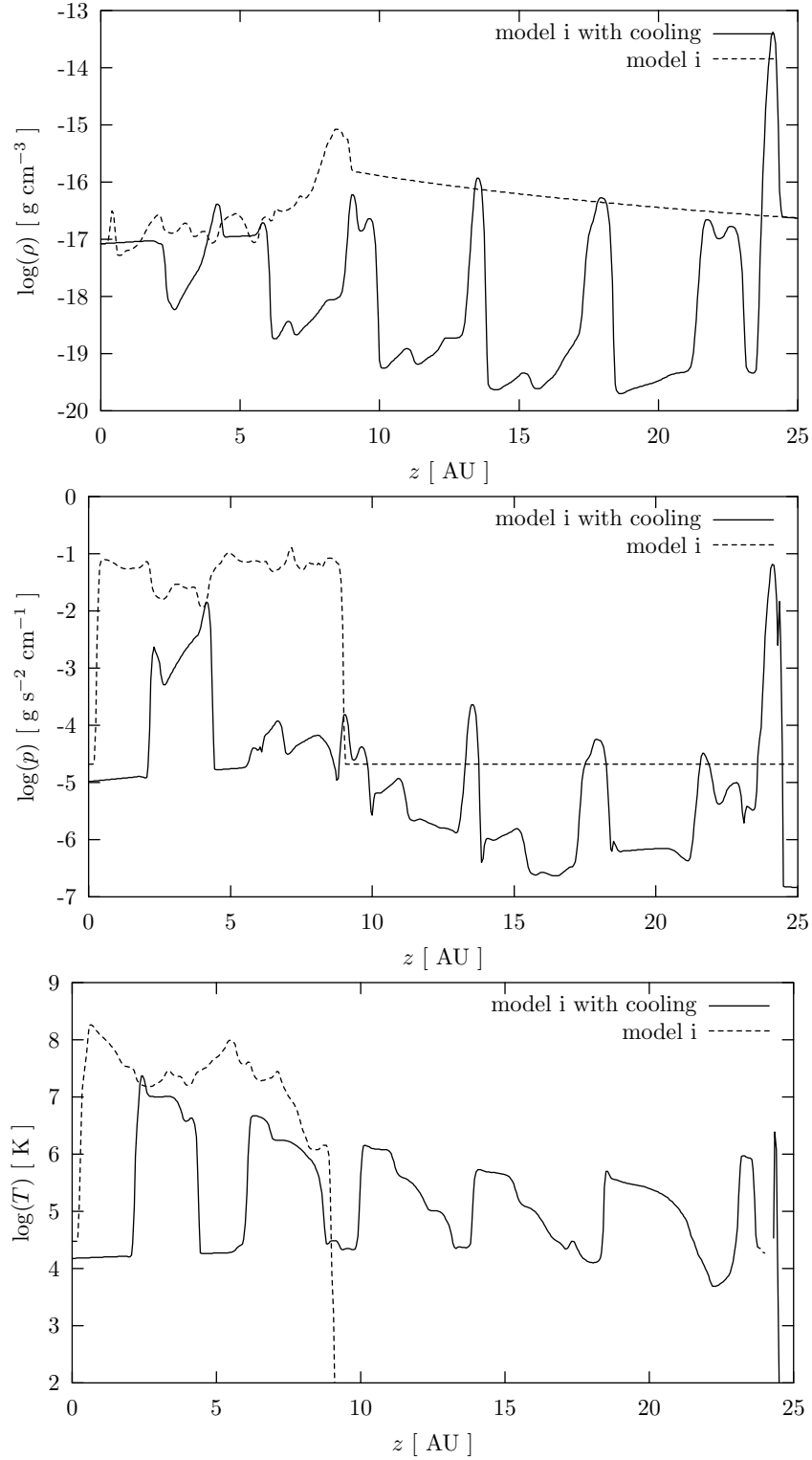


Figure 3.17: Slice of the logarithm of density (top), logarithm of pressure (middle) and of the logarithm of temperature (bottom) along the jet axis for model i with cooling and without cooling, respectively.

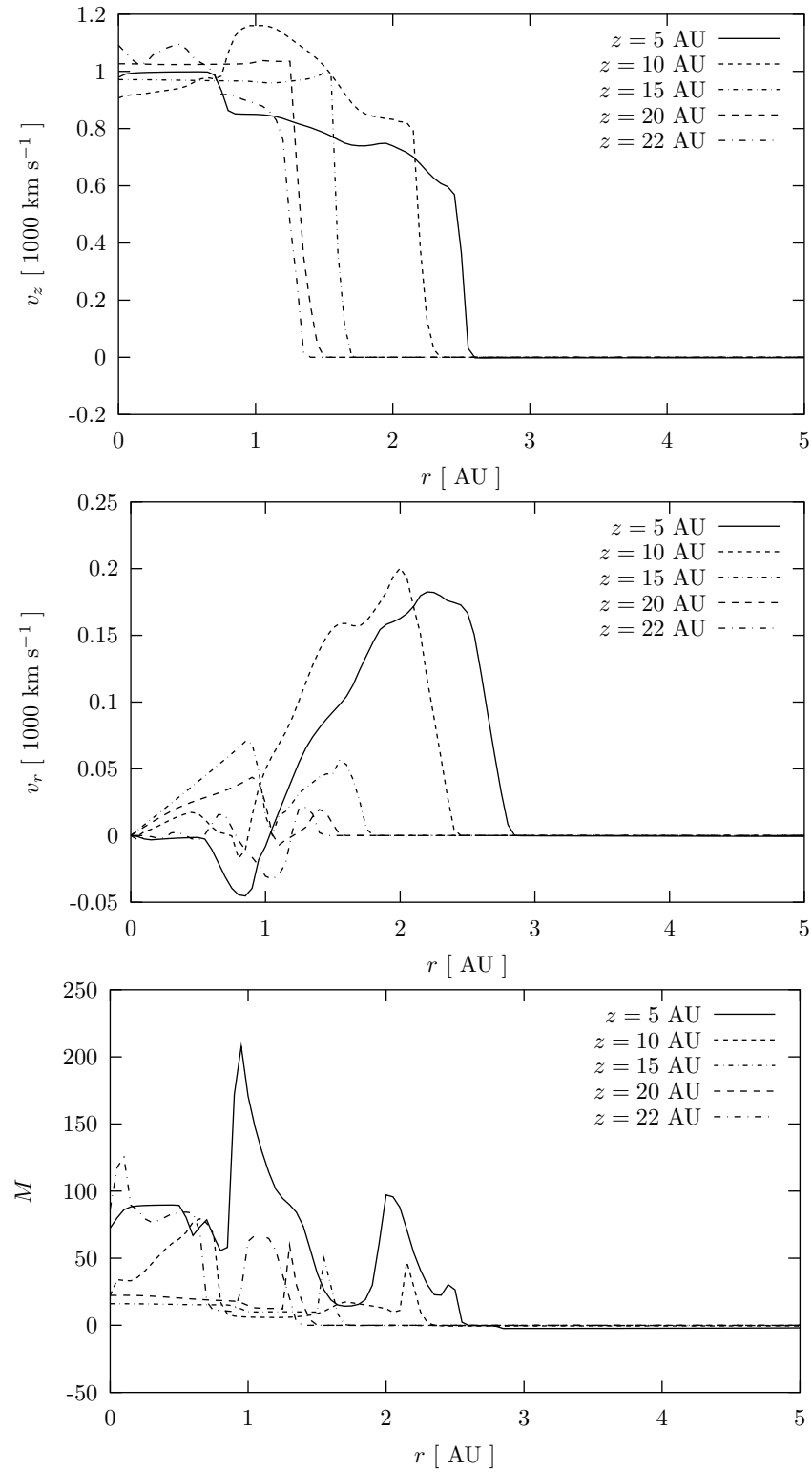


Figure 3.18: Radial profiles of the parallel velocity component v_z (top), the radial velocity component v_r (middle) and of the Mach number $M = v_z/c_s$ (bottom) of model i with cooling at day 74

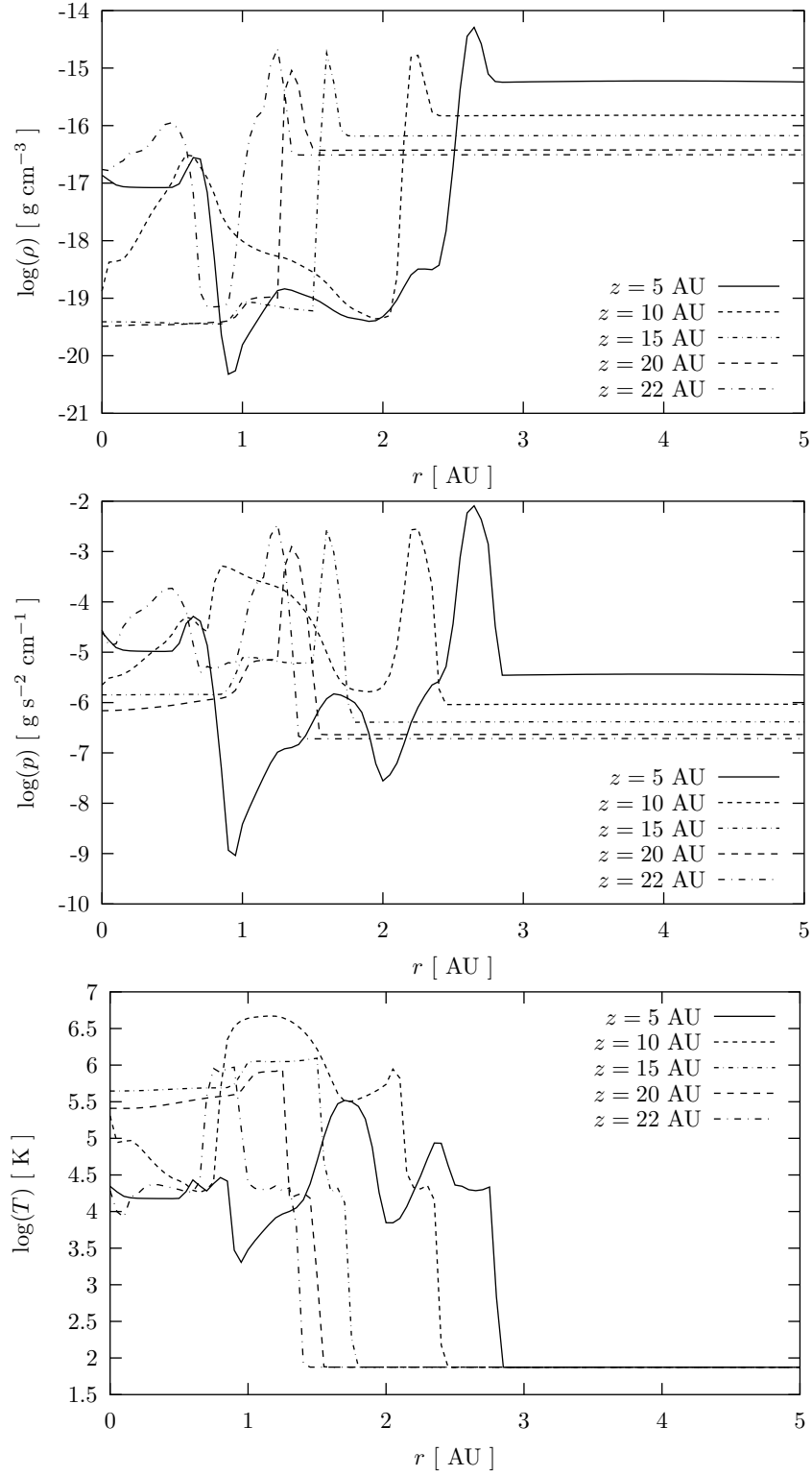


Figure 3.19: Radial profiles of the logarithm of density (top), logarithm of pressure (middle) and of the logarithm of temperature (bottom) of model i with cooling at day 74

constant along jet, in radial direction as well as in parallel direction. The jet consists only of the jet beam, no cocoon with a backflow component is visible and the jet beam velocity is relatively unchanged since the emission (Fig. 3.18, top). A larger radial expansion of the jet is only present near the jet source with velocities of the order of a few tenth of the jet propagation velocity (Fig. 3.18, middle). Although the parallel velocities components are in the cooled jet similar to those in the adiabatic jet, the Mach numbers are enhanced by a factor of ten (Fig. 3.18, bottom). This is an effect of its changed density and pressure values (Fig. 3.19, top and middle). As expected, the temperatures inside the cooled jet are reduced by two orders of magnitude (Fig. 3.19, bottom).

3.5 Emission of the jets

3.5.1 Adiabatic jet models

We present emission maps of the adiabatic jet models for bremsstrahlung, synchrotron and optical H I line radiation. They show the morphology of jets which would be observed if the only heating and cooling channels were shock heating and adiabatic expansion. We can construct these maps in order to investigate how the emission would look if radiative cooling would be relatively small compared with cooling due to adiabatic gas expansion, i.e. the cooling time scale is long compared to the dynamical time scale (see below).

In the models, temperatures ranges from 10^3 K in the red giant wind and $10^5 - 10^8$ K in the jet (Fig. 3.20), which makes the jets X-ray emitters due to thermal bremsstrahlung.

According to standard radiation theory of optically thin plasmas, e.g. Rybicki & Lightman (1979), the total emissivity due to bremsstrahlung from a completely ionized plasma is

$$j = 1.68 \cdot 10^{-27} T^{1/2} n_e n_i \text{ erg s}^{-1} \text{ cm}^{-3}. \quad (3.2)$$

Using the density and pressure data in each grid cell of the simulations, the emission per grid cell can be calculated and emission maps can be produced.

An estimate on the cooling time for the jet gas due to bremsstrahlung can be obtained from

$$t_{cool} = \frac{n k T}{1.68 \cdot 10^{-27} T^{1/2} n_e n_i} = 0.83 \frac{\sqrt{T_7}}{n_7} \text{ yr} \quad (3.3)$$

where T_7 is the temperature in units of 10^7 K, which is roughly the postshock temperature of shocks with velocities of 1000 km s^{-1} (Dopita & Sutherland 2003), and n_7 the number density in units of 10^7 cm^{-3} , which is typical for our adiabatic models. It follows that the cooling time due to bremsstrahlung is comparable to the propagation time of the jet (see section 3.3). This implies that radiative cooling is important for the employed jet model parameters and should be included in the energy equation.

Synchrotron emission should be present due to the acceleration of electrons in the shocks and the presence of local magnetic fields in the plasma. With a power-law energy distribution of the electron $N(E) dE = E^{-\kappa} dE$, the spectral index of the resulting spectrum of the emission is $\alpha = (\kappa - 1)/2$ (Rybicki & Lightman 1979) and the total emissivity of synchrotron radiation can be estimated to

$$j = \epsilon_s p B^{1+\alpha} = \epsilon_s \beta p^{(3+\alpha)/2} \quad (3.4)$$

with an assumed spectral index $\alpha = 0.6$ (Saxton, Bicknell & Sutherland 2002), ϵ_s the normalization of the power-law and $\beta < 1$ the proportionality factor of equipartition. Both parameters are quite unclear, therefore these results are only qualitative.

According to Aller (1984), we can use only those grid cells to estimate the H I line emission, where the temperature is larger than 10^4 K and where only recombination contributes to the emission. Hydrogen is assumed to be fully ionized. The emissivity is then

$$j = 4.16 \cdot 10^{-25} T_4^{-0.983} 10^{-0.0424/T_4} n_e n_i \text{ erg s}^{-1} \text{ cm}^{-3} \quad (3.5)$$

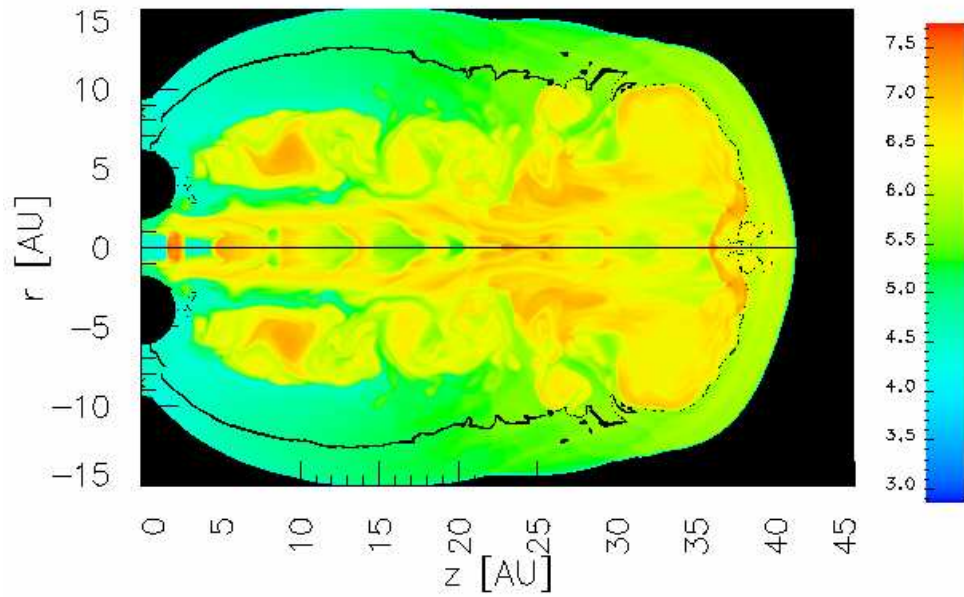


Figure 3.20: Logarithm of temperature of the model i; temperatures are present in the range of 10^3 K in the red giant wind, of 10^5 K in the shocked ambient medium and up to 10^8 K in the jet beam and the cocoon

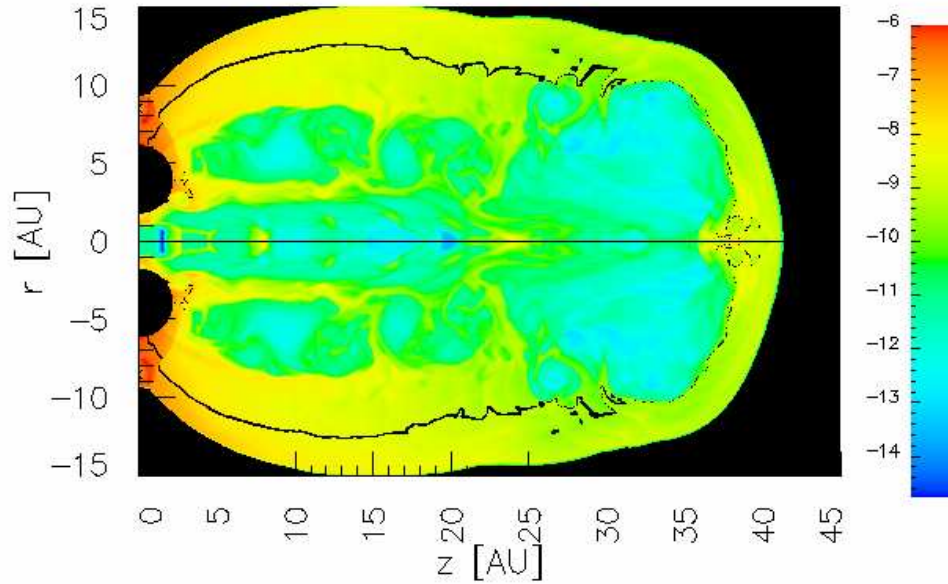


Figure 3.21: Logarithm of Bremsstrahlung emission of the model i in $\text{ergs}^{-1}\text{cm}^{-3}$; although the temperature is lower in the shocked ambient medium than in the cocoon and jet beam, the bremsstrahlung of the latter two regions dominate due to the high densities there

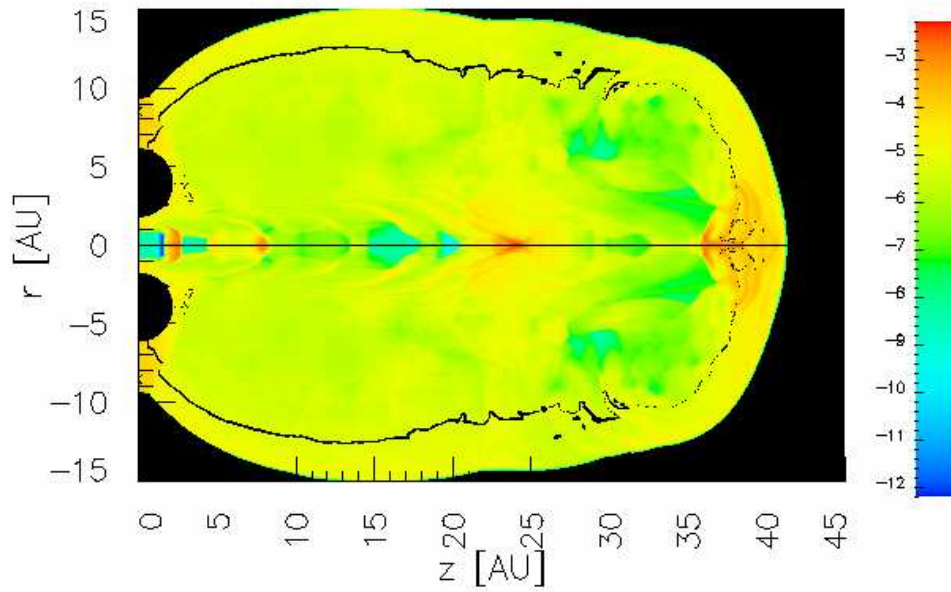


Figure 3.22: Logarithm of Synchrotron emission of the model i in $\text{erg s}^{-1}\text{cm}^{-3}$; ϵ_s is set to unity, which leads to overestimations of the emission

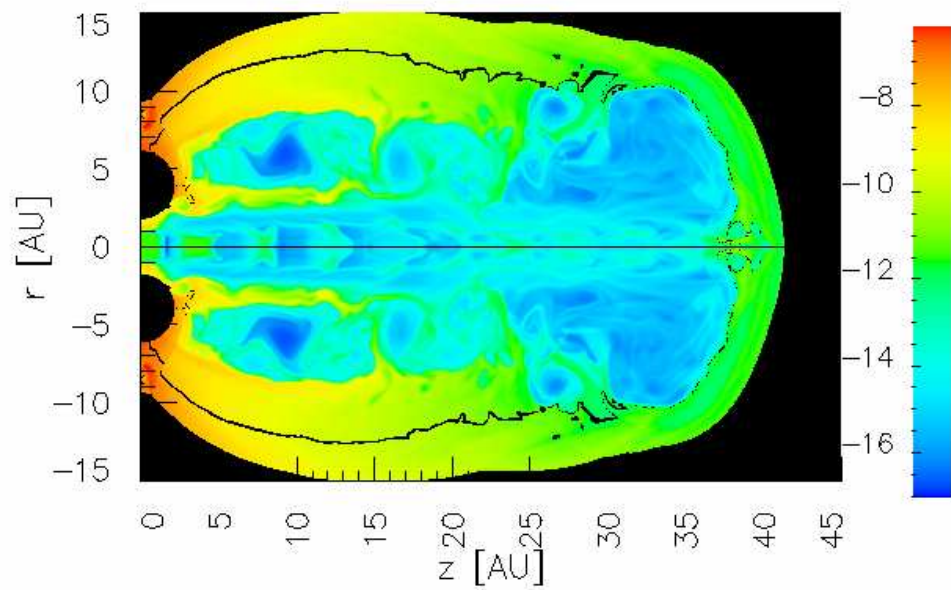


Figure 3.23: Logarithm of H I line emission of the model i in $\text{erg s}^{-1}\text{cm}^{-3}$; in regions with high temperatures – the cocoon and the jet beam – the optical emission is suppressed, the main contribution is the shocked ambient medium near the red giant

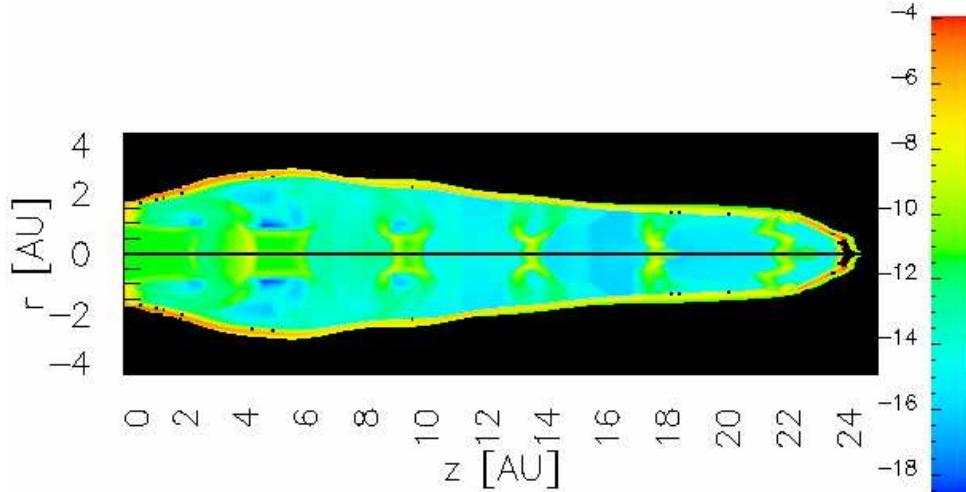


Figure 3.24: Logarithm of Bremsstrahlung emission of the model i with cooling in $\text{erg s}^{-1} \text{cm}^{-3}$; the shocked ambient medium collapsed, therefore the emission features of the jet beam are visible in the whole jet width

with T_4 the temperature in units of 10^4 K. In Figures 3.21 - 3.23, the logarithm of the Bremsstrahlung, synchrotron and HI line emission, respectively, is plotted for the model i. In all plots, it is obvious that the emission of the cocoon and the shocked ambient gas is comparable or even larger than that of the jet.

The total luminosity calculated from the emission maps is much higher than the initial kinetic luminosity of the jet ($10^{33} \text{ erg s}^{-1}$). This is the case because the majority of the kinetic jet energy which heats the jet gas would go for the resulting high gas density into radiative emission and not into adiabatic expansion of the gas. Thus, the adiabatic model produces far too hot jet gas, and therefore the emission is grossly overestimated. Thus, we have to conclude that the present model parameters are not appropriate for an adiabatic simulation. For models with lower density the real physical situation should be closer to the adiabatic case, as radiative cooling scales with the density squared. Thus the emission map presented here could still be at least qualitatively meaningful for lower density jet outflows from symbiotic systems.

3.5.2 The model with radiative cooling

The most important difference in the emission maps between models with cooling and models without cooling is, that the cocoon has a significantly smaller extent in the former. Having a much reduced emission from only a small, narrow cocoon enhances the prospect for detecting bright knots in the emission maps (Figs. 3.24 - 3.26), which are due to internal shocks in the jet beam.

In the purely hydrodynamical models the cocoon emission is dominant and may prevent the observation of the jet beam structure. For the model with cooling, the integrated luminosities at day 74 are:

$$\begin{aligned} L_{\text{Bremsstrahlung}} &= 1.15 \cdot 10^{33} \text{ erg s}^{-1} \\ L_{\text{HI}} &= 6.96 \cdot 10^{32} \text{ erg s}^{-1} \end{aligned}$$

L_{HI} accounts only for the HI recombination emission. The total cooling emission in all emission lines is certainly higher. Thus the dominant cooling radiation should be atomic emission lines.

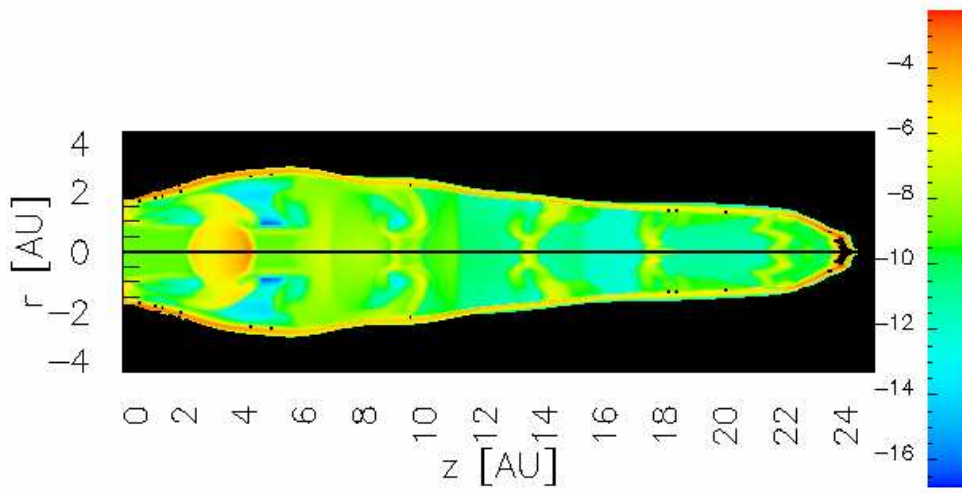


Figure 3.25: Logarithm of synchrotron emission of the model i with cooling in $\text{erg s}^{-1} \text{cm}^{-3}$

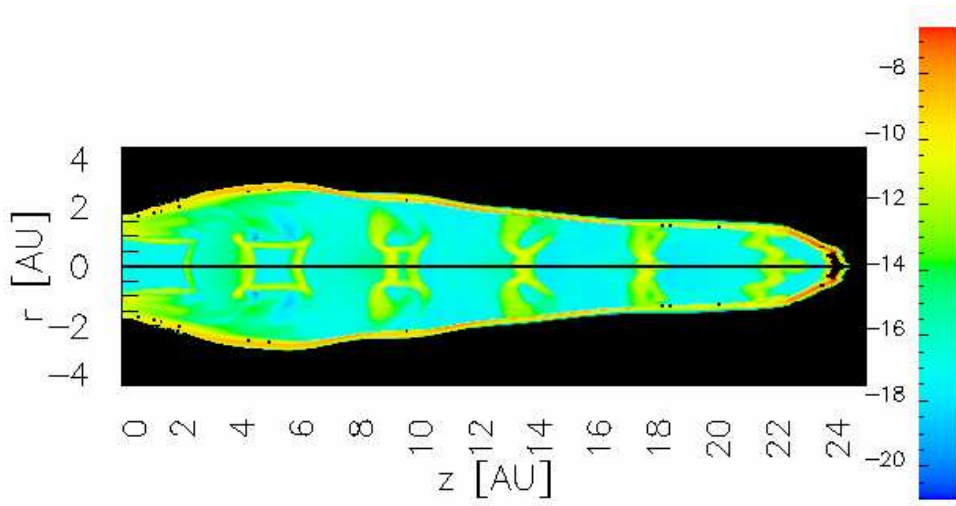


Figure 3.26: Logarithm of H I line emission of the model i with cooling in $\text{erg s}^{-1} \text{cm}^{-3}$

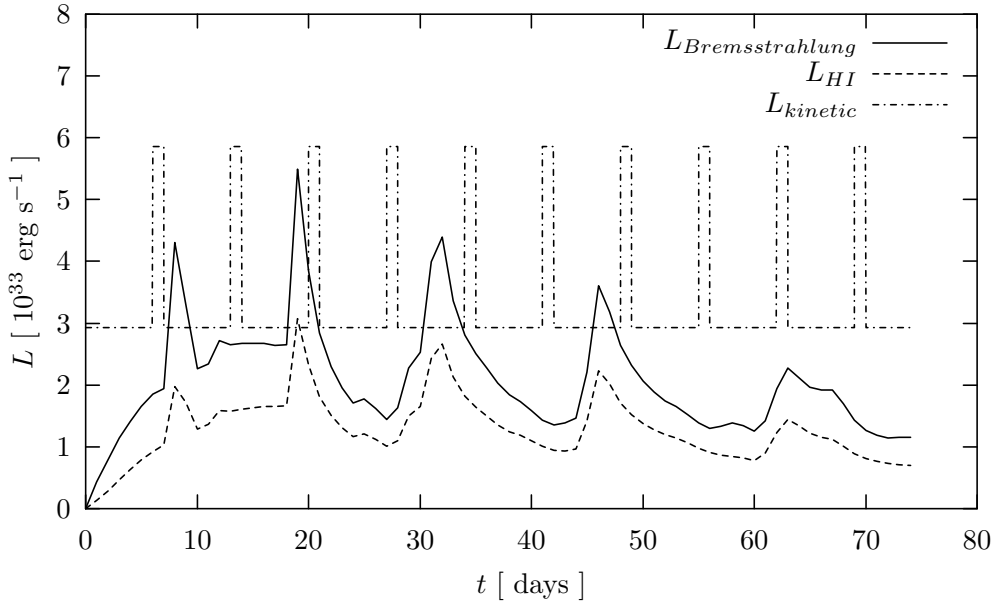


Figure 3.27: Evolution of the kinetic, bremsstrahlung and HI luminosity

For the comparison of the emission map with observations it should be considered, that the HI map is not representative for all optical lines. For example emission from collisionally excited lines like Ca II is only expected from the very coolest $T < 15000$ K regions in the jet knots. No emission would come from the hot jet beam or the cocoon, because there Ca would be in a higher ionization state than Ca^+ . Thus the knot structure may be particularly well defined in such low ionization lines. Similar selection effects must be considered for the observations of the Bremsstrahlung radiation. Thermal free-free radiation in the radio range would strongly favor the low temperature emission regions, such as the dense knots, while the Bremsstrahlung radiation observable with X-ray telescope would only originate from the very hottest, low density regions in the hot beam or the cocoon. The map for the Bremsstrahlung simply includes the emitted radiation in all wavelength bands. Fig. 3.27 shows the evolution of the kinetic, bremsstrahlung and HI luminosity until day 74. The emitted luminosity is about 50 per cent of the kinetic luminosity. The peaks in the emitted luminosity coincide with the merging of the pulses with the bow shock (see Fig. 3.15).

3.6 Discussion I

3.6.1 Model calculations

Pulsed jet models for parameters representative for symbiotic systems were described. Two main types of simulations were performed, a small model grid for adiabatic jets with different jet pulse parameters and one simulation including radiative cooling.

For the adiabatic jet models some quantitative differences are present for the different pulse parameters, but qualitatively the model results are very similar.

Huge differences can, however, be seen between the adiabatic models and the model which includes radiative cooling. Compared to the adiabatic models the most important effects induced by radiative cooling are:

- The energy loss through radiation lowers the pressure and the temperature which leads to a much smaller lateral extension of the jet, so that the cross section and the resistance

exerted by the external medium is strongly reduced leading to a significantly higher bow shock velocity.

- The internal structure of the pulsed jet with cooling shows a well defined periodic shock structure with high density, low temperature knots separated by hot, low density beam sections. Contrary to this in the adiabatic jet the hottest regions have the high density while the density is low in cool regions. The temperature and density contrast is much more pronounced in the models with cooling.

These differences are generic for model results from jet simulation without and with cooling. For the particular model i described here we can now quantify these differences.

- The jet radii are 10 AU for the adiabatic jet and 2.5 for the jet with cooling. These values are determined for model jets with the same axial length of 24 AU.
- The bow shock velocity after 74 days is about 200 km s^{-1} in the adiabatic model compared to 730 km s^{-1} in the cooled jet.
- The gas temperature in the adiabatic jet is everywhere (except for the initial jet gas in the nozzle) higher than $T \approx 2 \cdot 10^5 \text{ K}$ and goes up to $T \approx 10^7 \text{ K}$ in the high density shock regions. In the jet model with cooling the temperature is really low $T \approx 10^4 \text{ K}$ in the cool, high density knots. The hot beam regions have $T \gg 2 \cdot 10^5 \text{ K}$.
- The density contrast between cool and hot regions is about a factor of 30 in the adiabatic jet, but a factor of 1000 in the jet with radiative cooling. Note that high density regions are hot in adiabatic models, while they are cool in the models with cooling.

These huge differences show clearly that adiabatic jet models are far from reality if radiative cooling is indeed important. Therefore jet models with radiative cooling should be investigated in much more detail for the high jet gas densities encountered in symbiotic systems.

Unfortunately, the time scales of cooling processes are several orders of magnitude shorter than those of hydrodynamical ones. This is a large numerical problem which is demanding high computational costs. But as mentioned above, these costs are necessary to get new insights into the physics of jets in symbiotic stars.

Until now, only two-dimensional simulations have been performed, also due to high computational costs and memory demands of 3D-simulations. In those simulations, the red giant would be taken into account correctly, not as a ring, and its influences on the jet, the gravitation and the stellar wind, would not be symmetric anymore. This would result in the backflow being blocked only in a small segment, therefore the jet should be turbulent from the beginning.

As Kössl & Müller (1988) and Krause & Camenzind (2001) have shown in their simulations, the numerical resolution determines, whether one sees the transition from the laminar to the turbulent phase or not. Also in our simulations, this transition can be seen, implying that the resolution here is not too small. An increased resolution should not change the main result, the shrinking of the cocoon and the necessity of performing hydrodynamical simulations with cooling to understand the structure and emission of jets in symbiotic stars.

3.6.2 Comparison with symbiotic systems

Our model calculations make various predictions for jets in symbiotic systems. We focus here on the basic question whether the observations of symbiotic systems support more the adiabatic jet model or the jet model with cooling.

For MWC 560 the spectroscopic observations show strong absorptions from low ionization species such as Ca II, Fe II and Na I. Absorptions from neutral or singly ionized metals are only expected for cool gas with temperatures around $T \approx 10000 \text{ K}$ or lower. The strength of these absorptions suggest that a substantial fraction of the jet gas must be in this cool state as in the jet model with cooling. This is incompatible with the hot gas temperatures $T \gg 10^5$ present in

adiabatic models. The presented adiabatic jet models are not able to produce low temperature regions.

The propagation of the jet bow shock was well observed for the outburst in CH Cyg. The jet expansion was linear and fast $\approx 1500 \text{ km s}^{-1}$ producing after one year a narrow jet structure with an extension well beyond 300 AU. The estimated jet gas temperature was found to be below 10000 K. This is again in very good agreement with the jet model with cooling. According to our models an adiabatic model is expected to produce a jet with a lower expansion velocity, a broader jet beam emission and most importantly only high temperature jet gas. For CH Cyg it must be said that the initial jet conditions “at the nozzle” are not known.

Less clear is the situation in R Aqr. Although jet features can be traced down to a distance of less than 20 AU, it is not clear whether the jet gas is cool or hot. A proper motion for the emission features in the range 36 to 240 km s^{-1} has been derived. This would be more in the range of the gas motion of the adiabatic models. However it is not clear from where the observed emission originates, from the jet gas or the surrounding gas excited by shocks induced by the jet propagation. The small jet opening angle of 15° favors more a jet with cooling, but a strong disk wind or a steep density gradient for the circumstellar gas may also help to enhance the collimation of an adiabatic jet.

Thus, the comparison between model simulation and observations suggest strongly that radiative cooling is important for jets in symbiotic systems. The fact, that the model with cooling describes the observations better than those without cooling, means that the cooling time scale in the jet of symbiotic systems must be shorter than the propagation time scale (i.e. expansion time scale of the adiabatic gas) which is of the order of hundred days. This condition sets a lower limit for the density inside the jet of about $n \approx 10^6 \text{ cm}^{-3}$ ($T \approx 10^4 \text{ K}$) which is consistent with our initial parameters.

Chapter 4

Theoretical absorption line profiles

Based on our hydrodynamic simulations of pulsed jets with model parameters representative for MWC 560 we calculate and discuss synthetic absorption profiles.

4.1 Model calculation

4.1.1 Absorption profiles

Using the results from the hydrodynamical simulations, we calculate the absorption line structure.

As emission region we define a disk in the equatorial plane ($z = 0$) which extends to a radius r_{em} . For each grid cell within this region, we assume a normalized continuum emission and a Gaussian emission line profile:

$$I_0 = 1 + I_{\text{peak}} \cdot \exp(-v^2/\sigma^2). \quad (4.1)$$

This initial intensity is taken to be independent of position $r < r_{\text{em}}$.

Further we consider the possibility of different system inclinations i for the calculation of light rays from the emission region through the computational domain. We consider only absorption along straight light travel paths and neglect possible additional emission or scattering inside the jet.

The initial continuum and line emission (4.1) is taken as input for the innermost grid cell of each path. We then calculate the absorption within each grid cell j along the line of sight according to:

$$\begin{aligned} I_j &= I_{j-1} \cdot e^{-\tau_\lambda} \\ \tau_\lambda &= \frac{\pi e^2}{m_e c} \lambda_{kl} \left(1 - \frac{v_j}{c}\right) \frac{\rho_j \eta}{m_H} \Delta x_j f_{kl} \\ &= C_{kl} \Delta x_j \mathcal{F}(v_j, \rho_j), \end{aligned} \quad (4.2)$$

where e is the electron charge, m_e the electron mass, c the speed of light, λ_{kl} the rest frame wavelength of the transition, m_H the proton mass and f_{kl} the oscillator strength. The parameters are constant for a given atomic transition. Δx_j is the length of the path through grid cell j which is a function of the inclination i .

The parameters depending on the different hydrodynamical models are the velocity projected onto the line of sight v_j , the mass density ρ_j and η the relative number density with respect to hydrogen $\eta = n_k/n_H$ of the absorbing atom in the lower level k of the investigated line transition. The velocity is binned for the calculation of the absorption. The size of the bins Δv can be interpreted as a measure of the kinetic motion and turbulence in one grid cell. This absorption dispersion helps to smooth the effects of the limited spatial resolution of the numerical models.

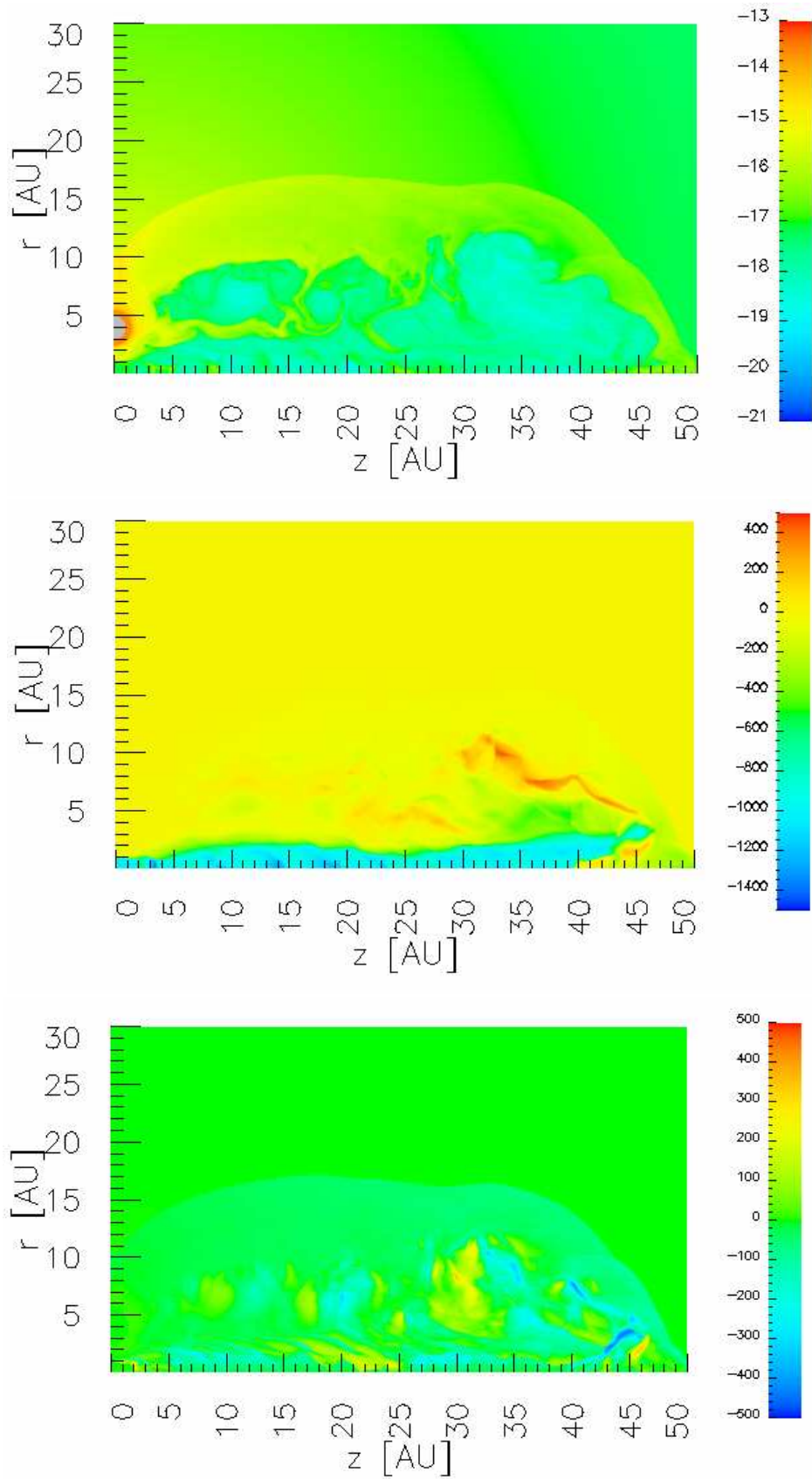


Figure 4.1: Adiabatic model i for a pulsed jet at day 444: Color plots of the logarithm of density in g cm^{-3} (top), of the velocity components parallel (middle) and perpendicular (bottom) to the jet axis

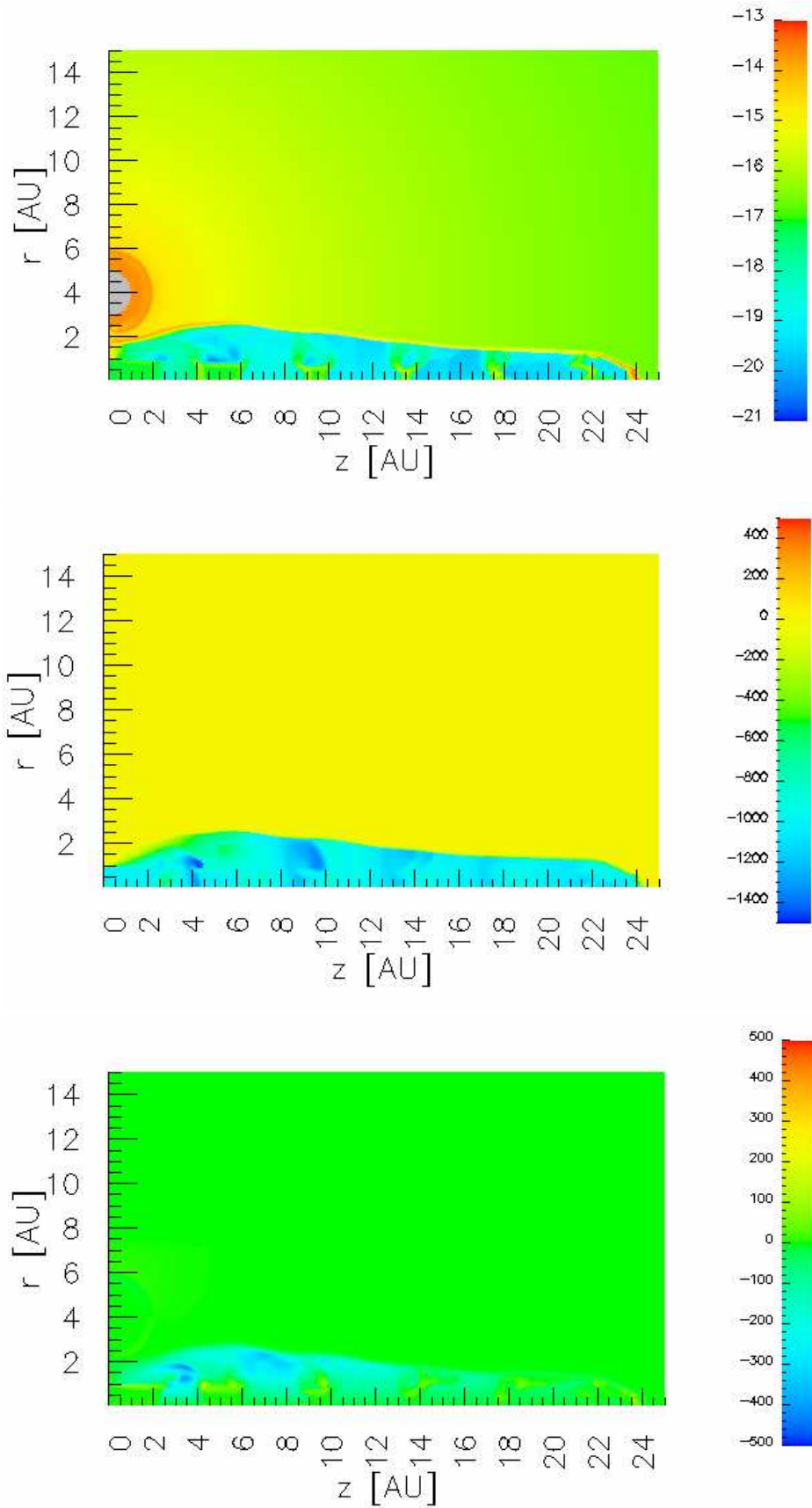


Figure 4.2: Pulsed jet model i with radiative cooling at day 74: the same quantities as in Fig. 4.2 are plotted.

The absorption calculation through the jet region is repeated for all possible light paths from the emission region to the observer. The arithmetic mean of the individual absorption line profiles from all path is then taken as resulting spectrum.

4.1.2 Model parameters

The quantities determining the absorption line profiles are, first, the parameters defining the hydrodynamical model. These are pulse velocity, pulse density and the time (day) in the simulation. For model i we have to distinguish further between adiabatic calculation and calculations including radiative cooling.

Second, for the emission from the jet source, the size of the emission region r_{em} must be fixed. For the emission spectrum we adopt a normalized continuum and an emission line component at rest velocity (the same transition as the calculated jet absorption line) with $I_{\text{peak}} = 6$, $\sigma = 100 \text{ km s}^{-1}$. An additional parameter is the inclination i under which the system is seen.

The parameters of the absorbing transition are defined by the rest wavelength λ_{kl} , the oscillator strength f_{kl} and the population of the absorbing atomic level $\eta = n_k/n_{\text{H}}$. Further we have to define the velocity bin size Δv which is a measure for the adopted turbulent (and kinetic) motion of the absorbers.

4.2 Results for different model parameters

The structure of the synthetic absorption profiles reflect in a certain way the hydrodynamical structure of the jet outflow. The hydrodynamical variables determining the absorption profile are the density and the velocity projected onto the line of sight. The density, the velocity component parallel and the velocity component perpendicular to the jet axis are plotted in Fig. 4.1 for an adiabatic model at day 444 and in Fig. 4.2 for a model with radiative cooling at day 74. Both models are based on the same jet pulse parameters (model i) $v_{\text{pulse}} = 2000 \text{ km s}^{-1}$ ($2\times$ the normal value) and a pulse density of $n_{\text{pulse}} = 1.25 \cdot 10^6 \text{ cm}^{-3}$ ($1/4\times$ the normal value). The adiabatic jet produces a very extended and highly structured jet cocoon. Contrary to this the model i with radiative cooling produces an almost “naked” jet beam with practically no jet cocoon, but with a well defined and sharp transition towards the ambient medium.

In the adiabatic model (Fig. 4.1) four different velocity regions can be distinguished:

- I the jet beam with high outflow velocities of -800 to -1400 km s^{-1} ,
- II the cocoon and bow shock region with velocities of -10 to -800 km s^{-1} ,
- III the external medium, the companion star and its wind with velocities around 0 km s^{-1} , and
- IV the backflow near and besides the jet head with velocities of 0 to $+500 \text{ km s}^{-1}$.

In the jet models with radiative cooling there exists neither an extended cocoon and bow-shock region nor a backflow region. These regions are compressed into a narrow transition region between jet beam and external medium due to the high density and the efficient cooling. Thus the model with cooling essentially has only two velocity regions: I — the jet beam, and III — the external medium (Fig. 4.3).

4.2.1 Size of the emission region and system inclination

We first investigate the effect of the emission region size r_{em} and the inclination i on the the synthetic absorption line profiles. For this we employ the adiabatic pulsed jet model i at day 444 shown in Fig. 4.1.

For the atomic transition we use the parameters $\lambda_{kl} = 3934 \text{ \AA}$, $f_{kl} = 0.69$ and $\eta = 2 \cdot 10^{-6}$ appropriate for the Ca II K transition. For η we just assumed that all Ca-atoms are in the ground

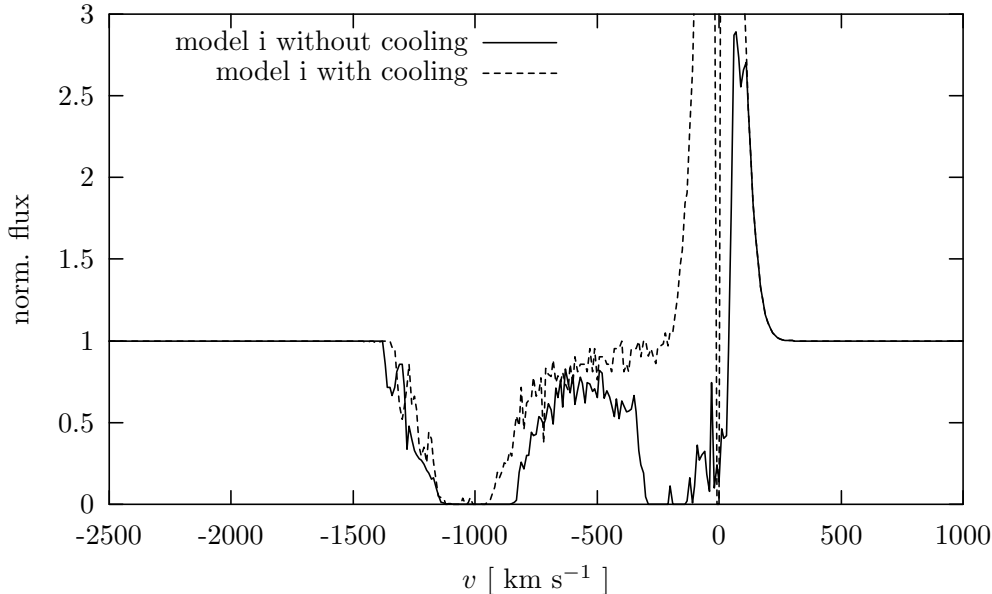


Figure 4.3: Four different absorption regions in the adiabatic model i caused by the jet beam, the bow shock region, the external medium and the backflow. In model i with cooling only the jet beam and the external medium are clearly visible, while the bow shock region creates only a slight absorption and no backflow is present

state of Ca^+ . This is useful for the investigation of the expected absorption line structures introduced by the different velocity regions. However, the gas temperature in the adiabatic models is far too high to have Ca in the form of Ca^+ . This will be discussed in Sect. 4.2.3. The velocity bin width for the calculation of the absorption profiles is set to $\Delta v = 10 \text{ km s}^{-1}$. The parameters for the emission line component in the initial spectrum are $I_{\text{peak}} = 6$ and $\sigma = 100 \text{ km s}^{-1}$.

In Fig. 4.4 the synthetic absorption profiles are given for different radii $r_{\text{em}} = 1, 5, 10 \text{ AU}$ of the disk-like emission region for model i. The system inclination is set to $i = 0$, therefore the projected velocity is equal to the velocity component parallel to the jet axis.

For $r_{\text{em}} = 1 \text{ AU}$ mainly the gas inside the jet beam (region I) with $v = -800$ to -1400 km s^{-1} produces absorptions. In addition there is strong absorption from the bow shock region (II) in the velocity range $v = 0$ to -350 km s^{-1} . The external medium (III), in front of the bow shock, finally absorbs the peak of the emission line. No signature from the backflow region (IV) is visible and therefore the red wing of the emission line is unaffected by absorption.

For an emission region with $r_{\text{em}} = 5 \text{ AU}$ a substantial fraction of the source light passes through the cocoon (II) and the backflow region (IV). Correspondingly the absorption in the velocity range $v = 0$ to -800 km s^{-1} is substantial and also the entire emission line is strongly suppressed including the red wing. On the other hand the high velocity component $v = -800$ to -1400 km s^{-1} is averaged out and therefore less strong because much of the light from the source passes no more through the fast jet beam (region I).

This trend continues for even more extended emission regions ($r_{\text{em}} = 10 \text{ AU}$). Dominant are the low velocity absorptions $v = 0$ to -200 km s^{-1} from the outer cocoon. Also clearly visible is the absorption from the backflow region extending to $v \approx +200 \text{ km s}^{-1}$.

In Fig. 4.5 the synthetic absorption profiles are given for different radii $r_{\text{em}} = 1, 2, 3 \text{ AU}$ of the disk-like emission region for the model i with cooling. For $r_{\text{em}} = 1 \text{ AU}$ the gas inside the jet beam (region I) with $v = -800$ to -1300 km s^{-1} produces absorptions. The external medium (III), in front of the bow shock, absorbs the peak of the emission line. For higher values of r_{em} no additional structure appears, but the high velocity component is averaged out and therefore less

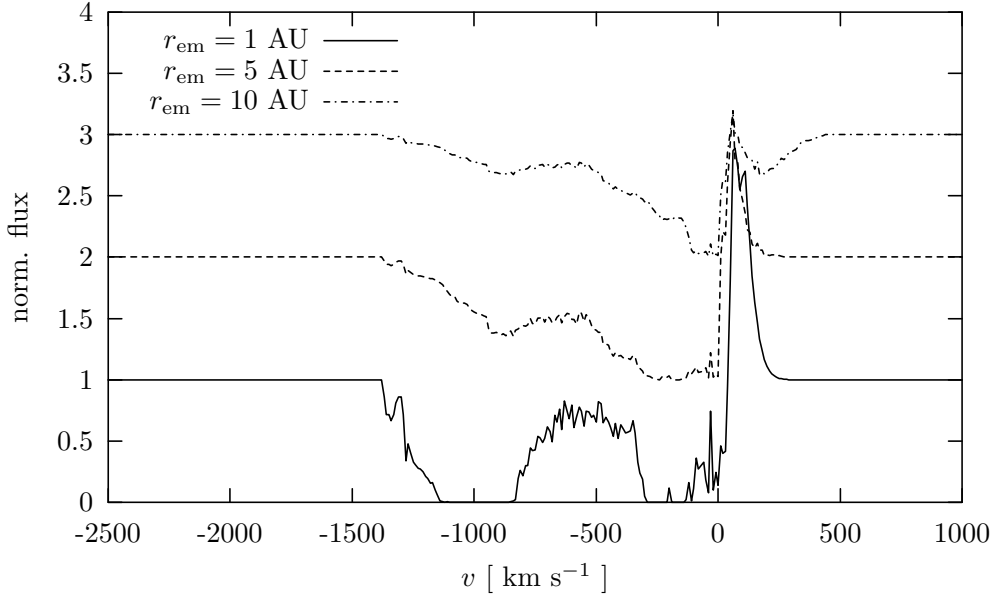


Figure 4.4: Synthetic absorption line profile for three different radii $r_{\text{em}} = 1, 5, 10$ AU of the emission region. Calculations for adiabatic model i (Fig. 4.1) and inclination $i = 0^\circ$. The appearance of different absorption components created in the jet beam and the cocoon and averaging effects are detectable.

strong.

The absorption line structure depends also on the system inclination as shown in Fig. 4.6 for model i without and in Fig. 4.7 for model i with cooling. In the first figure the synthetic spectra are compared for the inclinations $i = 0^\circ, 3^\circ$ and 6° for an emission region of radius $r_{\text{em}} = 1$ AU. For $i = 3^\circ$ and $i = 6^\circ$ the absorption components are redistributed in comparison to the $i = 0^\circ$ -case, because then other regions, e.g. of the cocoon and the backflow, are along the line of sight while regions in the jet beam at large z are missed.

In the case of model i with cooling, a new effect occurs. In Fig. 4.7 a region of lessened absorption appears and splits the main absorption component into two distinct components.

The equivalent width (EW) of the jet absorption depends correspondingly to the profile changes on the emission region size and the system inclination. This is shown in Fig. 4.8, where contours for the equivalent width in the i - r_{em} -plane are plotted. The calculation of EW for this plot considers only absorptions of the emission line free continuum region. The highest EW are obtained for compact emission region $r_{\text{em}} < 1.5$ AU and inclinations below about 12° . Important for a large equivalent width is that the line of sights pass through regions with different (evenly distributed) line of sight velocities. The jet/cocoon regions have the most diverse velocity distribution. These regions are missed by a substantial fraction of the line of sights for high inclination or extended emission regions resulting in a small EW.

4.2.2 The velocity bin size

The velocity structure in the synthetic jet absorption profile represents an average of the jet which is limited by the spatial resolution. The real velocity structure inside one grid cell is certainly more complex, mainly due to turbulent small scale gas motions. Therefore the discrete velocity value for the absorption of one grid cell should be replaced by a velocity dispersion. The strength of this dispersion, however, is not known. Thermal motion in our temperature regime leads to values of about 10 km s^{-1} , turbulence can increase them to 50 km s^{-1} and more. The effect of such

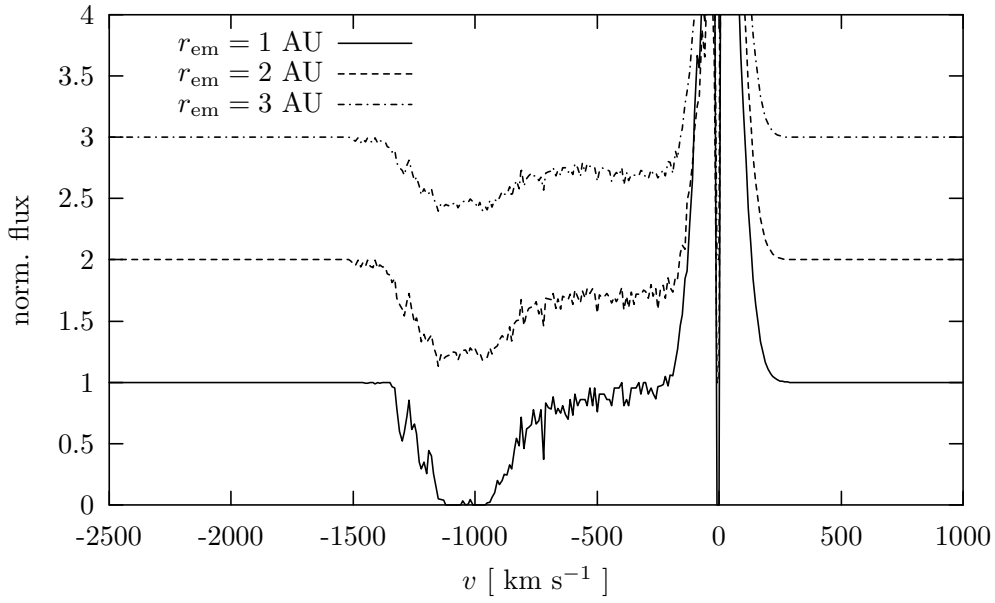


Figure 4.5: Synthetic absorption line profile for three different radii $r_{\text{em}} = 1, 2, 3$ AU of the emission region. Calculations for model i with cooling (Fig. 4.2) and inclination $i = 0^\circ$.

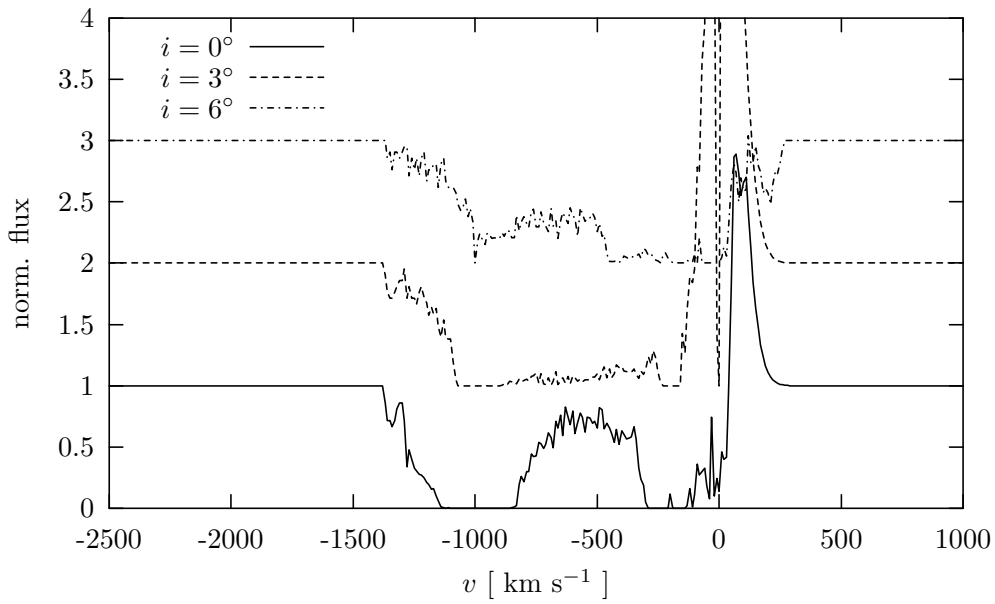


Figure 4.6: Synthetic absorption line profile for the adiabatic model i seen under the inclination $i = 0^\circ, 3^\circ$ and 6°). The radius of the emission region is $r_{\text{em}} = 1$ AU. The appearance of the intermediate velocity components from the cocoon (for $i = 3, 6^\circ$) and the backflow component IV (for $i = 6^\circ$) is visible.

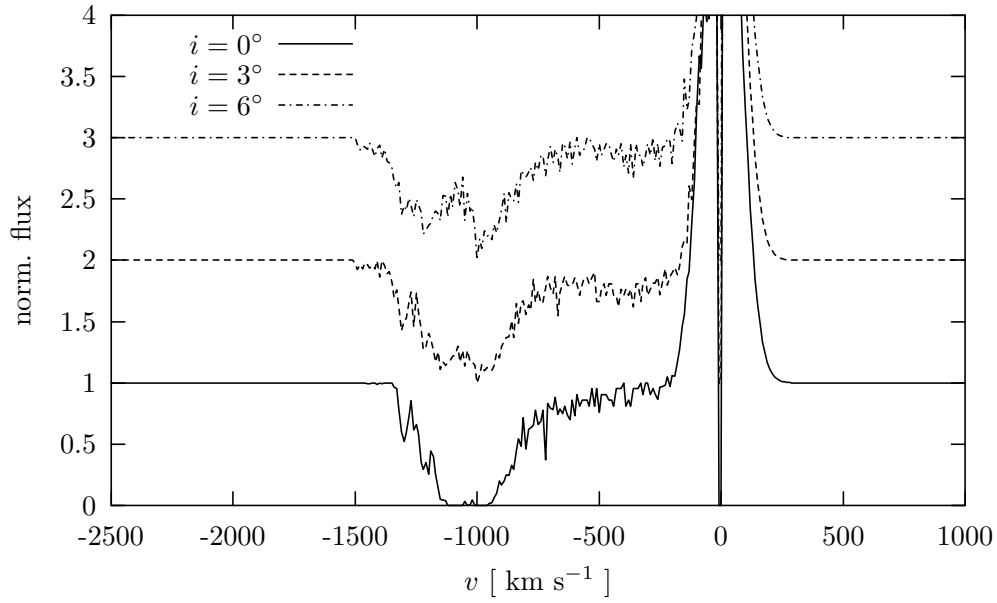


Figure 4.7: same as Fig. 4.6, but for model *i* with cooling. The splitting of the main absorption component into two distinct components with increasing system inclinations is visible.

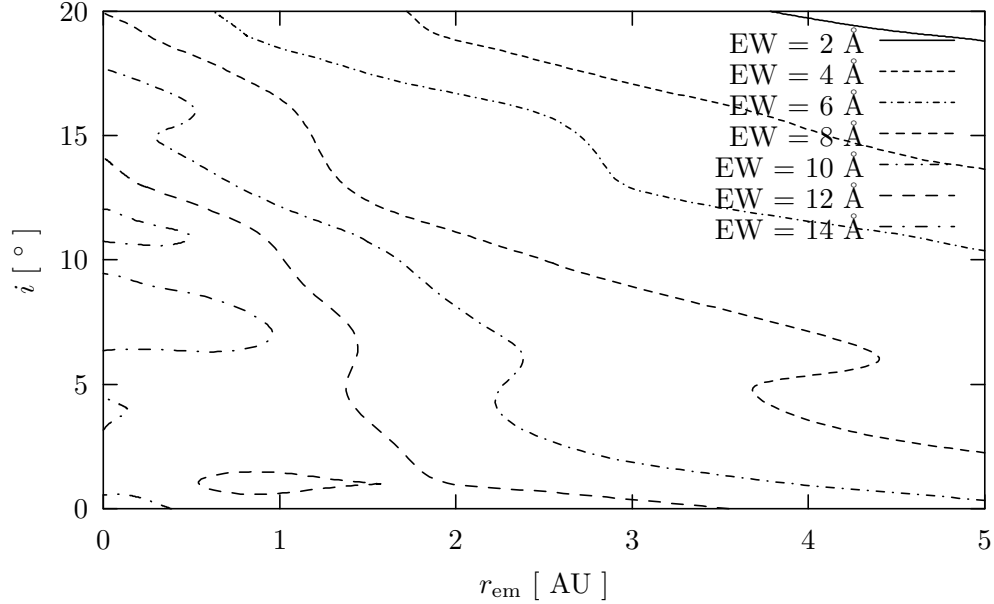


Figure 4.8: Equivalent width of the jet absorption. Contour plot of the equivalent width in the i - r_{em} -plane for adiabatic model *i*.

a velocity dispersion can be considered in the calculation of the absorption line by the binning of the velocities into broader bins. However, one has to assure – by correcting the optical depth calculated in equation (4.2) – that the EW is not affected by an enlarged Δv . For broader velocity bins, simulating a larger velocity dispersion of the absorbing atoms, a smoother jet absorption profile with less structure is obtained as shown in Fig. 4.9.

4.2.3 The ionization problem

In all the jet absorption profile calculations in the previous sections we have assumed that all Ca atoms are singly ionized. However, the gas temperature in the adiabatic models is far too high for Ca^+ -ions. Assuming collisional ionization equilibrium, Ca^+ would be the dominant ionization stage for $T_e < 15000$ K. The relative abundance Ca^+/Ca is less than 1 % for $T_e > 25000$ K or less than 0.01 % for $T_e > 250000$ K. After fitting the ionization balances from Sutherland & Dopita (1993) with

$$\eta(T) = \eta(0) \frac{1}{\exp(T/1000 - 14) + 1} \quad (4.3)$$

and introducing this into the calculation, for our adiabatic model no absorption is present if ionization equilibrium is considered for the Ca^+ abundance (Fig. 4.10, top). In the model with cooling, the absorption is weakened but still present (Fig. 4.10, bottom). The absorption generated by material which is cooler than 10^5 K is of the order of 4 % in the adiabatic model i, while around 60 % in the model with cooling. Even below 3×10^4 K we consider 48 % of the absorbing material. Therefore the temperature in our model with cooling is only slightly overestimated, while unacceptably high in the adiabatic models.

The much too high temperature of the model jet gas, compared to the observations, could be explained by insufficient cooling. As the cooling is proportional to the density squared, higher density gas in the jet model would cool faster down to the required temperature to account for the observed Ca II absorption. This may be achieved with models having higher gas densities in the jet or pulse. Another possibility is, that high density clumps may form, for which the cooling would be very efficient. However, the spatial resolution of our model grid is too coarse for simulating such small scale structures.

4.3 Time variability of the absorption line

As next step the temporal evolution of the highest velocity component is investigated. This “edge” velocity for the variable absorption originates from the most recent pulse, close to the jet nozzle, which is not yet slowed down as much as the previous pulses. As this gas is located close to the continuum emission region, the corresponding absorption feature is present for all viewing angles considered and essentially independently from the size of the emission region.

In Fig. 4.11, the maximum outflow (negative) velocity of the high velocity component is plotted between day 360 and 380 for the eight adiabatic models and between day 50 and 74 for the one with cooling. The first result is the fact, that pulses without velocity enhancements (only density changes) as investigated in the four adiabatic models v to viii, produce hardly any velocity effects. The velocity variations created by interactions between different density regions in the jet are only of the order of a few 10 km s^{-1} and only in the model v, where the density in the pulse is the smallest. It seems unlikely that high velocity components can be produced by density jumps in the jet outflow.

The simulations with high velocity pulses show all a qualitatively similar behavior, with a sudden outflow (negative) velocity increase to the pulse velocity of -2000 km s^{-1} followed by a velocity decay during the following days. Closer inspection of the evolution of the high velocity component shows some differences between the four adiabatic models i – iv to the model i with cooling. In the latter, the velocity drops within one or two days from the initial -2000 km s^{-1} to -1400 km s^{-1} and then much slower – apparently asymptotically – to a stationary value of -1300

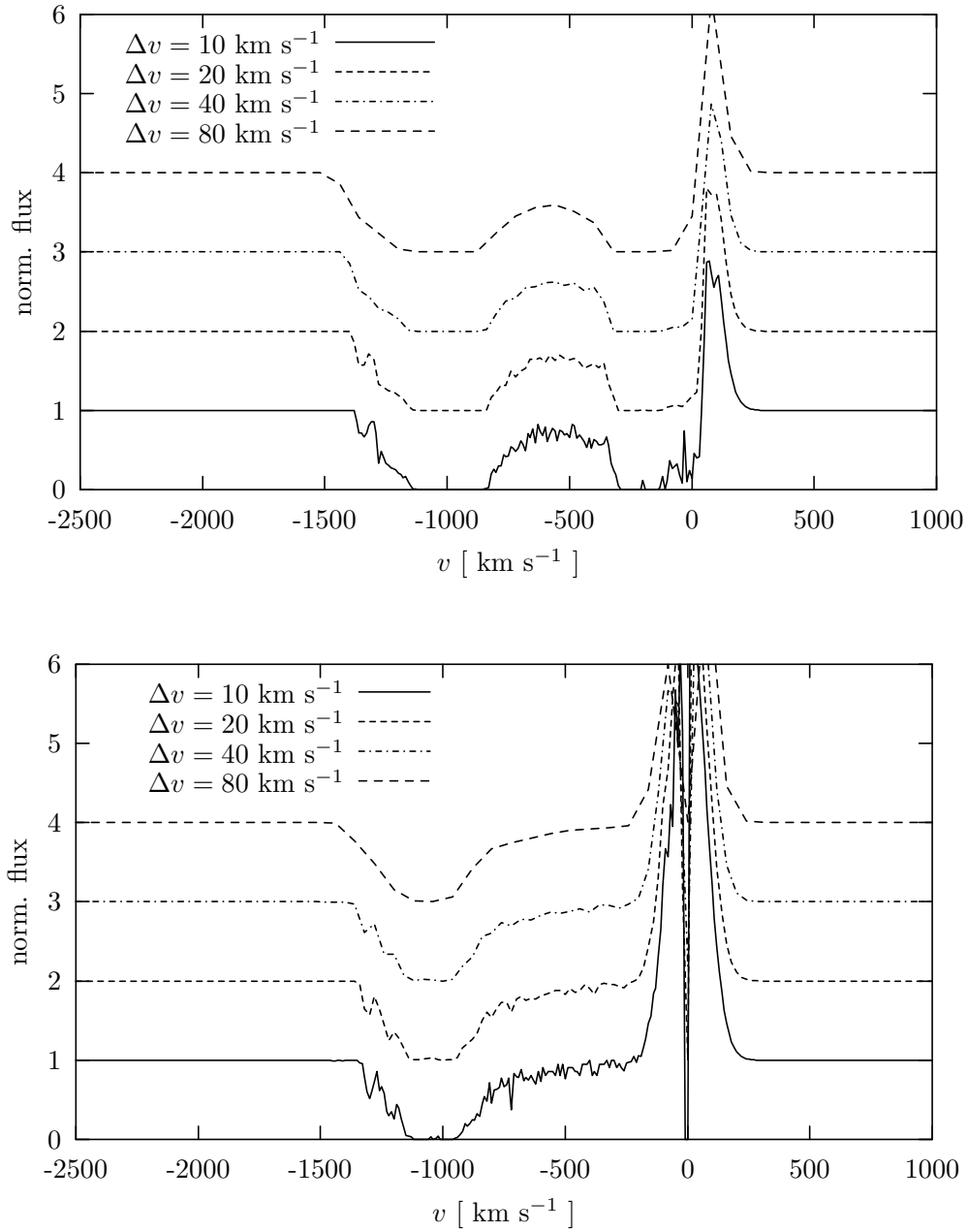


Figure 4.9: Theoretical absorption line profiles for values of the velocity bin size Δv (10, 20, 40, 80 km s⁻¹) for adiabatic model i (top) and for model i with cooling (bottom); higher velocity dispersions lead to smoother spectral absorption structures.

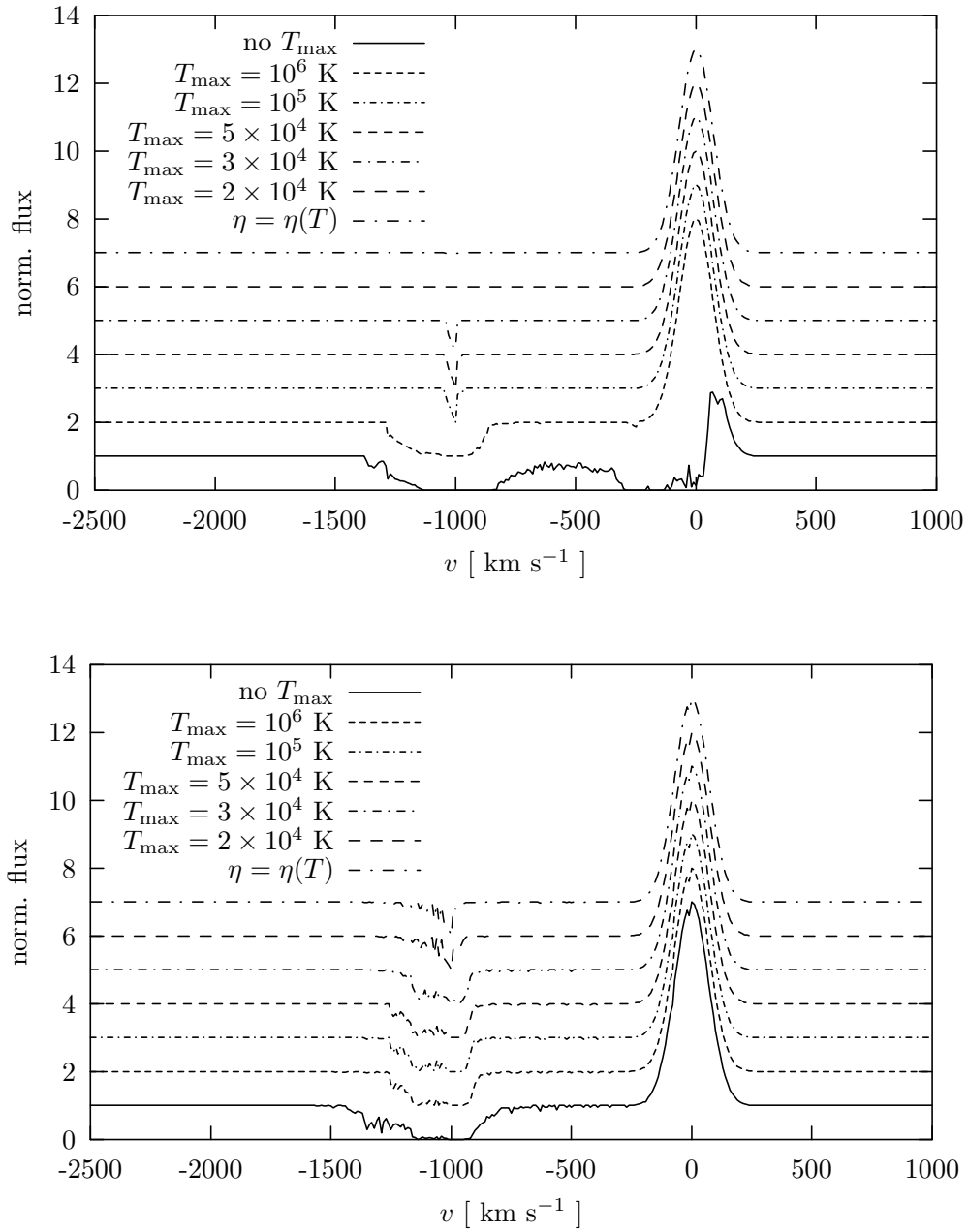


Figure 4.10: Theoretical absorption line profiles of the adiabatic model i (day 444) for different values of the temperature threshold T_{\max} (top) and for the model i with cooling (day 65) with and without a temperature dependent η (bottom); the correct ionization balances $\eta(T)$ lead to no absorptions in the adiabatic case

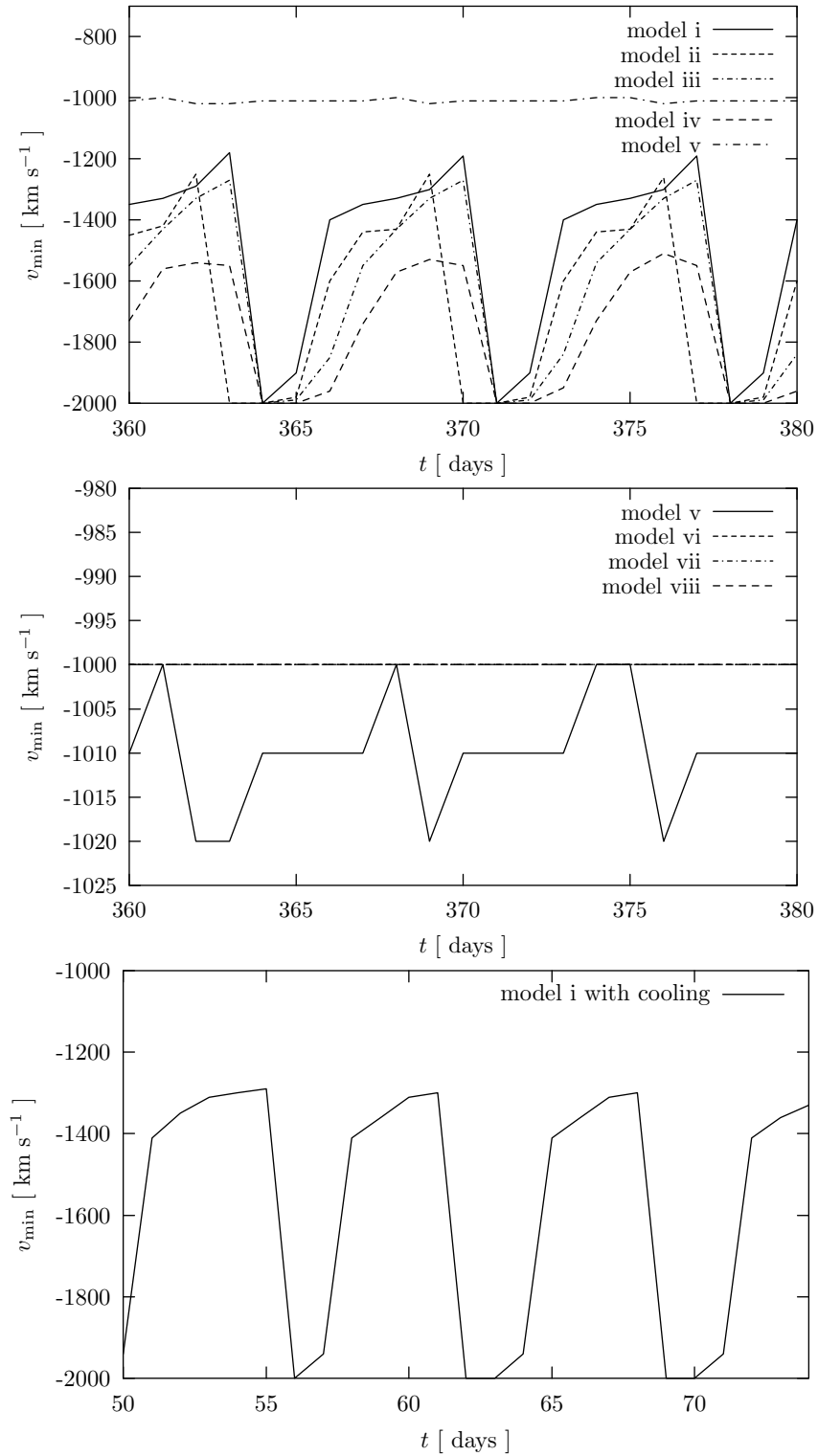


Figure 4.11: Time variability of the high (negative) velocity component for models i-v (top), for models v-viii (middle) as an enlargement (note the different scale of the y axis) and for model i with cooling (bottom)

km s⁻¹ during the next four days. In the adiabatic model i, the first drop is similar, but the slow decay seems to be only a plateau of two days, after that the velocity drops to -1150 km s⁻¹. The model ii shows the same behavior but with higher velocities (-1400 and -1250 km s⁻¹). The last two models iii and iv decay again in an asymptotic manner to -1300 km s⁻¹ and -1550 km s⁻¹, respectively.

4.4 Jet absorption profile: comparison with observations

4.4.1 Jet absorption profile

We construct now, based on our simulations, a fiducial model which reproduces the observed structure and temporal evolution of the jet absorption line profiles. One can directly see that the adiabatic models v - viii can be discarded because they do not show high velocity components in the synthetic absorption line profiles (Fig. 4.11, middle). Thus, we can restrict our further investigation to the four adiabatic models with high velocity pulses i - iv and the model i with cooling.

A major discrepancy in the jet absorption between our simulations and the observations is seen in the velocity region between -300 - 0 km s⁻¹ where the calculated absorption is grossly overestimated.

This feature appears whenever the light path from the emission region to the observer travels through the jet head (bow shock-Mach disk) region (Fig. 4.12). The simulations were stopped when the jet reached the opposite boundary. At this position, the density of the external medium has dropped to the density value of the jet at its nozzle. In reality, the jet would extend further into a region where the density of the external medium is by far smaller. Then the densities in the jet head region also should be smaller and therefore the depth of the absorption. To account for this, we disregard the absorption produced in this region. Thus the calculations of the absorption line profile is only done for the line of sight from $z = 0$ AU to 40 AU in model i and iv, 37.5 AU in model ii and iii in order to cut this region. As already mentioned, this feature does not appear in model i with cooling.

Another qualitative difference between the observations and a subset of model calculations is the occurrence of significant absorption with velocity $RV > 0$ km s⁻¹ visible on the red wing of the emission line (Figs. 4.4 and 4.6). This feature appears in the adiabatic models - but not in model i with cooling - for inclined line of sights $i = 6^\circ$ or extended emission regions $r_{em} = 10$ AU. These absorptions originate in the model calculations in the backflow region (IV). We are not aware, that an absorption component with $RV > 0$ km s⁻¹ has been ever observed in MWC 560. This includes IUE spectroscopy of higher ionization species, like C IV. There are various possibilities which could explain this: (a) no extended backflow region is present in MWC 560, similar to the model i with cooling, (b) the backflow region is too hot (say > 50000 K) to produce intermediate or low ionization absorptions, or (c) the line of sight to the continuum emission region misses the backflow region due to geometrical reasons (small r_{em} and $i \approx 0^\circ$). In the following we choose the parameters $r_{em} = 1$ AU and $i = 0^\circ$ for which also in the the adiabatic models no absorption from the backflow region will be present.

Moreover we calculate absorption line structures with the explicit exclusion of the jet head region. Also important to note is that we ignore the ionization problem discussed in section 4.2.3 assuming that all Ca-atoms are singly ionized Ca⁺. Further we choose a geometry which avoids the backflow region in the adiabatic models. Atomic parameters are taken for the Ca II absorption.

With these restrictions we obtain in the simulations absorption line profiles which are in quite good agreement with the observations. The simulations produce the detached, broad absorption component as observed for times where no new high velocity component was ejected during the previous days in the jet nozzle. This is shown in Figs. 4.13-4.15. There, sequences of the synthetical absorption line profiles are plotted for eight consecutive days for the adiabatic models i-iv and the model i with cooling.

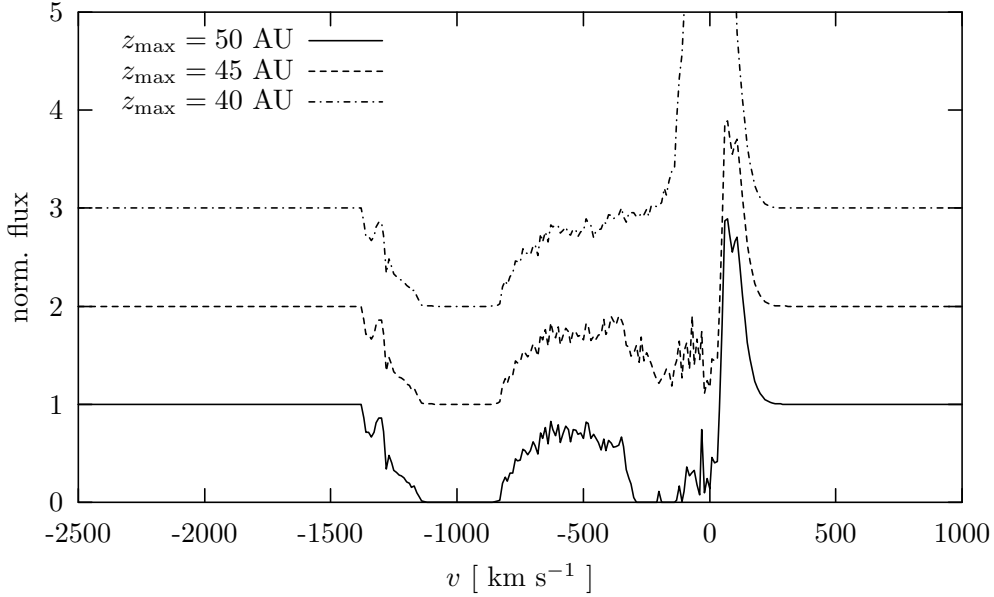


Figure 4.12: Theoretical absorption line profile of model i for values of z_{\max} ; the absorption feature at $RV \approx -300 \text{ km s}^{-1}$ is produced by the bow shock-Mach disk region

For days without high velocity component one can see that the widths of the absorption trough is smaller and the slope at its boundaries is steeper in the model with cooling than in the adiabatic models. This is a result of more pronounced inner structures in the cooled jet. Especially the steep slope at the blue side of the trough in the model with cooling is more similar to the observations.

The shallow component between the absorption trough and the emission line is visible in all models and always anticorrelated with the high velocity component as in the observations. Its strength also increases with increasing pulse densities.

4.4.2 Structure and evolution of the high velocity absorptions

Sect. 4.3 and Fig. 4.11 shows that the evolution of the highest velocity absorption components is in qualitative agreement with the observed behavior. However, there exists a most important difference between simulations and observations: the high velocity components are far too weak in the simulations compared with the observations.

In the adiabatic models the density in the jet pulse increases from $n_{\text{pulse}} = 1.25, 2.5, 5$ to $10 \times 10^6 \text{ cm}^{-3}$ for models i, ii, iii and iv respectively. Accordingly one can see a monotonic increase of the equivalent width and the depth of the high velocity components with increasing density of the pulses. According to the synthetic absorptions profiles, the higher density pulses required a longer time scale to be decelerated than the low density pulses. For example in Fig. 4.13, these components can be detected in only two consecutive days while they are present during three days in Fig. 4.14. A similar trend – a longer persistence and a higher depth of the high velocity components – can be found in the model with cooling with respect to the adiabatic model i.

Therefore a model with higher jet pulse density *including* cooling would be the model of choice.

4.5 Discussion II

In our previous study on the hydrodynamical structure of the investigated pulsed jets important differences were found between adiabatic simulations and the simulation including radiative cooling.

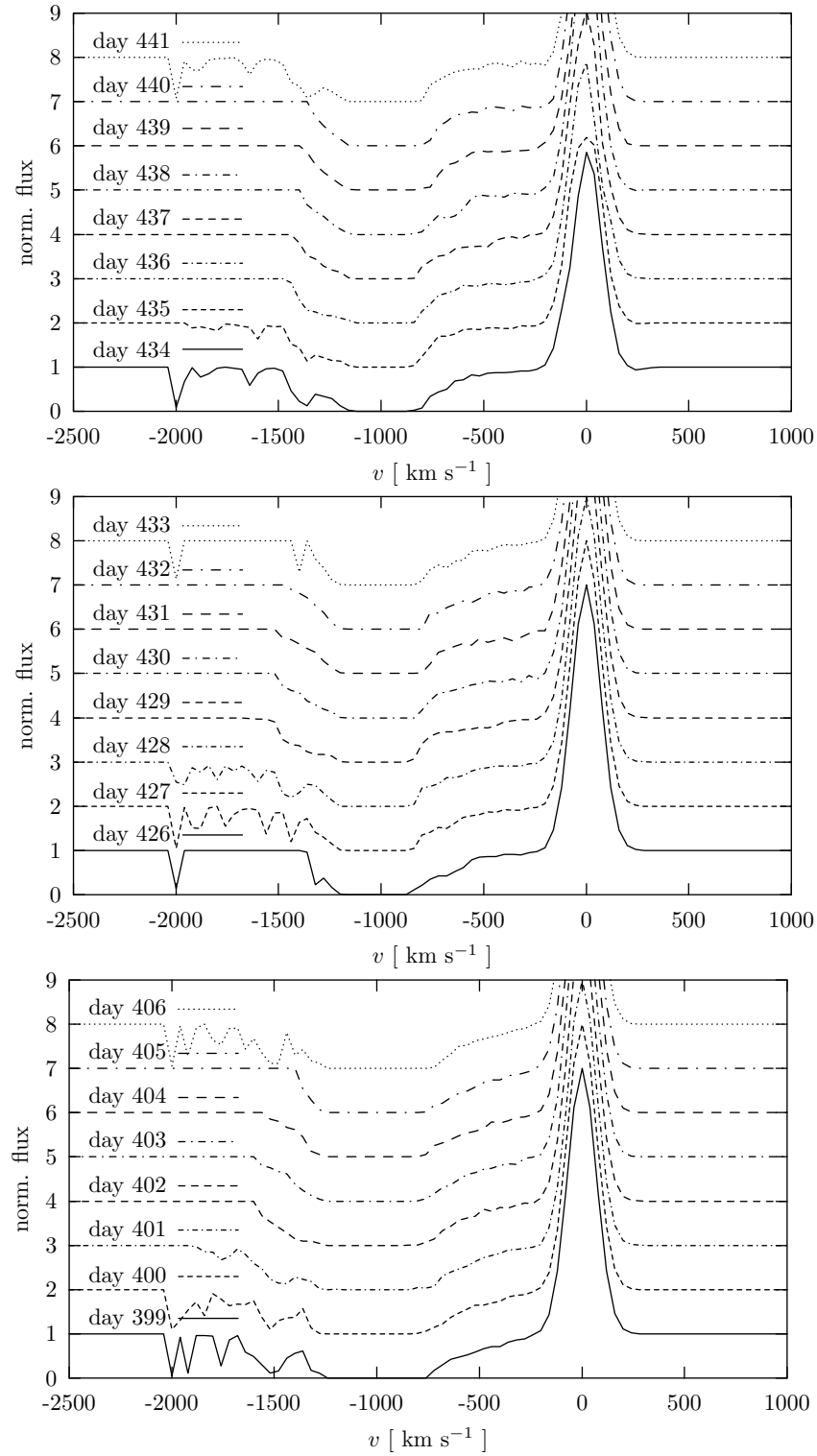


Figure 4.13: Sequence of absorption line profiles for eight consecutive days of model i (top), model ii (middle) and model iii (bottom)

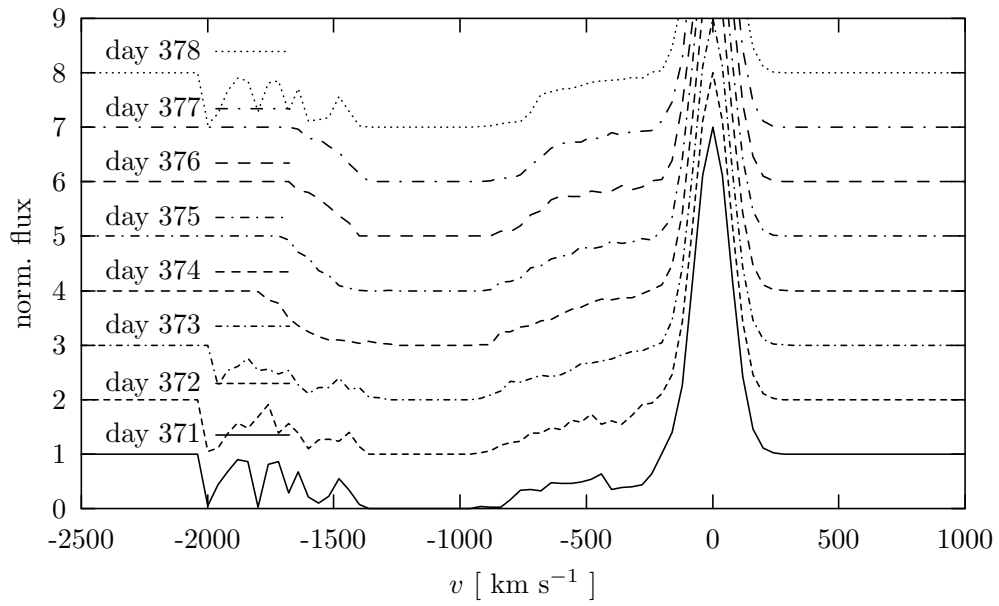


Figure 4.14: Sequence of absorption line profiles for eight consecutive days of model iv

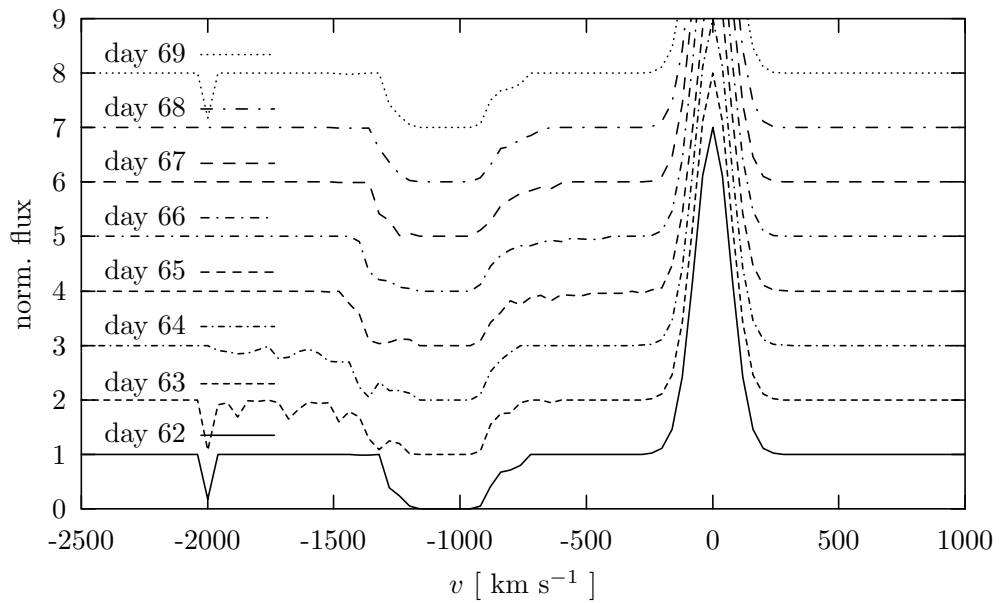


Figure 4.15: Sequence of absorption line profiles for eight consecutive days of model i with cooling

The adiabatic jets have an extended jet cocoon, while practically no cocoon is present for the jet model with cooling. Another difference is that the jet head velocity is much lower for the adiabatic jets. A further point, most important for the present study, is that the gas temperature in the adiabatic jet is everywhere far too high to produce the low ionization absorptions seen in the observations.

The gas temperature is also of central importance for the Ca II jet absorption profile calculated in this work. We find that for the adiabatic models practically no absorption is visible if the Ca ionization equilibrium is taken correctly into account. But even for the model simulations including radiative cooling the gas temperature in the jet is too high for producing the observed Ca II line strengths. Thus, more efficient cooling of the jet gas is required. This can be achieved with higher gas densities in the model jet outflow or perhaps with higher resolution of the hydrodynamical calculation, which may then be able to resolve high density small scale clumps. Additional modeling is required to investigate which of these solution is more likely.

Disregarding the ionization problem, we calculated the synthetic jet absorption line structure. This line structure represents essentially a projection of the gas radial velocity along the line of sight, which is more or less parallel to the jet. For the adiabatic jets with their extended cocoon and backflow regions different regions are probed depending on the adopted size of the emission line region or the inclination of the line of sight. For the well confined jet beam of the model with cooling, the calculated jet absorptions are essentially independent of these parameters.

The adiabatic model calculations show also a strong low velocity absorption between $-300 - 0 \text{ km s}^{-1}$ from the jet head region. This is not seen in the observations most likely because the real jet in MWC 560 extends much further into a low density environment than in our model simulation. Thus we can disregard this component as “artifact” of our model.

A success of our computations is that the basic structure of the jet absorption in MWC 560, which is the broad, detached component, can be well reproduced. The mean velocity and the velocity width is in good agreement with the observations. Surprisingly, both adiabatic jet models and the model with cooling provide qualitative similar absorption profiles. However, as we disregard the ionization equilibrium we should more correctly speak of the projected RV distribution of the gas.

Also the temporal evolution of the highest velocity components of the transient jet pulses follows the observed behavior. Not well reproduced by our simulations are the strengths of the high velocity components. They are far too weak in our simulations. This suggests that higher gas densities are required for the jet pulses.

From the presented comparison between the synthetic and observed jet absorption line structure we conclude that the general direction of our modeling is correct. Due to the high temperature the adiabatic simulations are inadequate to explain the observed low ionization absorptions observed. However, disregarding the temperature, they provide an easy to calculate mean to explore the projected velocity distribution of the gas in a pulsed jet along the line of sight. Our current jet simulation with radiative cooling solves the ionization problem not fully, as the gas temperature is still somewhat too high. However, the discrepancy is rather small and may be solved with calculations having a higher gas densities in the jet in order to enhance the efficiency of gas cooling. Higher gas densities are also required for the strengths of the absorption in the transient high velocity components.

With our comparison between synthetic and observed line profiles we have demonstrated the huge diagnostic potential of the spectroscopic observations of the jet absorption profiles in MWC 560. The information, which can be extracted from these observations, is unique for astrophysical jets and is therefore a most important source for a better understanding of astrophysical jets, in particular for the detailed investigation of the propagation and evolution of small scale structures originating in the jet acceleration region.

The shape of the high velocity components is in all simulations discrete. This could be a result of the assumed rectangular velocity and density steps for the pulses. A Gaussian form possibly could smooth the components in the absorption line profiles.

A point where these simulations can be further improved is the elapsed time and therefore the

calculated length of the resulting jet. We only simulated the jet until it reached a length of 50 AU. At this point, however, the density of the environment has decreased to the density in the jet nozzle. A transition of the initially underdense jet ($n_{\text{jet}}/n_{\text{wind}} < 1$) towards an overdense jet will occur, which should result in changed kinematics.

Chapter 5

Large scale simulations

We have now already performed purely hydrodynamical simulations and those including cooling of jets with parameters that are intended to represent those in MWC 560. We presented the structure and emission of the simulated jets and their implications on the absorption line profiles created by the jet. A drawback of our former simulations was the fact that they are stopped when the jet reached a length of 50 AU. At this point, however, the density of the environment has decreased to the density in the jet nozzle. A transition of the initially underdense jet towards an overdense jet should occur, which could result in changed kinematics. We present new large scale simulations with approximated cooling calculated on the NEC SX-5 and compare it with our former simulation including exact cooling effects.

5.1 The numerical models

To perform the large scale simulations with cooling, we were forced to approximate the treatment of cooling again. We neglected the atomic network with its rate equations and assumed collisional equilibrium to derive the ionization states of hydrogen. We included Bremsstrahlung and the general cooling function calculated with these partial densities. The pulse parameters were chosen as in the models i and iv. The nomenclature is now model i apc (approximated cooling) and iv apc, respectively.

As comparison a largescale simulation of the adiabatic model i was also performed neglecting all cooling effects.

The geometrical model was taken over without changes, except for the dimensions of the computational domain. In this new simulation, the dimension in axial direction was doubled to 100 AU to be able to study the jet propagation after density compensation.

5.2 Validating the cooling treatment

Before investigating the new simulations, we have to validate the ability of our approximated cooling treatment to describe the real properties inside jets of Symbiotic Stars. As we have already tested the reliability of our former simulation model i with cooling by observations, it is now sufficient to compare the simulation model i apc with that one. In Fig. 5.1 we show density and temperature plots from model i apc and model i with cooling at day 74, the last simulated time step in the old run. Apart from only slight differences in the internal structure such as in the shapes of vortices, the mean results as the bow shock sizes of the jets, positions of the internal shocks and density values are identical in both simulations. Therefore the previously derived properties such as the jet structure, the bow shock geometry and evolution, the internal jet structure and pulse evolution are consistent in both simulations. The same holds also for the temperature and therefore for the jet emission. This result seems to legitimate the use of an approximated treatment of the

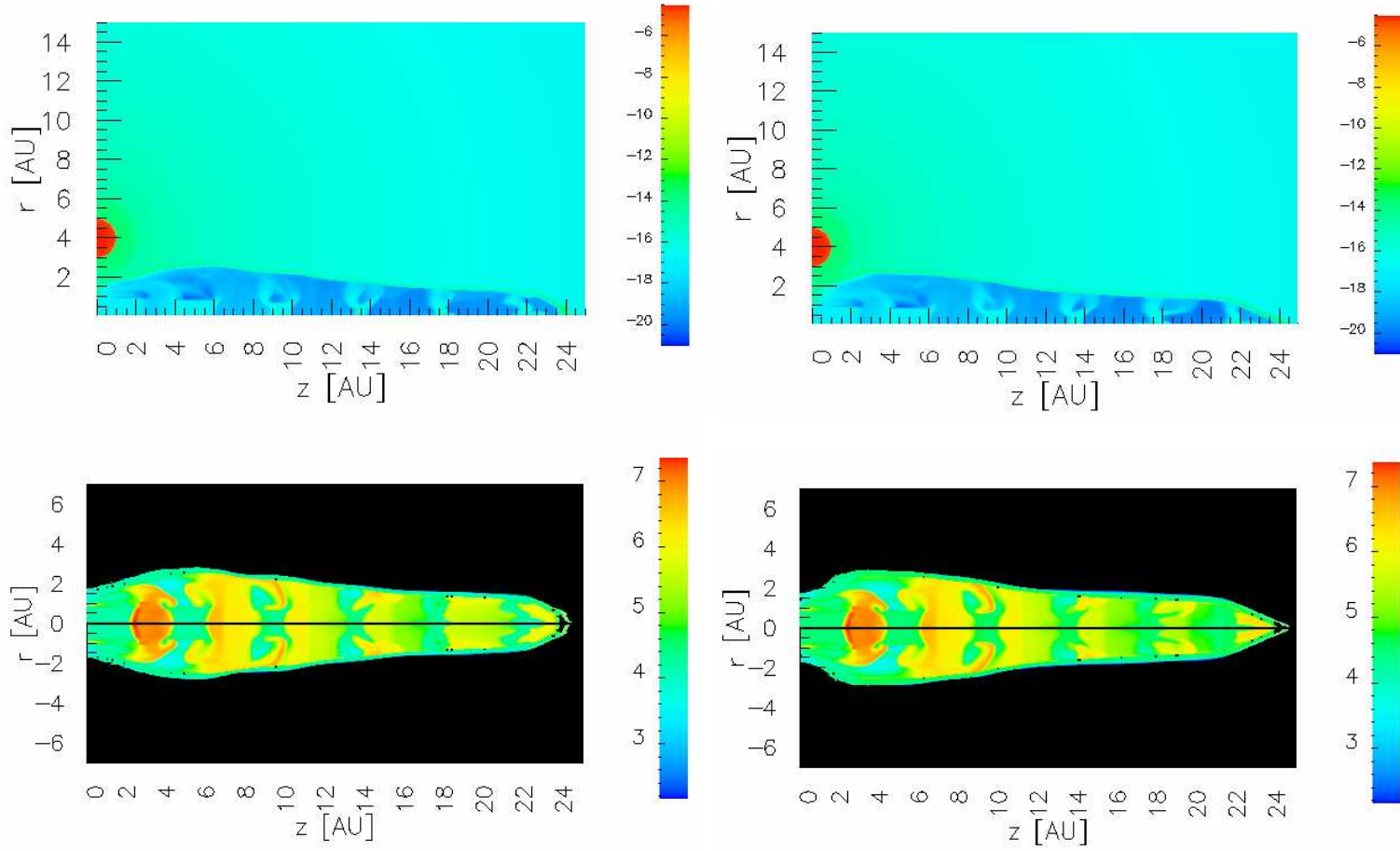


Figure 5.1: Comparison of density plots (top) and temperature plots (bottom) from model i with cooling (left) and model i apc (right) at day 74; beside slight differences in the internal morphology the dimensions of the jets, positions of the internal shocks, density values and temperatures are identical in both simulations

cooling inside jets in Symbiotic Stars and makes it possible to enlarge the numerical investigations with reduced computational constraints.

5.3 Jet structure

5.3.1 Bow shock geometry and evolution

The jet in the adiabatic model i shows no new behavior, it propagates in both directions with almost constant velocity. In radial direction, the velocity is now only $\sim 56 \text{ km s}^{-1}$ while 210 km s^{-1} in parallel direction. This last value is only the mean of variation on time scales of 100 days between 170 and 300 km s^{-1} .

The radial extension of the jet in model i apc, the cross section and the resistance exerted by the external medium are now only initially weakened. This leads again to a faster propagation velocity as in the adiabatic jet (Fig. 5.2). At the beginning, the cooled jet is always accelerating – in radial direction from 35 km s^{-1} in the first 70 days to 135 km s^{-1} in the following days. In parallel direction, it is accelerating from 485 km s^{-1} in the first 20 days to 740 km s^{-1} in the first 70 days. The radial extent – which was measured by searching the position of the density maximum – and therefore the jet head area only slightly increases and is not able to compensate the decreasing local density contrast as in the simulations without cooling. After day 70, however, suddenly the parallel velocity seems to remain constant. The radial extent and the jet head area grow, the acceleration stops. This is a new behavior which was not seen in the old simulation.

This transition is not caused by the density balance of the jet and its surrounding medium at a distance of 50 AU – the jet has propagated only 20 AU at day 70. A possible explanation could be a lack of numerical resolution. The size of the cocoon between the jet beam and the radial bow shock is initially too small to be resolved correctly. The sideways deposited shocked material from the pulses is then compressed and cools with high efficiency. Only a small fraction of the hot shocked gas cools by adiabatic expansion and inflates the cocoon. The more the cocoon grows, the more pressure waves can be sent into the cocoon and the more the growth of the cocoon is accelerated. With increased resolution, the cocoon and the radial extent of the jet should inflate from the very beginning, not be constant for a certain time.

Surprisingly, the density balance of the jet which should occur at 50 AU has no visible effect on the bow shock structure and evolution. This is possibly another result of the cooling which adjusts the density in the jet head in an also self-similar way.

In the model iv apc, the behavior of the parallel bow shock velocity is equivalent to that in model i apc, but the velocity after 70 days reached already 800 km s^{-1} . This higher acceleration is expected due to the higher density of the pulses. The radial velocity decreases to 45 km s^{-1} due to more efficient cooling and pressure loss inside this jet.

5.3.2 Internal jet structure

Fig. 5.3 shows the evolution of the internal shocks along the jet axis. As in model i with cooling, again the propagation of all pulses can be traced in the plot until their merger with the jet head. Each new pulse is instantaneously slowed down from 2000 km s^{-1} to about 1200 km s^{-1} within the first two days. The distance between the internal shocks created by the periodic velocity pulses stays constant. The very simple, periodic jet structure in the axial cuts of the Mach number, parallel velocity, density, pressure and temperature (Figs. 5.4-5.5) with knots and the jet beam remains in this large scale simulation unaffected by the above mentioned transition. A new feature in our model is the radial continuation of these knots into the cocoon (Fig. 5.6). They are not spatially confined to the jet beam.

No new effects can be detected in the model iv apc.

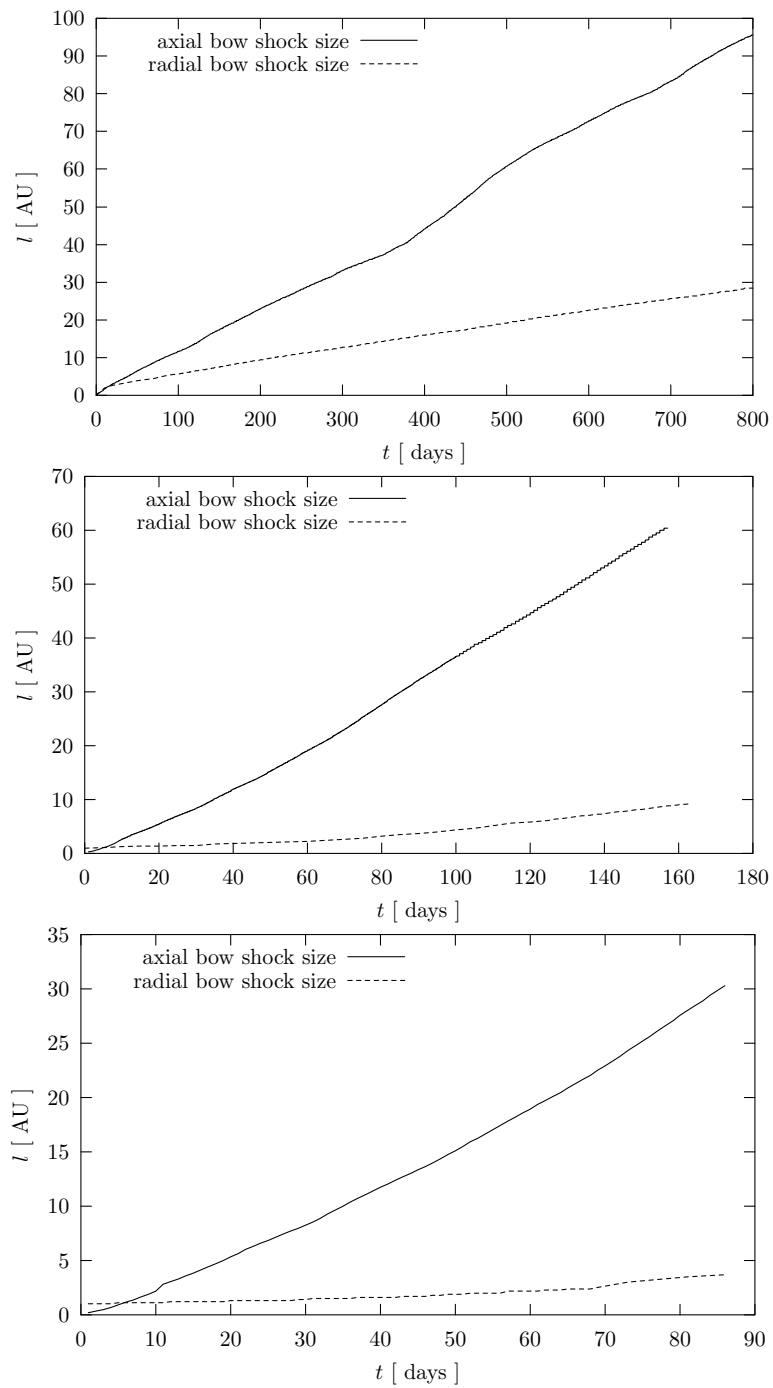


Figure 5.2: Size of the bow shock in parallel and radial direction for the adiabatic model i (top), model i apc (middle) and model iv apc (bottom)

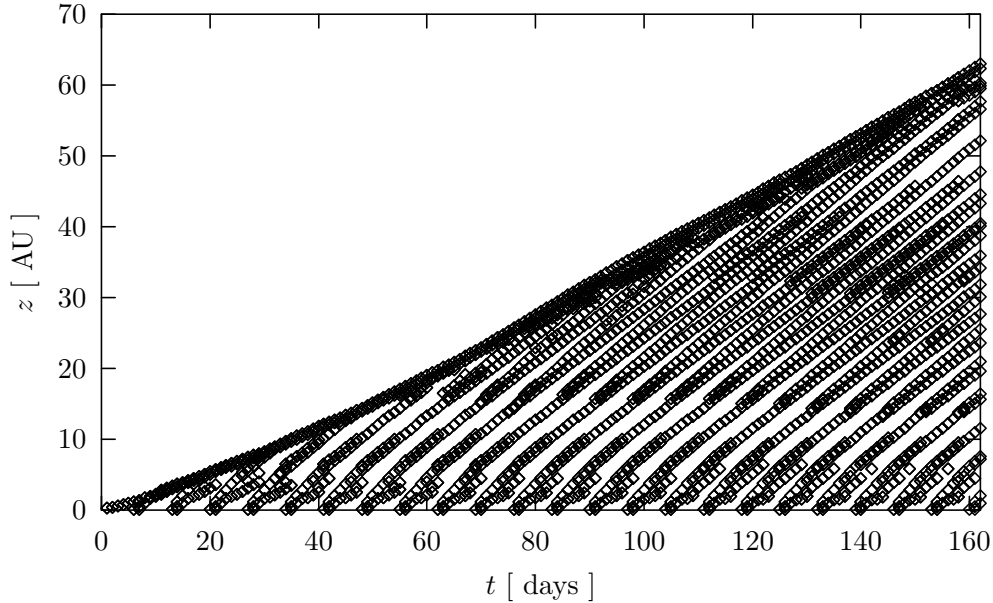


Figure 5.3: Evolution of the pulses for model i apc; all pulses can be traced directly until their merger with the jet head as in model i with cooling

5.3.3 Radial profiles

In Figs. 5.7-5.8 radial profiles are plotted for model i apc at day 162. The parallel velocity component again stays nearly constant inside the jet, but it slightly enhanced at radii of 5 AU compared to the jet axis. This leads to slow overtaking of the radial extensions of the jet pulses. The radial velocity component, however, shows now a different behavior with respect to the model i with cooling (Figs. 3.18-3.19). In the latter, negative velocities are present along the whole jet always at radii of 1 AU, now they are confined to the region on the jet axis near the jet head. This could be a sign of a collapse of the Mach disk-jet head region due to or after cooling.

The extensions of the jet pulses along the axis are visible in the density profile. While in model i with cooling, the knots had a radius of 1 AU, their extent is now a few AU. The density level in the knots, however, is lowered by a factor of ten. Therefore the total mass of each knot could be constant during this spreading process, which could be triggered by a trough in the pressure profile at an intermediate jet length.

5.4 Jet emission

Again the total emissivity due to bremsstrahlung of a completely ionized plasma and of HI line emission is calculated using the density and pressure data in each grid cell of the model i apc (Figs. 5.9-5.10).

In this plot, the knots with high density and lower temperature can be detected with their higher emission than the jet beam with low density and higher temperature. The distinctness of these structures in the cocoon increases downstream towards the jet head and makes them detectable in a better way. The fact that not only the knots in the jet beam are high emitters, but also the similar structures in the cocoon is in better agreement with observation as of R Aquarii which also show expanded emission knots which are too broad to be interpreted as structures in the jet beam alone.

Again, the results of model iv apc are similar.

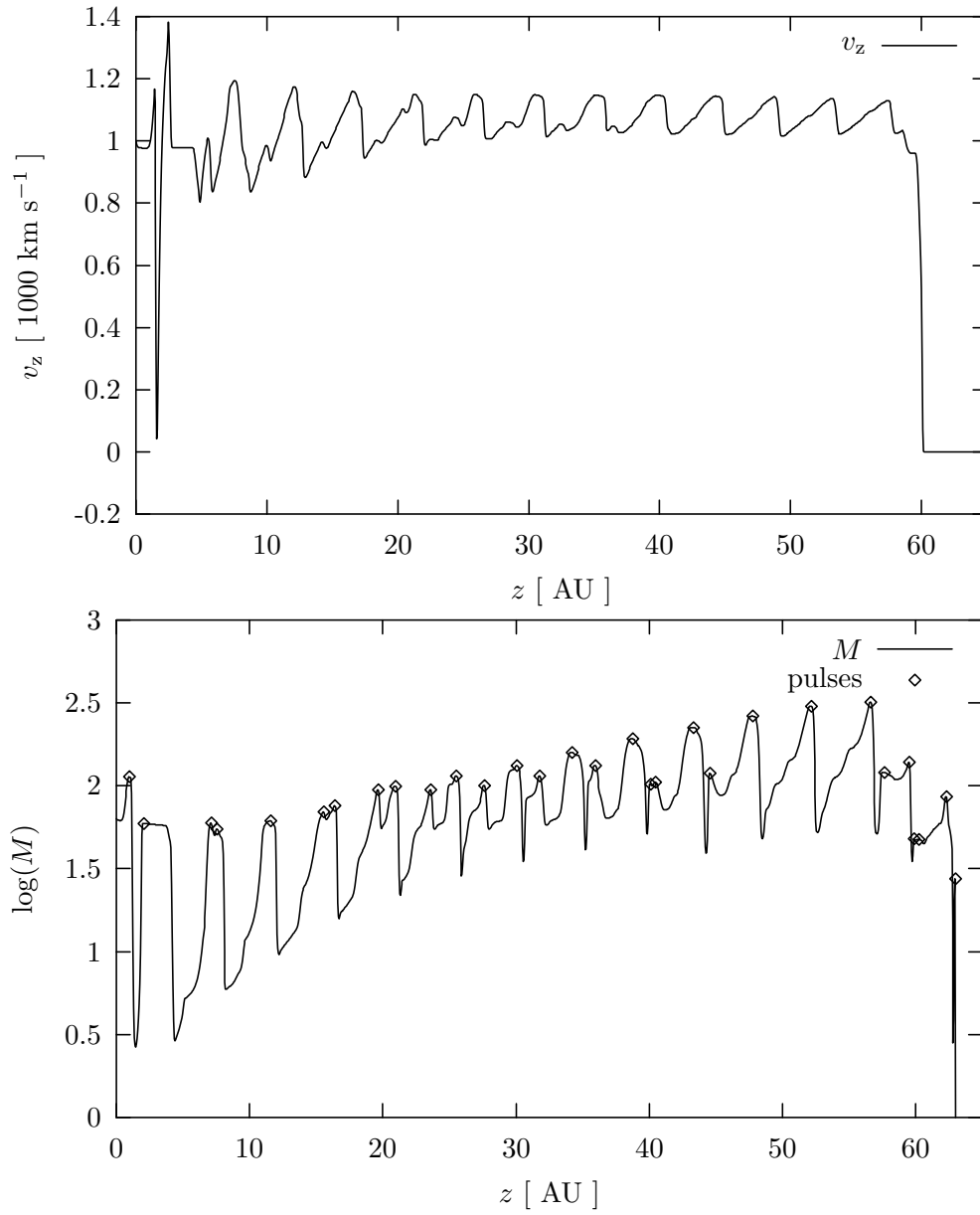


Figure 5.4: Slice of the parallel velocity and Mach number along the jet axis for model i apc; the internal shocks can be directly identified

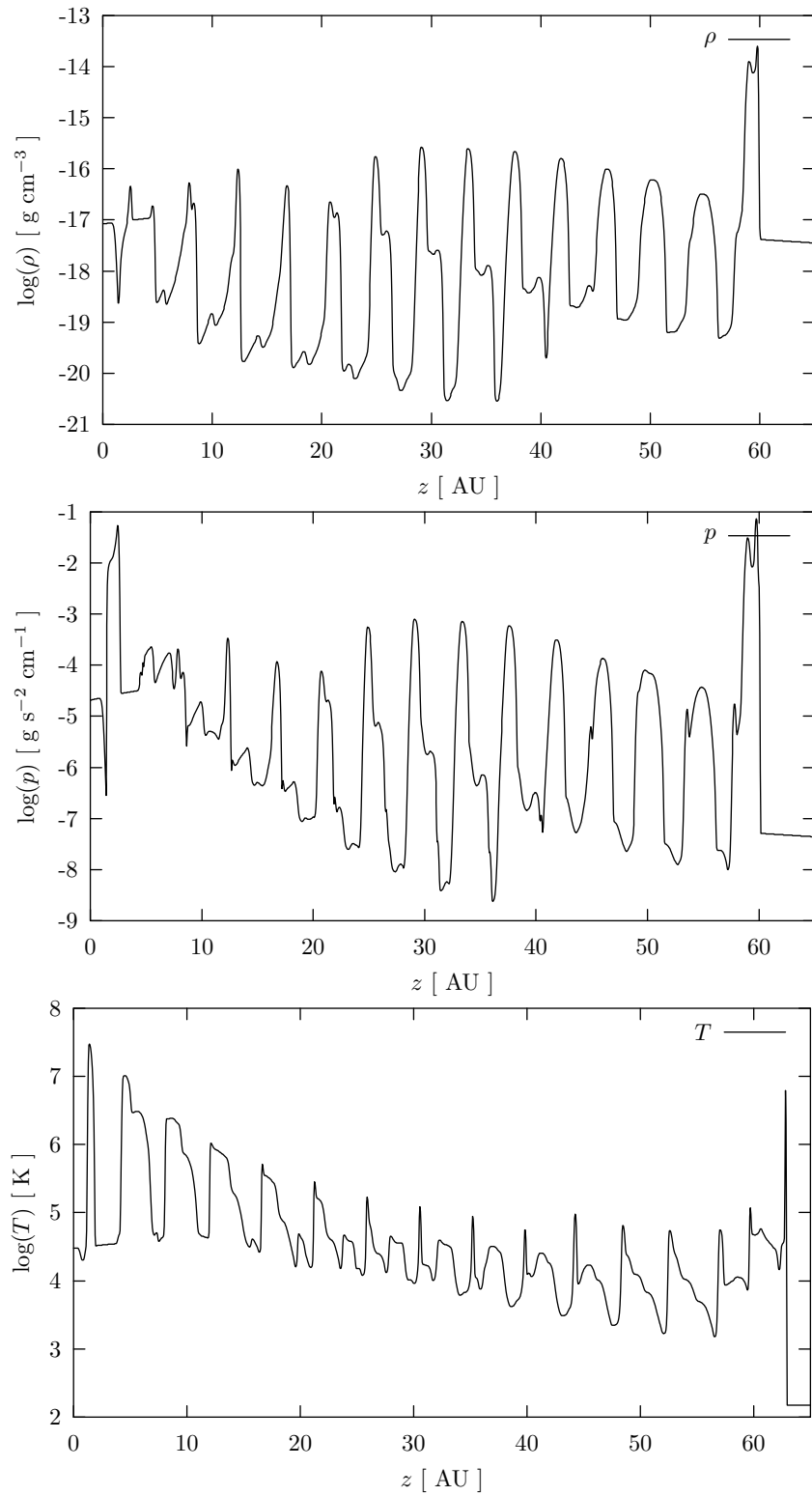


Figure 5.5: Slice of the logarithm of density, pressure and temperature along the jet axis for model i apc; the internal shocks can be directly identified

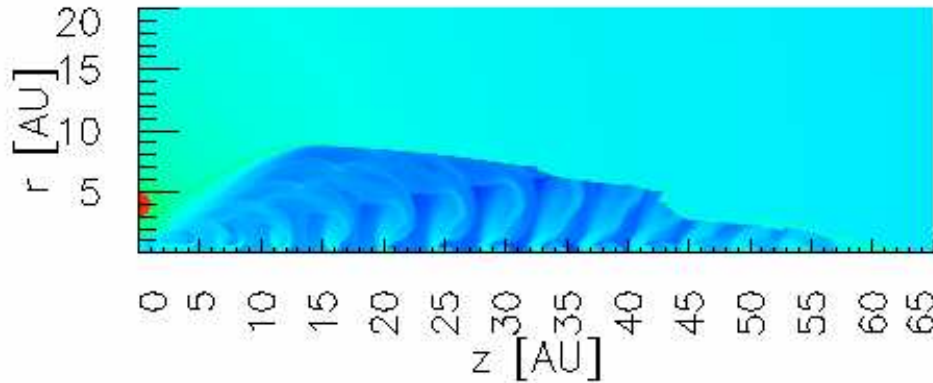


Figure 5.6: Logarithm of density of model i apc; the knots in the jet beam are extended into the cocoon

5.5 The absorption line profiles

In chapter 4, the weakness of the high velocity components in the synthetic absorption line profiles compared to the observed ones was described. Now, our model iv apc could be a solution of that problem, as both ways to increase the absorption in the high velocity component – higher pulse density plus cooling – are now present.

In Figs. 5.11-5.12, the sequences of the two largescale models i apc and iv apc are shown. In the first case, the extension of model i apc to larger propagation times and lengths results in no new effects. The position of the main absorption trough, the shape of its boundaries, the presence, persistence and depth of the high velocity component are unaffected with respect to Fig. 4.15.

The model iv apc with increased jet pulse densities, however, causes clearly visible differences. The stable absorption trough is shifted towards higher velocities, from -1050 km s^{-1} up to -1300 km s^{-1} and its width is increased from about 200 km s^{-1} to 500 km s^{-1} .

In the high velocity component, several deep absorptions are present in contrast to the few moderate ones in model i apc. In the observations of the Ca II line, however, the high velocity components are not saturated which seems to show that the real parameters are closer to model i apc than to model iv apc. In the Balmer lines saturation occurs often, but the level of the saturated line is enhanced by covering effects.

As the pulse structure was not changed the line widths of the high velocity components are again quite narrow. This could be perhaps improved by using a sinusoidal or Gaussian pulse profile instead of the rectangular steps in velocity and density.

5.6 Discussion III

Surprisingly, the assumed effect which was motivation for the presented large scale simulations due to the transition from an underdense to an overdense jet was not detectable, neither in the kinematics of the jet nor in its structure. Instead of that, however, a new effect which was not visible in the former simulation occurred in model i apc. The conclusion that the radial extent of the jet remains constant as seen also in the first days of the new simulation and the non-existence of a cocoon has to be replaced by an even inflating cocoon.

Caused by this inflation, the cocoon then shows a similar knotty structure as the jet beam which has similar emission properties. This new effect then improves the ability of the model to explain observations of jets in Symbiotic Stars with regard to their emission.

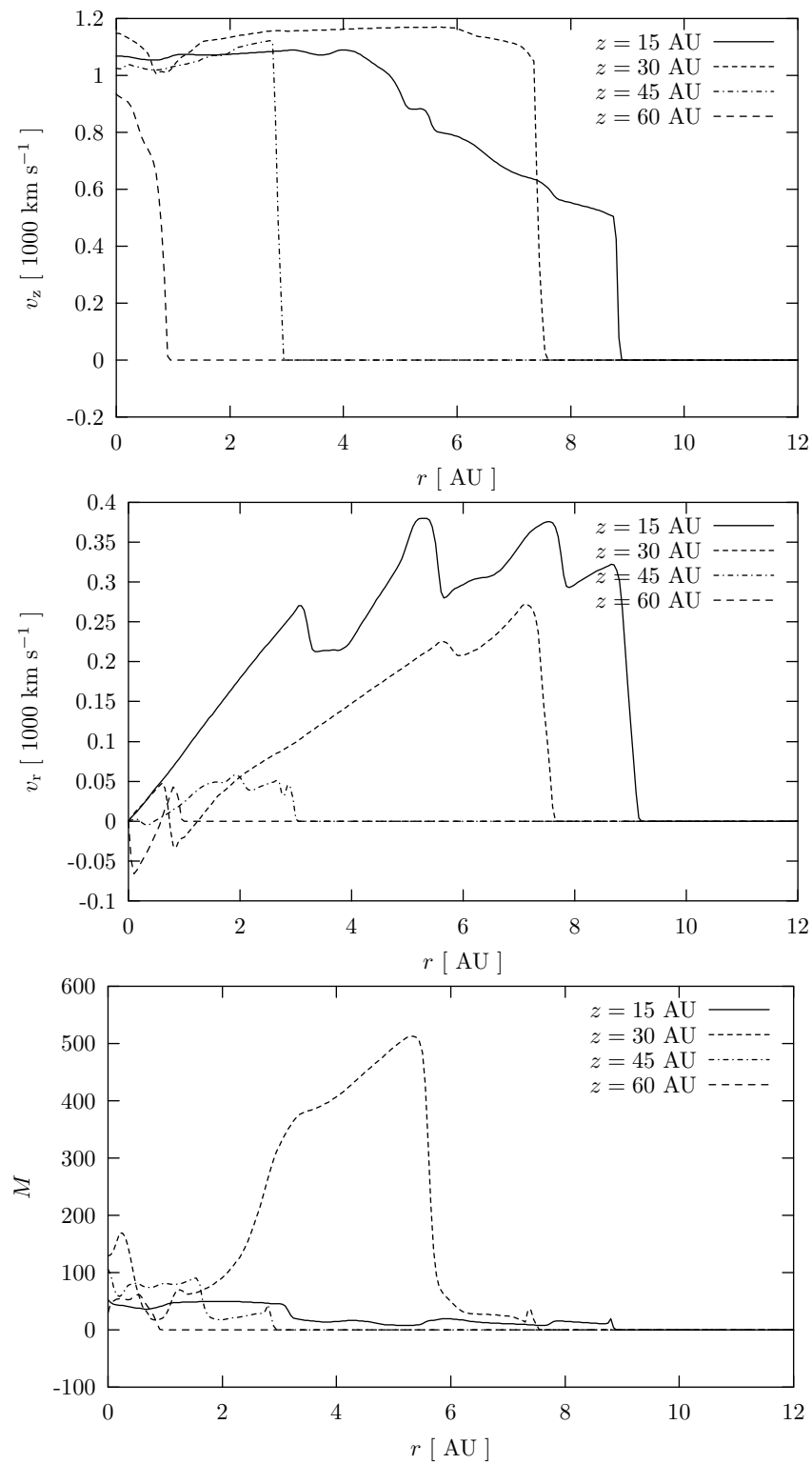


Figure 5.7: Radial profiles of the parallel and radial velocity and Mach number for model i apc

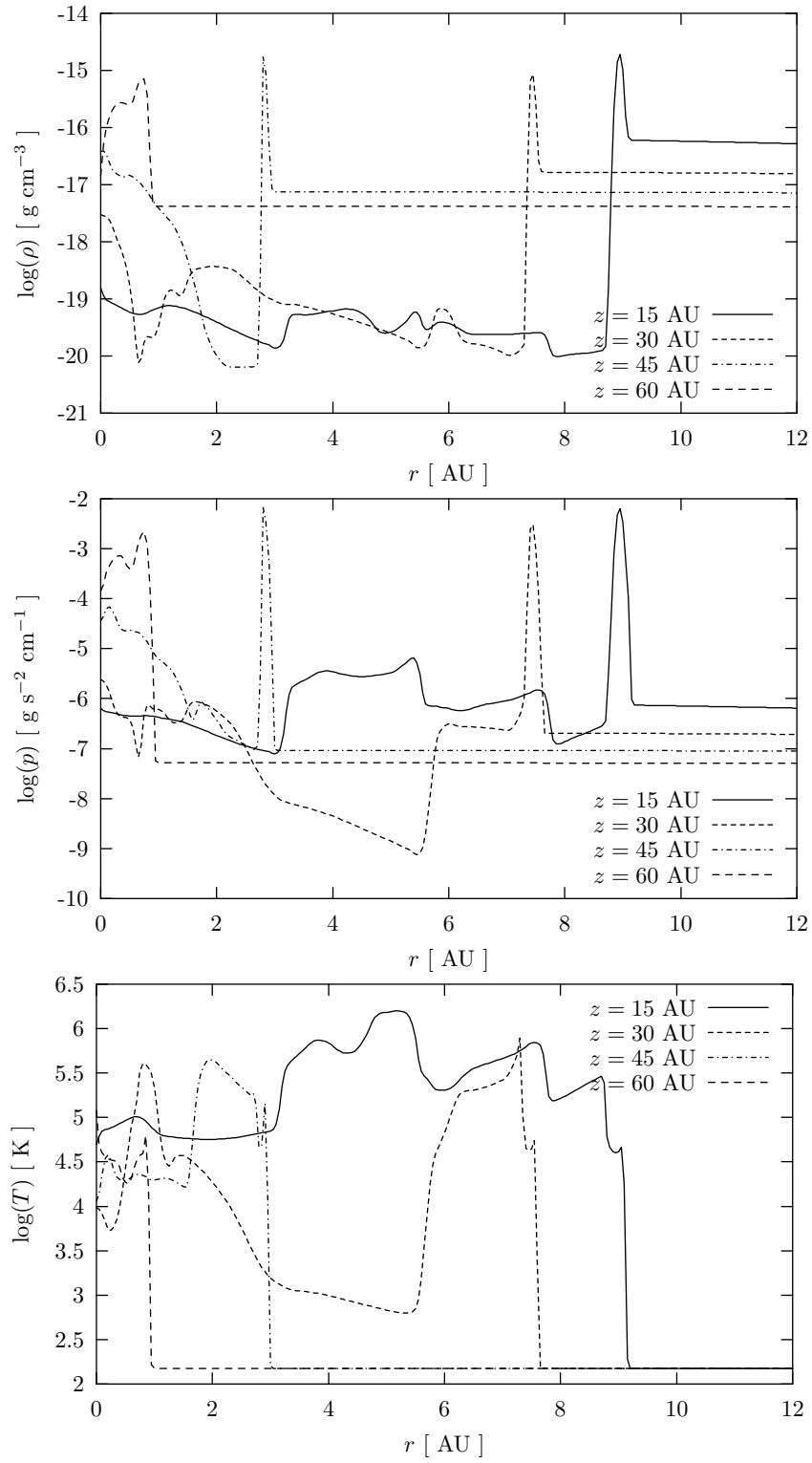


Figure 5.8: Radial profiles of the logarithm of density, pressure and temperature along the jet axis for model i apc

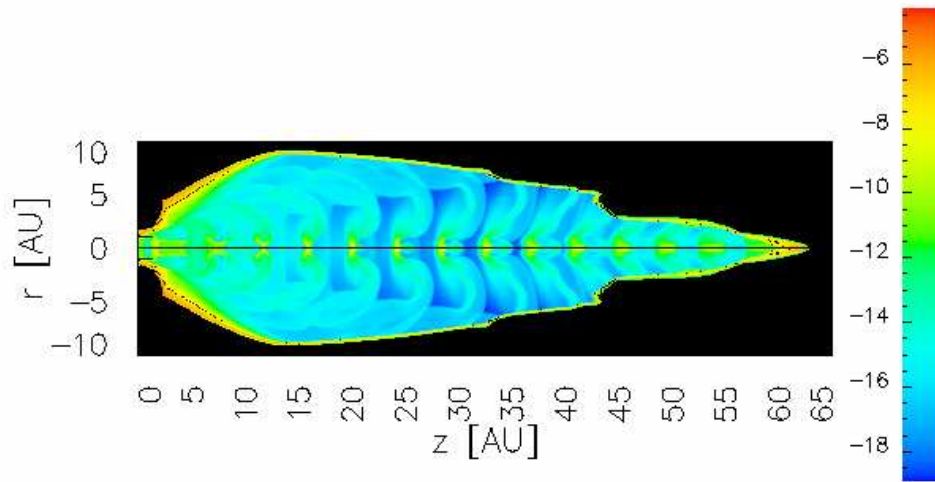


Figure 5.9: Logarithm of Bremsstrahlung emission for model i apc; knots with higher emission and the jet beam with lower are well distinguishable

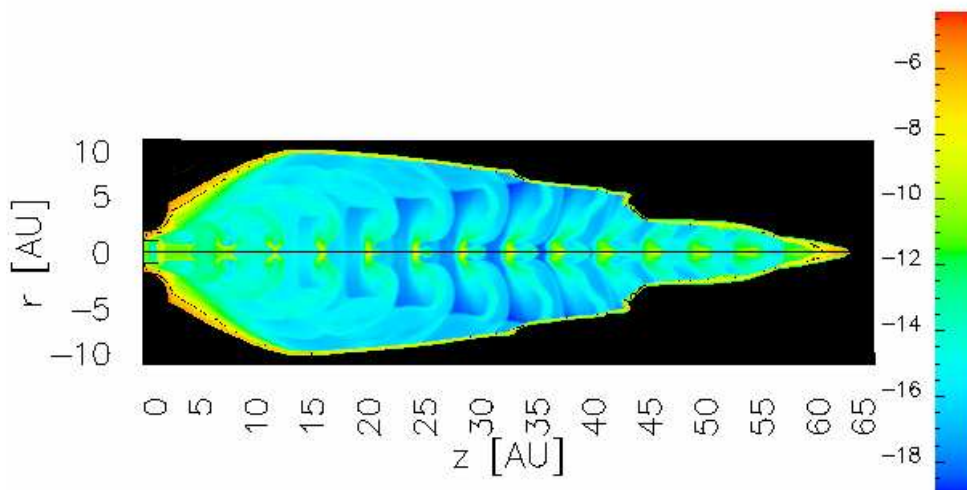


Figure 5.10: Logarithm of HI line emission for model i apc; no large deviation from Fig. 5.9 are present

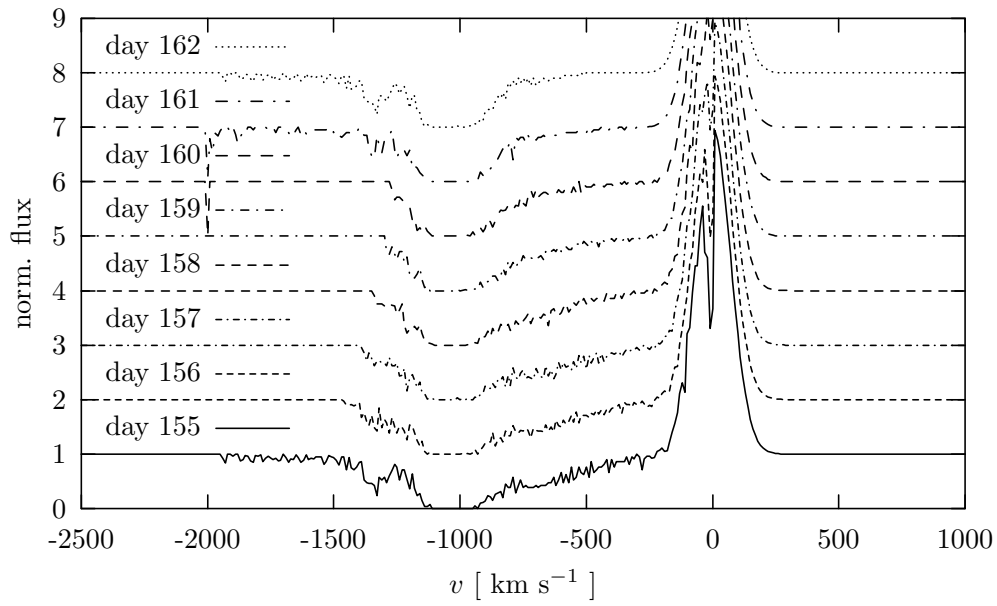


Figure 5.11: Sequence of absorption line profiles for eight consecutive days for model i apc

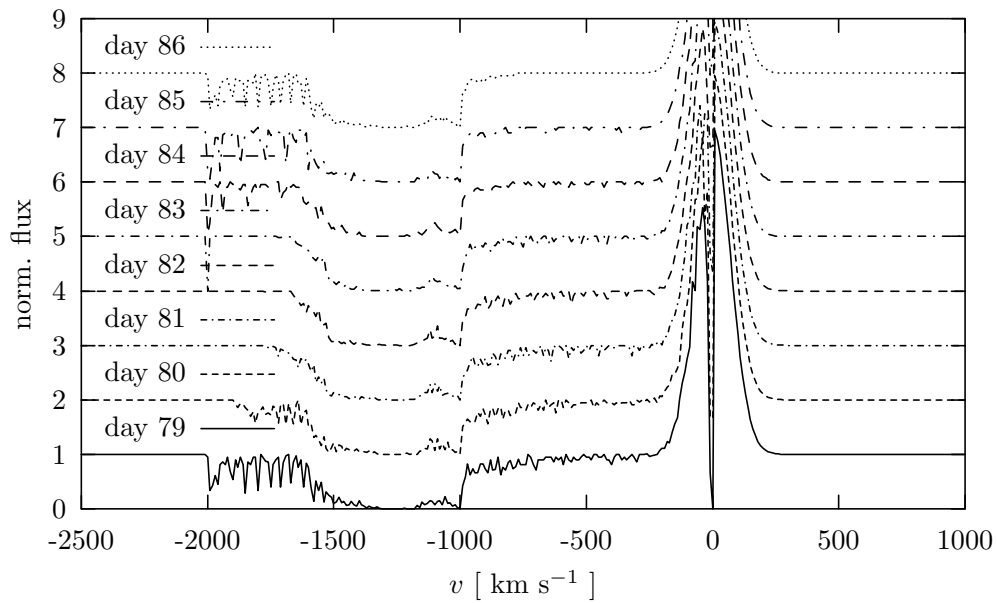


Figure 5.12: Sequence of absorption line profiles for eight consecutive days of model iv apc

The problem with too weak high velocity components in the absorption line profiles could be – almost overstatedly – solved in model iv apc. Another effect is the velocity shift of the stable absorption trough to higher velocities. The higher density leads to more efficient cooling and therefore the smaller radial extents of the jet and to faster propagation. This shift is, however, not appropriate to describe the observational data.

Chapter 6

Jet formation in white dwarf systems

In the previous part of this thesis, we focused ourselves on the propagation of jets in Symbiotic Stars. We assumed that the jet is already collimated when leaving the nozzle in our simulations. Now it is time to investigate in more detail the mechanisms of jet *formation* and *collimation* in Symbiotic Stars. In this chapter, we will present the technical approaches to solve the equations of magnetohydrodynamics and the jet formation scenarios found by these calculations.

6.1 Formation of jets by MHD processes

Jets are highly collimated and supersonic outflows. The opening angles are always only a few degrees. From emission lines, one can deduce temperatures of the order of 10^4 K which leads to sound speeds of 10 km s^{-1} . The typical jet velocities are at least one order of magnitude higher. Observations additionally show that the high collimation is already established at distances very close to the jet source. Jets should be therefore self-collimated. An elegant mechanism to accelerate and then collimate the jets by the same means, is to use magnetic fields as first shown in the pioneering work of Blandford & Payne (1982).

Radiation pressure as accelerating force is disproven by observations, as the measured luminosities and with it the radiation pressure thrust L_{bol}/c are by a factor of 100-1000 too small to explain the observed momentum discharge, kinetic energy of the jets and their outflow rate and velocity.

All systems which show jet emission seem to have accretion disks, e.g. detected by flickering. Simultaneous observations in different wavelength bands have shown that the UV emission thought to represent the thermal emission of the disk and the radio emission of the jets are always temporally correlated. Furthermore the observed outflow velocities are similar to the Keplerian velocity at the inner edge of the accretion disk. This seems to make a similar jet formation process in all known jet sources likely. The equations to be solved are those of Magnetohydrodynamics (MHD). These can be tackled in an analytic or numerical way.

6.1.1 Approaching the problem

To solve the basic equations of ideal MHD (without EOS/energy equation)

$$\frac{\partial}{\partial t} \rho + \nabla \cdot (\rho \mathbf{v}) = 0 \quad (6.1a)$$

$$\frac{\partial}{\partial t} (\rho \mathbf{v}) + \nabla \cdot (\rho \mathbf{v} \mathbf{v}) = -\nabla p - \rho \nabla \Phi + \left(\frac{1}{\mu_0} \nabla \times \mathbf{B} \right) \times \mathbf{B} \quad (6.1b)$$

$$\frac{\partial}{\partial t} \mathbf{B} = \nabla \times (\mathbf{v} \times \mathbf{B}) \quad (6.1c)$$

analytically, one starts with the first assumption: stationarity. This has the consequence that no feedback from the distant jet to the jet source is allowed. This then requires that the outflow has to be faster than any information carrying wave, i.e. the flow must go smoothly through all three critical points characterized by the three waves in MHD: the Alfvén waves defined as

$$v_A = \frac{B}{\sqrt{\mu_0 \rho}} \quad (6.2)$$

and the slow and fast magnetosonic waves calculated as

$$v_{\text{SM,FM}}^2 = \frac{1}{2} \left(v_A^2 + c_s^2 \mp \sqrt{(v_A^2 + c_s^2)^2 - 4 v_A^2 c_s^2 \cos^2 \theta} \right). \quad (6.3)$$

where θ is the angle between the magnetic field B and the direction of propagation of the wave. The second assumption is that of axisymmetry. Then the vector fields can be decomposed in cylindrical coordinates r, φ, z into

$$\begin{aligned} \mathbf{B} &= \mathbf{B}_p + B_\varphi \mathbf{e}_\varphi \\ \mathbf{v} &= \mathbf{v}_p + v_\varphi \mathbf{e}_\varphi = \mathbf{v}_p + \Omega r \mathbf{e}_\varphi. \end{aligned} \quad (6.4)$$

This assumption has direct consequences, from the first part of the induction equation (6.1c) follows directly

$$\mathbf{v}_p \times \mathbf{B}_p = 0, \quad (6.5)$$

which means that the poloidal component of the velocity is always parallel to the poloidal component of the magnetic field. With the continuity equation (6.1a), this can be written as

$$\mathbf{v}_p = \frac{\kappa}{\mu_0 \rho} \mathbf{B}_p \quad (6.6)$$

with

$$\kappa = \sqrt{\mu_0 \rho_A} \quad (6.7)$$

constant along a magnetic field line ($\mathbf{B}_p \cdot \nabla \kappa = 0$). ρ_A is the density at the Alfvén point. From the second part of the induction equation (6.1c) follows

$$\mathbf{B}_p = \frac{1}{r} \nabla \Psi(r, z) \times \mathbf{e}_\varphi = -\frac{1}{r} \frac{\partial \Psi}{\partial z} \mathbf{e}_r + \frac{1}{r} \frac{\partial \Psi}{\partial r} \mathbf{e}_z. \quad (6.8)$$

The poloidal magnetic field component can be expressed in terms of a function $\Psi(r, z)$, the magnetic flux function. The hydrodynamic flow is then confined along nested magnetic surfaces $\Psi = \text{const}$.

The other equations can be used to derive several integrals of motion. From the remaining information in the induction equation (6.1c) follows

$$B_\varphi \mathbf{v}_p = (\Omega - \Omega_F) r \mathbf{B}_p \quad (6.9)$$

which can be solved for

$$\Omega_F = \Omega - \frac{\kappa B_\varphi}{\mu_0 \rho r}. \quad (6.10)$$

This is the law of iso-rotation. The angular velocity of each magnetic surface is constant. From the φ -component of the momentum equation (6.1b) follows conservation of specific angular momentum

$$l = \Omega r^2 - \frac{r B_\varphi}{\kappa} = \text{const.} =: \Omega_F r_A^2. \quad (6.11)$$

With this equation, the Alfvén point r_A can be defined.

From the scalar product of the momentum equation (6.1b) with \mathbf{B}_p follows the conservation of specific energy

$$E = \frac{1}{2} \mathbf{v} \cdot \mathbf{v} + \Phi + h - \frac{r \Omega_F B_\varphi}{\kappa}. \quad (6.12)$$

In this sometimes called Bernoulli equation, h is the enthalpy with $\nabla h = \frac{1}{\rho} \nabla p$ in adiabatic case and $h = \frac{\gamma}{\gamma-1} \frac{p}{\rho}$ for polytropes. Another invariant K is needed in the energy equation omitted so far, which is then related to a conservation of specific entropy.

To solve now the problem of jet formation, one last step is to find the shape of Ψ . For this, one has to consider the force balance in normal direction which gives the Grad-Shafranov equation

$$\frac{\rho_A - \rho}{\rho} r^2 \nabla \left(\frac{1}{r^2} \nabla \Psi \right) + \frac{1}{2} \rho \nabla \Psi \cdot \nabla \left(\frac{\rho_A}{\rho^2} \right) = 4\pi \rho r^2 \left[\frac{d\mathcal{E}}{d\Psi} + g \Omega_F \left(\frac{d(\Omega_F r_A^2)}{d\Psi} + g \Omega_F r^2 \frac{\rho}{2\rho_A} \frac{d \ln \rho_A}{d\Psi} \right) + \Omega r^2 \frac{d\Omega_F}{d\Psi} \right] \quad (6.13)$$

with the combined constant of motion $\mathcal{E} = E - \Omega_F^2 r_A^2$. Solving this highly non-linear equation is still a challenge!

We then have 8 unknown variables (density ρ , 3 velocity components \mathbf{v} , 2 magnetic field variables Ψ , B_φ , pressure p , temperature T), 8 equations (eq. for \mathbf{B}_p , perfect gas law, EOS, eq. for \mathbf{v}_p , eq. for Ω_F , eq. for l , Bernoulli and Grad-Shafranov equation) and 5 MHD invariants (ratio of ejected mass to magnetic flux κ , rotation rate of magnetic surface Ω_F , total specific angular momentum l , total specific energy E , invariant related to specific entropy K) plus 3 regularity conditions to overcome the singularities of the MHD equations (6.1) at the three critical points. These equations can now be solved analytically in the self-similar case with its geometrical constraints (e.g. Pudritz & Norman 1986; Ferreira & Casse 2004) or numerically in the non-self-similar case (e.g. Camenzind 1990; Pelletier & Pudritz 1992; Breitmoser & Camenzind 2000).

This above-mentioned way to solve the problem is now somewhat outdated, although a lot of work is still done in this area. Unfortunately, the perhaps most important variable – the time t – is not considered in these analytic studies. Observations, however, show that the process of jet formation is highly transient and time-dependant. The other approach then which will also be used throughout this thesis is to solve the full set of time-dependant MHD equations (A.5) numerically without any assumptions concerning symmetry or stationarity. In the first simulations, a polytropic accretion disk in hydrostatic equilibrium was set as boundary condition (e.g. Ustyugova et al. 1999; Krasnopolsky, Li & Blandford 1999, 2003). Remarkably, in these simulations stationary flows can occur which are consistent with analytic stationary MHD theory. One disadvantage of them, however, is the fact that the magnetic feedback onto the disk structure was not considered self-consistently. Recently, new numerical studies overcame this drawback (Casse & Keppens 2002, 2004; Kato, Mineshige & Shibata 2004).

6.1.2 Jet formation scenarios

Depending on the internal magnetic field structure, all models can be sorted into three jet formation scenarios.

The disk-wind scenario assumes an open large scale magnetic field. B_z is then an even function of z , so B_r and B_φ have to have odd symmetry, if the field is assumed to be axisymmetric. One direct consequence is that the radial and azimuthal field component have to vanish in the disk plane ($B_r|_{z=0} = B_\varphi|_{z=0} = 0$). As already Blandford & Payne (1982) have shown, the angle θ

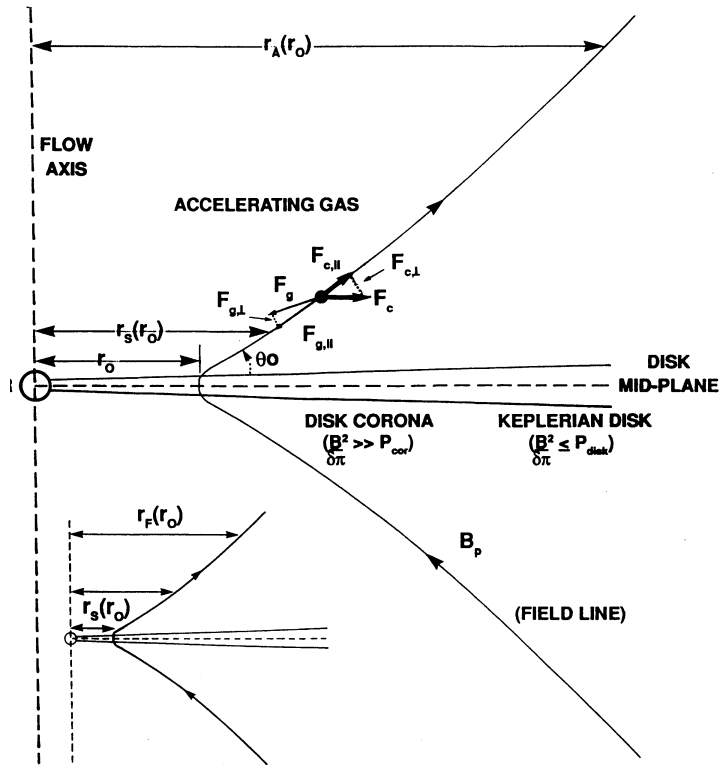


Figure 6.1: Schematic sketch of the accretion disk and the magnetic field; also shown are the acting forces and the position of the critical points; adopted from Pelletier & Pudritz (1992)

between the field line and the disk surface has to be smaller than 60° to achieve acceleration of disk material. The magnetic field lines are like rigid wires controlling the flow like beads. Forces, acting on a gas parcel, are gravity (of the central star) F_g and centrifugal forces due to Keplerian rotation F_c (Fig. 6.1). After the slow-magnetosonic point the gas will be centrifugally accelerated into a jet/wind, the flow accelerates as far as the Alfvén point. After this point the acceleration continues, only if the density continues to decrease. At the fast-magnetosonic point the acceleration stops and collimation starts by the toroidal component of the magnetic field. The decomposition of the acting forces shows that effective gravity can vanish far enough along the field line.

One problem of this scenario is the origin of the external field. Two mechanisms to create this large scale field are possible – or a mixture of both: advection of an interstellar field during the infall of matter or a disk dynamo (Ferreira 2004).

The second scenario assumes a more natural magnetic field configuration: a dipolar stellar field connecting the star with the disk (Fig. 6.2). By the differential rotation of the disk, the magnetic loops connecting the star and the disk become twisted which induces a toroidal field component. This induction increases magnetic pressure which causes the loops to expand. The system then evolves through a series of force-free configurations with increasing energy towards a non-equilibrium state; the expansion accelerates plasma which is attached to field lines. Last, magnetic reconnection frees the plasmoid from the system and increases the stellar magnetosphere

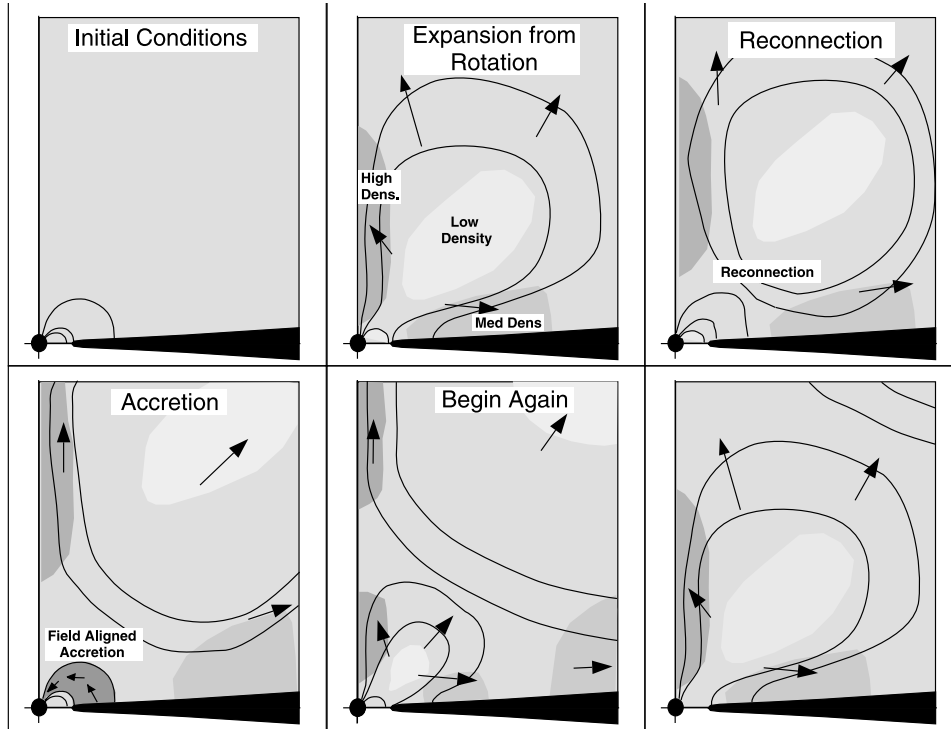


Figure 6.2: Schematic sketch of jet formation mechanism through star-disk-interaction; adopted from Goodson, Böhm & Winglee (1999)

whose parts within the corotation radius trigger field-aligned accretion. Parts of the newly enlarged magnetosphere connect the star and its disk again and another expansion will be initiated by the differential rotation, but now plasma from the accretion stream flows out. This ejection cycle leads also to an oscillation of the inner accretion disk. The expansion of the magnetosphere truncates the disk, the outer boundary of the magnetosphere diffuses into the disk, the disk spirals inwards, until it causes reconnection and after reloading by accretion flow, there is again expansion of the magnetosphere. The value of the diffusivity distinguishes between several modes of ejection: for high diffusivity ($v_K < v_{diff}$) the field can continuously slip through the disk and cannot be constantly wrapped up, for intermediate diffusivity ($v_r < v_{diff} < v_K$) the field can be wrapped up until it opens, steady solutions are possible if the diffusion velocity is greater than the peak radial velocity of the inner disk, and for low diffusivity ($v_{diff} < v_r$) the oscillation mechanism applies leading to episodic outflows (Goodson, Böhm & Winglee 1999).

The third scenario works without the assumption of an external magnetic field. Only small scale magnetic fields of a purely poloidal configuration inside the often used initial condition of a rotating torus is needed to start accretion by the magneto-rotational instability (*MRI*, Balbus & Hawley 1991). No large scale magnetic field is necessary outside the torus. When disk material reaches the innermost region, upward motion is triggered by the magnetic pressure of the accumulated toroidal fields, sometimes called “magnetic tower”. At some point, the magnetic tower stops vertical inflation and turns to shrink because of the pressure in the corona, part of blown up material falls back towards the equatorial plane. When a geometric thick structure persists, a quasi-steady state is set up (Kato, Mineshige & Shibata 2004).

6.2 Formation of jets by thermal pressure in *SPLASHs*

Recently, Soker & Regev (2003) pointed out a problem which arises in their opinion from X-ray observations of YSOs. They claim that, if the magnetic energy plays an important role over large regions, strong magnetic fields should undergo resistive reconnection. This then should produce X-rays. Getman et al. (2002), however, have found in a X-ray study with Chandra, that no correlation is present between the presence or absence of outflows and the X-ray luminosities.

Motivated by this *X-ray deficit*, Soker & Regev (2003) proposed a new ejection mechanism and allow only for small magnetic fields to collimate the flow. They suggest that the acceleration is driven by thermal pressure in boundary layers (BL), the region in which the accreting matter is decelerated from its Keplerian rotation to the much smaller stellar rotation and which is likely in weakly magnetized Neutron Stars and White Dwarfs. It is a relatively small, but hot region which is optically thick at high and optically thin at low accretion rates. The rotational support against gravity is replaced by thermal pressure. Up to one half of the gain in potential energy is radiated in this small region – the other half has been already lost in the accretion disk. They assume the formation of spatiotemporally localized accretion shocks (*SPLASHs*), i.e. a small amount of accreted matter is shocked within a short dissipation event. Here, their analytic estimates will be introduced.

Let the BL be geometrically thin and isothermal in vertical direction ($P = c_s^2 \rho$), then the hydrostatic equation is

$$\frac{1}{\rho} \frac{dP}{dz} = -\frac{z}{r^2} v_K^2 \quad \implies \quad \rho = \rho_0 \exp\left(-\frac{z}{r^2} \frac{v_K^2}{c_s^2}\right). \quad (6.14)$$

Let the radial extension of the BL $b = \epsilon R \simeq H$ be similar to the disk height at the BL. The necessary condition for formation of *SPLASHs* is

$$T_{\text{cool}} = \frac{l^2 \kappa \rho}{c_s} \gtrsim T_{\text{ad}} = \frac{l}{c_s}. \quad (6.15)$$

If one assumes an isothermal disk before AND after occurrence of *SPLASHs*, this leads to a vertical acceleration

$$a_z = -\frac{1}{\rho} \frac{dP}{dz} - \frac{z}{r^2} v_K^2 = \frac{z}{r^2} v_K^2 (\eta - 1) \quad (6.16)$$

with the temperature rise η . If the shocked material in the *SPLASH* expands to a distance z , it reaches the velocity

$$v_z = \beta \sqrt{2z a_z} = \frac{z}{r} v_{\text{esc}} \sqrt{\eta - 1} \beta \quad (6.17)$$

with the parameter β independent of z and the escape velocity $v_{\text{esc}} = \sqrt{2} v_K$. The kinetic energy of the rotating disk material is transformed to thermal energy in the *SPLASH* and back to kinetic energy via expansion. To allow for radiative losses of energy, one can introduce another parameter Γ as the fraction of initial kinetic energy converted into kinetic energy of escape. $1 - \Gamma$ is then the radiative loss.

The initial Keplerian kinetic energy per unit fraction of the disk is

$$E_{\text{kin, in}} = \frac{1}{2} v_K^2 \int_{-\infty}^{\infty} \rho dz \quad (6.18)$$

and that of the escaping material is

$$E_{\text{kin, fin}} = \frac{1}{2} \int_{-\infty}^{\infty} v_z^2 \rho dz. \quad (6.19)$$

With the definition of $\Gamma = E_{\text{kin, fin}}/E_{\text{kin, in}}$ and equations (6.14) and (6.17), this can be expressed as

$$\beta \sqrt{\eta - 1} = \sqrt{\Gamma} \frac{v_K}{\sqrt{2} c_s}. \quad (6.20)$$

After substituting back in equation (6.17), we get

$$v_z = \frac{z}{r} v_{\text{esc}} \sqrt{\Gamma} \frac{v_K}{\sqrt{2} c_s}. \quad (6.21)$$

To achieve jet launching, we have the condition $v_z \gtrsim v_{\text{esc}}$ which is equal to

$$x := \frac{z}{r} \frac{v_K}{\sqrt{2} c_s} \gtrsim \frac{1}{\sqrt{\Gamma}}. \quad (6.22)$$

The mass per unit area which reaches the escape velocity is

$$\Sigma_{\text{esc}} = 2 \int_{z_m}^{\infty} \rho dz \quad (6.23)$$

with z_m the height at which $v_z = v_{\text{esc}}$. The fraction of disc material reaching escape velocity follows to

$$f_m = \frac{\int_0^{\infty} e^{-x^2} dx}{\int_0^{\infty} e^{-x^2} dx} \quad (6.24)$$

and fraction of total energy carried by escaping mass to

$$f_E = \Gamma \frac{\int_0^{\infty} x^2 e^{-x^2} dx}{\int_0^{\infty} x^2 e^{-x^2} dx}. \quad (6.25)$$

The momentum per unit mass carried by the wind is

$$v_a = \sqrt{\Gamma} v_{\text{esc}} \frac{\int_0^{\infty} x e^{-x^2} dx}{\int_0^{\infty} e^{-x^2} dx} \frac{1/\sqrt{\Gamma}}{1/\sqrt{\Gamma}}. \quad (6.26)$$

We have now $f_m = f_m(\Gamma)$, $f_E = f_E(\Gamma)$ and $v_a = v_a(\Gamma)$ (Fig. 6.3), which can be observed in principle. After introducing the ‘‘mass processing’’ efficiency $0 < \chi = \dot{M}_{\text{splash}}/\dot{M}_{\text{acc}} < 1$, this leads to the real observables mass loss, kinetic luminosity and momentum discharge

$$\dot{M}_o = \chi f_m \dot{M}_{\text{acc}} \quad (6.27)$$

$$L_{\text{kin}} = 0.5 \chi f_E \frac{G M \dot{M}_{\text{acc}}}{R} \quad (6.28)$$

$$\dot{P}_o = \chi f_m \dot{M}_{\text{acc}} v_a. \quad (6.29)$$

These three values should be consistent with the same choice of Γ and χ .

6.3 Estimates and reliability

As already presented in section 2.5 and as used to simulate the jet nozzle, the parameters of the jet in MWC 560 are

- the velocity $v = 1000 \text{ km s}^{-1}$ and

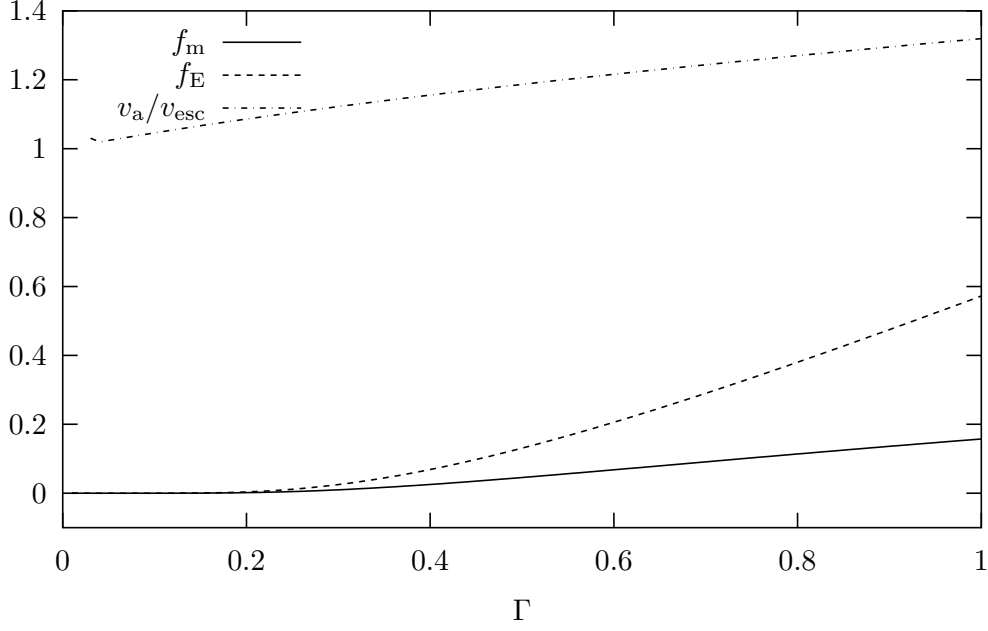


Figure 6.3: $f_m = f_m(\Gamma)$, $f_E = f_E(\Gamma)$ and $v_a/v_{\text{esc}} = v_a/v_{\text{esc}}(\Gamma)$

- the number density $n = 5 \times 10^6 \text{ cm}^{-3}$, which is equal to a mass density $\rho = 8.4 \times 10^{-18} \text{ g cm}^{-3}$.

Using equations 3.1 , this specifies

- the mass outflow rate $\dot{M}_{\text{jet}} = 9.33 \times 10^{-9} M_{\odot} \text{ yr}^{-1}$,
- the momentum discharge $\dot{P}_0 = \dot{M}_{\text{jet}} v_{\text{jet}} = 5.93 \times 10^{25} \text{ g cm}^{-1} \text{ s}^{-2}$ and
- the kinetic jet luminosity $L_{\text{jet}} = 2.93 \times 10^{33} \text{ erg s}^{-1}$.

The occurrence of the pulses is tentatively neglected. This energy output can be provided by several different mechanisms:

- by the luminosity of the white dwarfs

$$L_{\text{WD}} = 4 \pi R_*^2 \sigma T^4 = 3.5 \times 10^{30} \left(\frac{R_*}{7 \times 10^8 \text{ cm}} \right)^2 \left(\frac{T}{10^4 \text{ K}} \right)^4 \text{ erg s}^{-1} \quad (6.30)$$

- the accretion power of the disk (and almost the same amount coming from a BL)

$$L_{\text{acc}} = \frac{1}{2} \frac{G M_* \dot{M}}{R_*} = 1.1 \times 10^{35} \left(\frac{R_*}{7 \times 10^8 \text{ cm}} \right)^{-1} \left(\frac{M_*}{M_{\odot}} \right) \left(\frac{\dot{M}}{10^{-8} M_{\odot} \text{ yr}^{-1}} \right) \text{ erg s}^{-1} \quad (6.31)$$

- or the magnetic luminosity (Camenzind 1997)

$$L_{\text{mag}} = \frac{1}{2} \Omega_* R_*^3 B_p B_{\varphi} = 6.17 \times 10^{32} \left(\frac{\Omega_*}{\text{h}^{-1}} \right) \left(\frac{R_*}{7 \times 10^8 \text{ cm}} \right)^3 \left(\frac{B_p}{\text{MG}} \right) \left(\frac{B_{\varphi}}{\text{mG}} \right) \text{ erg s}^{-1}. \quad (6.32)$$

The flux in the UV band was measured as 10^{-9} erg cm $^{-2}$ s $^{-1}$ (Maran et al. 1991) and the UV luminosity – which is likely to be equal to the accretion power of the disk and the boundary layer – is then

$$L_{\text{UV}} = 1.2 \times 10^{35} \left(\frac{d}{\text{kpc}} \right)^2 \text{ erg s}^{-1}. \quad (6.33)$$

With a derived distance of 2.5 kpc, this suggests an minimal accretion rate of $3.5 \times 10^{-8} M_{\odot} \text{ yr}^{-1}$ and therefore an ejection efficiency of 27 %.

6.3.1 The magnetic model

Let Ψ be a magnetic surface anchored at the inner radius of the accretion disk. Then this surface remains always inside the jet up to large distances. Using the constants of motion along this surface and the jet parameters, one can make estimates.

As magneto-centrifugally driven jets have fast-magnetosonic Mach numbers $M_{\text{fm}} \sim 3$, the total magnetic field in the jet should be

$$\sqrt{B_{p,\text{jet}}^2 + B_{\varphi,\text{jet}}^2} = \frac{4}{3} \pi \rho_{\text{jet}} v_{\text{jet}} = 0.06 \text{ mG}. \quad (6.34)$$

Using the conservation of flux $\Psi = B_p R^2$ and assuming $B_{\varphi,0} \ll B_{p,0}$, the total magnetic field near the white dwarf is

$$B_{p,0} \sim 28 \text{ kG}. \quad (6.35)$$

With the conservation of current $I = R B_{\varphi}$, the toroidal field inside the jet is then

$$B_{\varphi,\text{jet}} \ll 1 \text{ G}, \quad (6.36)$$

and should be dominant inside the jet. The magnetic pressure is then of the order of $10^{-2..-3} \text{ g s}^{-2} \text{ cm}^{-1}$, while the thermal pressure is about $10^{-3} \text{ g s}^{-2} \text{ cm}^{-1}$.

A magnetic field has been detected only in one symbiotic system (Z Andromedae, Sokoloski & Bildsten 1999). They interpreted an observed periodic photometric variability as the Keplerian spin period at the magnetospheric radius r_{mag} , where the magnetic pressure of the WD's field is comparable to the ram pressure of the accreted material. This radius can be calculated as

$$\begin{aligned} r_{\text{mag}} &= \left(\frac{B^4 R^{12}}{32 G M \dot{M}^2} \right)^{1/7} = \\ &= 3.6 \times 10^9 \left(\frac{B}{\text{MG}} \right)^{4/7} \left(\frac{R}{7 \times 10^8 \text{ cm}} \right)^{12/7} \left(\frac{M}{M_{\odot}} \right)^{-1/7} \left(\frac{\dot{M}}{10^{-8} M_{\odot} \text{ yr}^{-1}} \right)^{-2/7} \text{ cm}, \end{aligned} \quad (6.37)$$

which leads to a period of

$$\begin{aligned} P &= 2\pi \sqrt{\frac{r_{\text{mag}}^3}{G M}} = \\ &= 116 \left(\frac{B}{\text{MG}} \right)^{6/7} \left(\frac{R}{7 \times 10^8 \text{ cm}} \right)^{18/7} \left(\frac{M}{M_{\odot}} \right)^{-5/7} \left(\frac{\dot{M}}{10^{-8} M_{\odot} \text{ yr}^{-1}} \right)^{-3/7} \text{ s}. \end{aligned} \quad (6.38)$$

In the case of Z And, the measured period was about 28 min, equivalent to a magnetic field of about 22 MG (Sokoloski & Bildsten 1999). Assuming a lower magnetic field in MWC 560 of $B = 100$ kG, such oscillations should also be present with a period of 16 s, which is certainly below any observable limit.

All derived estimates, which are consistent with each other, and the fact, that a magnetic would not be observable in MWC 560 with the method of Sokoloski & Bildsten (1999), make likely that the ejection is really magnetically driven – or at least do not reveal any reason against it.

6.3.2 The pressure model

As mentioned in section 6.2, Soker & Regev (2003) assumed that the magnetic field inside the jet would undergo fast reconnection which would heat up the plasma to temperatures making the gas visible in X-rays. The maximum temperature up to which the gas would be heated can be estimated by equipartition (Tanuma et al. 2003) as

$$T_{\max} \sim 10^6 \left(\frac{n}{10^6 \text{ cm}^{-3}} \right)^{-1} \left(\frac{B}{100 \text{ mG}} \right)^2 \text{ K.} \quad (6.39)$$

The emissivity in Bremsstrahlung, created by reconnection, would then be $10^{-12} \text{ erg s}^{-1} \text{ cm}^{-3}$ and, multiplied by the jet area and an assumed jet length of 100 AU, the total luminosity would be $10^{30} \text{ erg s}^{-1}$. With again a distance of 2.5 kpc, the flux would be $10^{-15} \text{ erg s}^{-1} \text{ cm}^{-2}$. MWC 560 is no source in the *ROSAT* all-sky survey, as the flux limit of *ROSAT* is $(3 \times 10^{-12} \text{ erg s}^{-1} \text{ cm}^{-2})$, Cruddace et al. 2002).

Using the observables \dot{M} , L_{jet} and \dot{P}_0 , one can fix in principle the two free parameters χ and Γ of the model of Soker & Regev (2003).

Fixing the model highly depends on estimating the right mass accretion rate which, however, is rather difficult. As estimated in the last section, the mass accretion rate must be larger than $3.5 \times 10^{-8} M_{\odot} \text{ yr}^{-1}$ to explain the observed UV luminosity. Here the kinetic luminosity of the jet is ignored. Therefore from mass outflow rates follows $\chi f_m < 0.27$. As $\chi < 1$ and $f_m < 0.2$ for $0 < \Gamma < 1$, this should be even by far smaller, but it is only possible to guess the real values of χ and Γ due to these incertainties.

This scenario was only introduced in analytic estimates and now has to be verified qualitatively and quantitatively in numerical simulations.

6.3.3 The outburst period of pulsed jet formation

As shown in chapter 2.5, every seven days pulses arise. We have shown in chapter 4, that the most likely pulse model is that with a doubled jet velocity and a similar jet density during pulses. One possible explanation for this variability can be found by investigating a related class of objects: dwarf novae. Also there accretion onto white dwarfs occur and outbursts are triggered by a highly enhanced mass accretion rate due to a disk instability (Warner 1995; Lasota 2001). The period of seven days in MWC 560 can be reproduced by models of this disk instability using reasonable parameters of the disk and central object as $\dot{M} = 10^{17} \text{ g s}^{-1}$, $M = 0.6 M_{\odot}$, $\alpha = 0.04$, $r_{\text{in}} = 8.5 \times 10^8 \text{ cm}$, $r_{\text{out}} = 2 \times 10^{10} \text{ cm}$ (Fig. 14 in Lasota 2001).

Chapter 7

Simulations of Jet Formation

In this chapter, simulations to model the jet formation in symbiotic stars will be presented. Different initial configurations and boundary conditions were used whose effects will be discussed.

7.1 Attempts to reproduce the results of Casse & Keppens (2002)

As mentioned in chapter 6, in Casse & Keppens (2002, 2004) and Kato, Mineshige & Shibata (2004) the accretion disk was considered self-consistently for the first time. Therefore it is natural to start with one of their models – we have chosen that of Casse & Keppens (2002).

7.1.1 Initial conditions

As initial condition these authors used an accretion disk which is a modified self-similar standard disk (Shakura & Sunyaev 1973). The scale height ϵ , which is defined as

$$\epsilon = \frac{H}{r} \quad (7.1)$$

with the local height of the disk and the cylindrical radius r from the central object, is chosen to be constant ($\epsilon = 0.1$). From the assumption of vertical hydrostatic equilibrium inside the disk and Keplerian rotation, the power-law of the density profile follows which was modified by the authors to

$$\rho(r, z, t = 0) = \rho_0 \frac{R_0^{3/2}}{(R_0^2 + r^2)^{3/4}} \left(\max\{10^{-6}, [1 - \frac{(\gamma - 1) z^2}{2 H^2}]\} \right)^{1/(\gamma - 1)} \quad (7.2)$$

with γ the polytropic index of the equation of state

$$p = \kappa \rho^\gamma \quad (7.3)$$

and ρ_0 a normalization constant. γ is set to $5/3$. As the authors use dimensionless equations, in each magnetohydrodynamical quantity such a normalization will occur, as *NIRVANA* solves the MHD equations in SI units. These constants will be calculated below. R_0 is a smoothing length introduced to avoid singularities in the denominator which is set to $R_0 = 4 R_i$. R_i is the inner radius of the accretion disk which will be one of the model parameters and plays the role of a unit length in our model. Also the velocities follow power-laws: the azimuthal velocity is a slightly deviated Keplerian profile

$$v_\phi(r, z, t = 0) = v_0 (1 - \epsilon^2) \frac{R_0^{1/2}}{(R_0^2 + r^2)^{1/4}} \exp\left(-2 \frac{z^2}{H^2}\right) \quad (7.4)$$

with the velocity normalization

$$v_0 = \Omega_K(R_i) R_i = \sqrt{\frac{G M_{\text{CO}}}{R_i}}. \quad (7.5)$$

The radial velocity component describes accretion motion scaled as the angular velocity and the sound speed

$$v_r(r, z, t = 0) = -v_0 m_S \frac{R_0^{1/2}}{(R_0^2 + r^2)^{1/4}} \exp\left(-2 \frac{z^2}{H^2}\right) \quad (7.6)$$

and the vertical component secures the disk equilibrium with

$$v_z(r, z, t = 0) = v_r(r, z, t = 0) \frac{z}{r}. \quad (7.7)$$

The constant m_S is chosen to be smaller than unity ($m_S = 0.3$) which is equal to subsonic poloidal inflow (Casse & Keppens 2002).

The magnetic field strength can be calculated introducing the plasma beta defined as

$$\beta = \frac{p_{\text{gas}}}{p_{\text{magn}}} = \frac{2 \mu_0 p_{\text{gas}}}{B^2}. \quad (7.8)$$

The magnetic field should have global topology only with a non-vanishing vertical component

$$B_z(r, z, t = 0) = B_0 \frac{R_0^{3\gamma/4}}{(R_0^2 + r^2)^{3\gamma/8}} \frac{1}{\sqrt{\beta}}, \quad B_r(r, z, t = 0) = B_\phi(r, z, t = 0) = 0. \quad (7.9)$$

The normalization follows to

$$B_0 = \sqrt{2 \mu_0 \kappa \rho_0^{\gamma/2}}. \quad (7.10)$$

This initial condition should be iterated in the framework of *resistive* MHD. Therefore one has to make an ansatz to describe the resistivity η . Casse & Keppens (2002) have used an ansatz similar to the α -viscosity of Shakura & Sunyaev (1973), but with the Alfvén velocity instead of the sound speed, i.e.

$$\eta = \alpha_m v_A|_{z=0} H \exp\left(-2 \frac{z^2}{H^2}\right). \quad (7.11)$$

α_m was set to 0.1.

The free parameters in the model are now ρ_0 , R_i , R_0 , κ , ϵ , m_S , α_m and γ . These should be converted to the physical parameters M_{CO} , M , R_i , R_0 , ϵ and m_S , α_m and γ . The density normalization is, of course, depending on the assumed mass accretion rate (in the equatorial plane) as

$$\dot{M} = -4 \pi R_{\text{out}} H \rho v_r \quad (7.12)$$

which leads to

$$\rho_0 = \frac{\dot{M}}{4 \pi \epsilon m_S R_{\text{out}}^2 v_0}. \quad (7.13)$$

Using the assumption of hydrostatic equilibrium inside the disk, the polytropic constant κ is not independent of ρ_0 and v_0 :

$$\kappa = \frac{\epsilon^2 v_0^2 (M_{\text{CO}})}{\sqrt{16/17} \gamma} \rho_0^{-(\gamma-1)}. \quad (7.14)$$

The square root is a result of the offset R_0 .

A problem with the initial conditions of Casse & Keppens (2002) is the fact that the disk structure was chosen as a slightly deviated standard disk which, however, is an unmagnetized disk. It would be more appropriate to start with a solution of a magnetized disk as found e.g. by Campbell (1997) or with a completely other approach (see below).

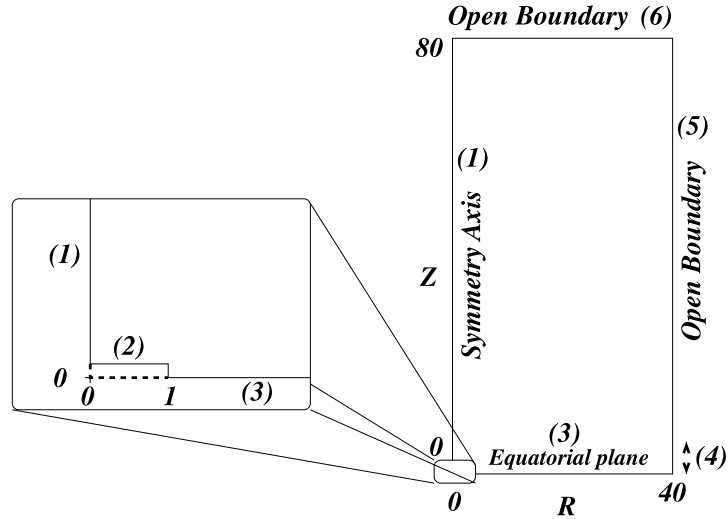


Figure 7.1: Sketch of the boundary conditions used by Casse & Keppens (2002)

7.1.2 Boundary conditions

To reproduce the results of Casse & Keppens (2002), it is surely not sufficient to start with their initial conditions only, but we have to implement their boundary conditions. The boundaries of the two-dimensional computational domain was splitted into 7 different regions (Fig. 7.1), four of which are standard conditions: in the equatorial plane anti-mirror symmetry was introduced, on the rotational axis conditions of a symmetry axis were used, the upper radial and upper vertical boundary were modeled with open outflow conditions. Three additional conditions were imposed: on the upper radial boundary inside the disk ($z < H$), a source region ensures a constant accretion rate into the disk. Near the origin of the coordinate system, a rectangular box was excluded, whose radial extent was chosen to be R_i and whose vertical extent was set to two cells in Casse & Keppens (2002) and also to R_i in Casse & Keppens (2004). The reason for this increasing of the vertical box height became clear in our first simulations. The upper vertical box boundary was implemented as “sink” conditions as it was called by Casse & Keppens (2002) which means a simple copy of the values above the boundary inside the boundary. In radial direction, outflow conditions were used to ensure accretion from the computational domain inside the box.

With this setup, one problem arose in our simulations with the boundary condition of the upper right corner cell of the box. This single cell was treated as belonging to the sink boundary as well as to the outflow boundary. This created unphysical magnetic monopoles in this single cell and therefore a non-vanishing divergence of B and additional forces near the box (Fig. 7.2). One way to avoid this behavior is to enlarge the box to reduce this effect as done in Casse & Keppens (2004). However, this is not a saturating solution, as well as the whole box seems to be unmotivated.

Due to these reasons, we changed to a spherical coordinate system and imposed anti-mirror conditions on the inner radial boundary to model the solid surface of the compact object. This leads to a reduction of the time-step by a factor of 10 at the beginning of the simulation up to a factor of 10^3 , when the time-step stays stationary. Its values were then of the order of 10^{-4} s or 10^{-10} of an orbit at the inner radius and 10^{-7} s or 10^{-13} of an orbit, respectively. The evolved time was 1000 s and 50 s, respectively.

Therefore the simulations were stopped and alternative setups were searched.

7.2 Torus simulations

Another approach apart from a more or less standard disk as initial condition is to begin with a rotating torus inside the computational domain. One advantage of this setup is that all material is already inside the domain initially and no matter source has to be implemented on the boundaries. Therefore we started another branch of simulations with tori as initial conditions.

7.2.1 Initial conditions

Starting with the static hydrodynamics equations, from the momentum equation follows

$$\frac{1}{\rho} \nabla p = -\nabla \Phi + \frac{l^2}{r^3} \nabla r. \quad (7.15)$$

r is again the cylindrical radius. With the polytropic equation of state and the identity

$$\nabla \left(\frac{p}{\rho} \right) = \frac{\gamma - 1}{\gamma} \frac{1}{\rho} \nabla p \quad (7.16)$$

the equation (7.15) can be integrated to

$$\frac{\gamma}{\gamma - 1} \frac{p}{\rho} + \Phi + \int_r^\infty dr' \frac{l(r')^2}{r'^3} = W_0. \quad (7.17)$$

Under the assumption of constant l , the integral can be solved to

$$\frac{\gamma}{\gamma - 1} \frac{p}{\rho} + \Phi + \frac{1}{2} \frac{l^2}{r^2} = W_0 \quad (7.18)$$

with which the density is then

$$\rho = \left(\frac{1}{\kappa} \frac{\gamma - 1}{\gamma} \left(W_0 - \Phi - \frac{1}{2} \frac{l^2}{r^2} \right) \right)^{1/(\gamma - 1)}. \quad (7.19)$$

The angular momentum of the torus is then dependent of its radial position R_0 and the choice of Φ as

$$l(R_0) = \sqrt{GM R_0} \frac{R_0}{R_0 - 2R_g}, \quad (7.20)$$

if Φ is chosen to be

$$\Phi = -\frac{GM}{R - 2R_g}. \quad (7.21)$$

With a smoothing length $R_g = (GM)/c^2$, this is equal to the Pseudo-Newtonian potential (Paczynski & Wiita 1980), used to model relativistic effects of a Schwarzschild metric around Neutron stars and Black Holes. For white dwarfs, this is not necessary. If Newtonian Gravity ($R_g = 0$) is assumed, the last term on the right hand side in equation (7.20) vanishes. R is the spherical radius.

Inside the torus, the velocity components are then

$$v_\phi = \frac{l(R_0)}{r} \quad v_r = v_\theta = 0. \quad (7.22)$$

Outside the torus, Keplerian rotation is assumed

$$v_\phi = \Omega_K r \quad v_r = v_\theta = 0 \quad (7.23)$$

with

$$\Omega_K = \sqrt{GM R} \frac{R}{R - 2R_g} \frac{1}{r^2}. \quad (7.24)$$

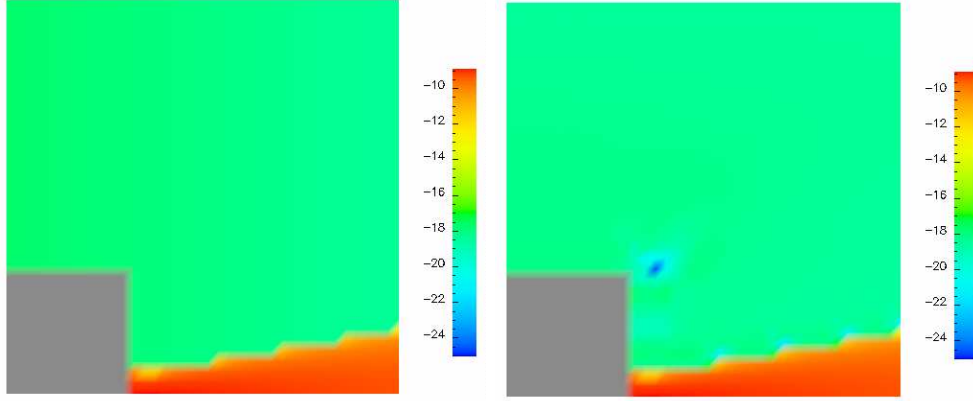


Figure 7.2: Density anomalies created by the corner of the box (left: initial condition; right: after 1000 s)

To initialize the magnetic field and to assure that its divergence vanishes, we calculate the magnetic field components from the vector potential \vec{A} defined as

$$\vec{B} = \nabla \times \vec{A}. \quad (7.25)$$

The only considered component of \vec{A} is set identical to the internal energy

$$A_\phi = e \quad (7.26)$$

to leave the plasma β constant within the torus. This results in the following magnetic field components

$$B_R = \frac{1}{R \sin \theta} \frac{\partial}{\partial \theta} (\sin \theta e) \quad B_\theta = -\frac{1}{R} \frac{\partial}{\partial R} (R e) \quad B_\phi = 0 \quad (7.27)$$

in spherical coordinates, or

$$B_r = -\frac{\partial}{\partial z} e \quad B_z = \frac{1}{r} \frac{\partial}{\partial r} (r e) \quad B_\phi = 0 \quad (7.28)$$

in cylindrical coordinates, respectively. Afterwards, these components were scaled to achieve an assumed plasma $\beta = 10^3$. No global external magnetic field was implemented!

The free model parameters were then adapted for convenience to simulate the accretion onto a stellar black hole with $M = 10 M_\odot$. The density maximum of the torus was positioned to $8 R_g$. These values, of course, are not suitable for Symbiotic Systems, but a problem arose to find a torus solution at larger distances within the computational domain. All distances are given in units of R_g . The orbit time at the density maximum is then about 3×10^{-3} s.

7.2.2 The effect of a solid surface onto the jet formation process

Analog to section 7.1, we started two simulations with different boundary conditions at the inner radial coordinate, one with open conditions (run A) and one with anti-mirror conditions to model the solid surface of the central object (run B). The aim of these simulations was to investigate the influence of the solid surface and the reliability of the analytic assumptions of Soker & Regev (2003). A third simulation (run C) was performed similar to run A, but in cylindrical coordinates to investigate the influence of different coordinate systems. Here the cylindrical radius starts at $2 r_g$, i.e. a cylinder along the axis is cut out and the inner radial boundary is chosen to be open.

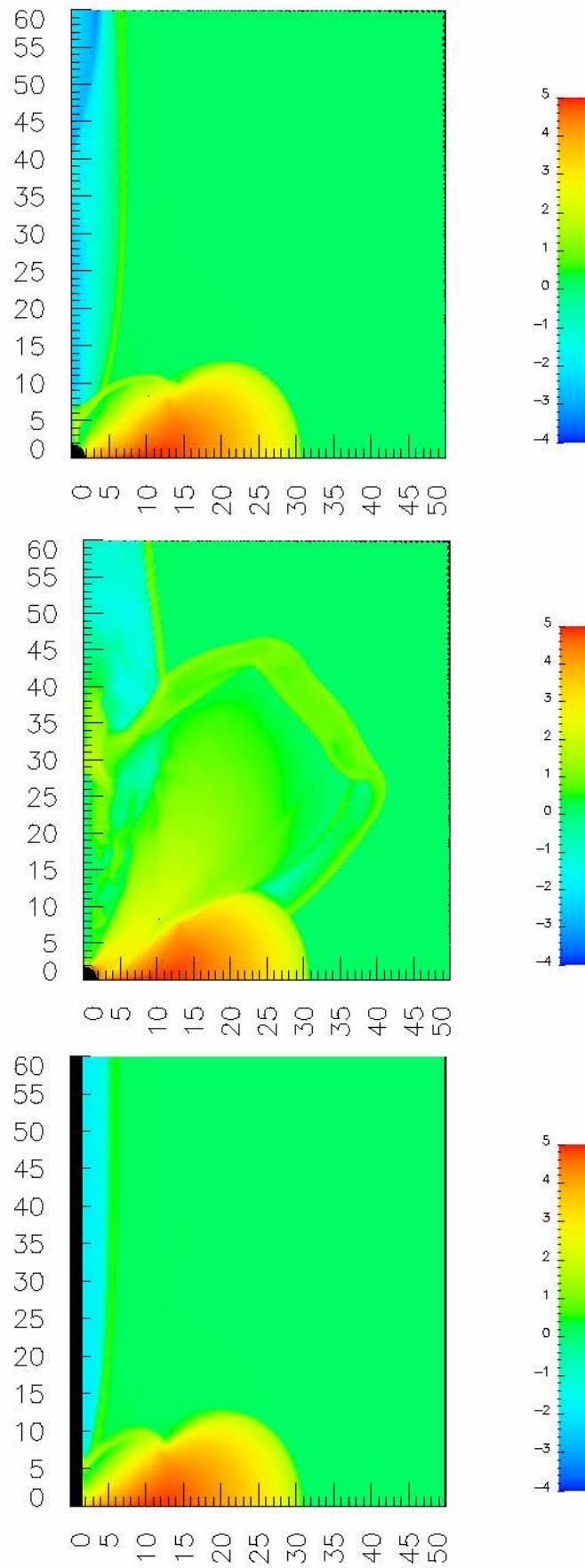


Figure 7.3: Plots of the density of run A (left), run B (middle) and run C (right) after 4.5×10^{-3} s; the coordinates are in units of r_g

The accretion and ejection components

In Fig. 7.3, the density is plotted for the three runs after 4.5×10^{-3} s (1.5 torus orbits). One can clearly see that activity is triggered much faster in run B with the solid boundary.

In run A accretion sets in immediately due to the magnetorotational instability inside the torus. After almost one revolution of the torus, it gets in contact with the central object, which leads to a re-distribution of matter in the now established disk. The inner part of the disk puffs up creating an expanding bubble. Along the rotation axis, a funnel is created whose cross section grows with evolving time.

Also in run B the accretion process starts immediately and also the funnel is created. Additionally, a boundary layer with a radial extent of one fifth of the black hole radius forms on the surface of the central object. Due to its high pressure, a flare occurs. This flare bubble, now created by the boundary layer, not by the accretion disk, expands along the surface of the torus with high velocities and also high density. The density contrast of the bubble is $\eta = 10^2$, i.e. the bubble is overdense. The expansion of the bubble is powered by a continuous high pressure flow from the boundary layer. The expansion direction of the bubble is along a latitude of around $40\text{-}50^\circ$. If an external magnetic field would be present, perhaps the flow could be bended to directions parallel to the axis.

Inside the swept out funnel along the axis, after three orbits in run C (9×10^{-3} s) a high velocity component emanates out of the spherical expansion. This funnel jet has a head velocity between $c/3$ and c and a density contrast of $\eta = 10^{-2}$. As this is only seen in run C and not in run A, the open boundary might create this flow.

In Fig. 7.4, the time evolution of the accretion rate in the equatorial plane at $r = 4 r_g$ is plotted. The qualitative behavior seems to be equal in all runs, but in run C the accretion rate is always higher. It is possible that the open boundary near the axis causes a global radial inflow which is superimposed to the accretion rate which is visible in runs A and B. The accretion rate in the latter runs seems to be equal until 3.2×10^{-3} s, i.e. no causal connection is established between the boundary layer and the accretion flow itself until then. After that point, the flare coming from the boundary layer destabilizes the accretion flow and enhances its rate.

The jet emission efficiency

In Fig. 7.5, a poloidal slice at $r = 10 r_g$ of the mass accretion/outflow rate of run A and run B at different times is plotted. One can clearly see the different accretion and ejection components in this simulation.

The first peak at about 40° represents the flares created by the boundary layer in run B and

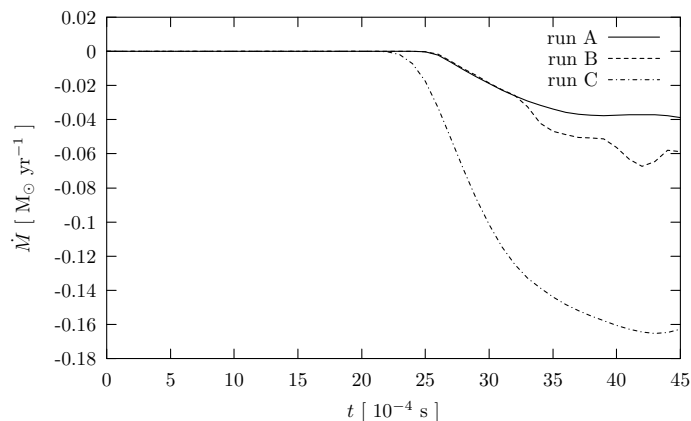


Figure 7.4: Time evolution of the accretion rate in the equatorial plane at $r = 4 r_g$

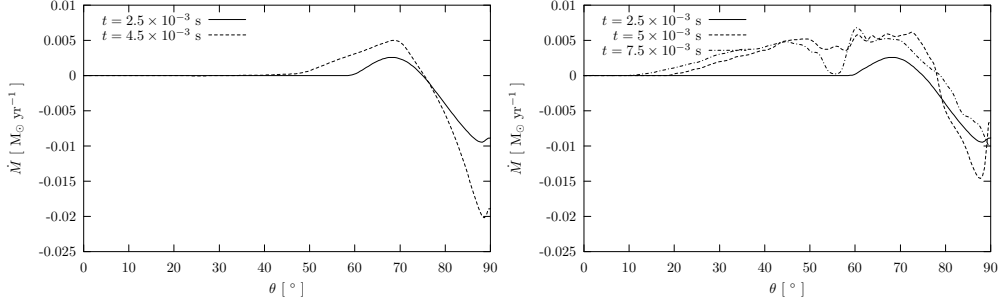


Figure 7.5: Poloidal slice at $r = 10 r_g$ of the mass accretion/outflow rate of runs A (left) and B (right) at different times

has no corresponding feature in run A. The second peak at about 70° is identical with an outflow along the surface of the torus which is common in all runs. At larger values of θ , the accretion flow can be seen. Remarkably, the accretion flow is slightly above the equatorial plane in both runs. At this distance of $10 r_g$ the accretion rate is higher in run A than in run B, while at smaller distance the behavior is vice versa (Fig. 7.4). The accretion rate in all peaks is highly time dependant.

Using the mass accretion rate in the equatorial plane and the mass ejection rate of the two peaks, one can calculate an ejection efficiency of the system. This efficiency is plotted in Fig. 7.7. After an initial phase of global ejection in the equatorial plane until about 2×10^{-3} s, the mass fraction outflowing along the torus surface (second peak) compared to that being accreted is almost constant between 25–30 % in run A, while oscillating around a mean of about 50 % in run B. The oscillations are created by the flaring boundary layer. In run A, the efficiency of ejection in the first peak is only one percent, the ejection peak is not really present. In run B, however, the ejection efficiency of the first peak is comparable to that of the second peak, i.e. also in the range between 40–50 %.

Structure of the accretion flow

The next step is to investigate the structure of the accretion flow and the question about the influences of the emergence of the boundary layer. In Fig. 7.8, the main magnetohydrodynamical quantities of the flow are plotted, namely the density, the ratio of angular momentum to Keplerian angular momentum, the radial and azimuthal velocity components, the poloidal magnetic field components, the azimuthal magnetic field component, the accretion rate and the temperature.

In the first plot, showing the density distribution in the equatorial plane, the boundary layer

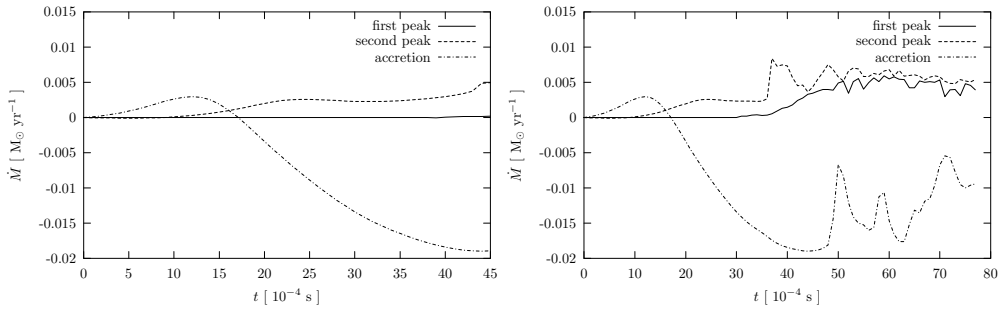


Figure 7.6: Time evolution of the ejection peaks and the accretion disk in run A (left) and run B (right)

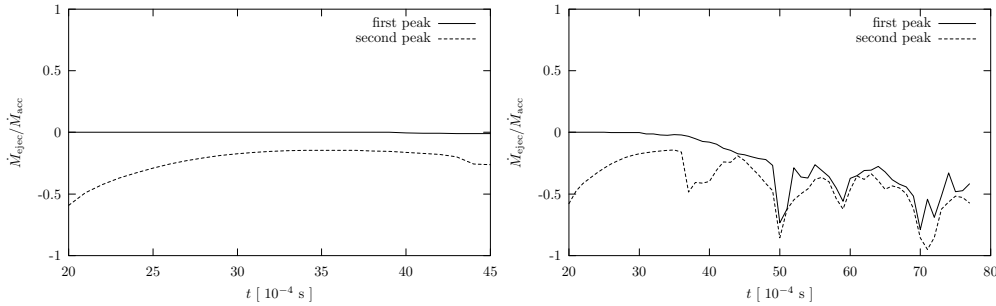


Figure 7.7: Efficiency of the ejection mechanism in the two ejection peaks in run A (left) and B (right)

between 2 and $2.4 r_g$ (1-1.2 radii of the central object) is apart from the torus the most prominent feature in run B. The density increases by more than an order of magnitude with respect to the accretion flow. In run A, the open boundary representing the black hole arranges for a density, decreased by a factor of 4-5, due to the drain into the black hole. In contrast to run B in which the accretion flow is always rotating super-Keplerian, the angular momentum of the flow in run A drops below the Keplerian angular momentum for distances smaller than about $3 r_g$. This is also an effect of the drag created by the black hole which also shows oneself in the radial velocity component. Between 3 and $5 r_g$, the accretion flow is even faster in the model with boundary layer, in the vicinity of the central object, however, the (negative) accretion velocity highly increases in run A, while decreases before reaching the boundary layer itself. The absolute values of all velocity components, which become super-luminal in a few cases, are, of course, unphysical due to the fact that *NIRVANA* is not a special relativistic code. The qualitative behavior, however, should be unchanged by this fact. The smaller toroidal velocity component of the flow in run B is a further effect of the boundary layer which decelerates the flow by thermal pressure. That results in a large value of β , in spite of a large magnetic field. The emergence of the boundary layer creates a peak at its surface of the radial and poloidal components of the magnetic field, which is perhaps created by strong shocks inside it. This highly magnetized region extends to a distance of $60 r_g$ from the equatorial plane leading to a positive total poloidal current, instead of negative values near and inside the torus (Fig. 7.9), which then can drive jets also magnetically.

7.2.3 Structure of the BL ejection component

Now we investigate the structure of the ejection component itself. In Fig. 7.10 the main magnetohydrodynamical quantities along a slice through the ejection component at $\theta = 45^\circ$ are plotted.

The variability of the accretion rate and with it of the ejection rate leaves its mark in form of a rich substructure in all variables. Similar to our jet propagation simulations in chapter 3 one can distinguish knots with an enhanced density, magnetic field components and temperature as in the adiabatic models. In the velocity components, however, the knots are not significant, only a global deceleration can be detected.

7.3 Implications for symbiotic stars

We have presented a model of a somewhat hypothetical object with solid surface accreting from a rotating torus. We have seen that the emergence of a boundary layer results in an additional ejection components. Now we have to scale our results to the objects we are mainly interested in, to symbiotic stars.

As these results are found using ideal magnetohydrodynamics, whose equations can be written

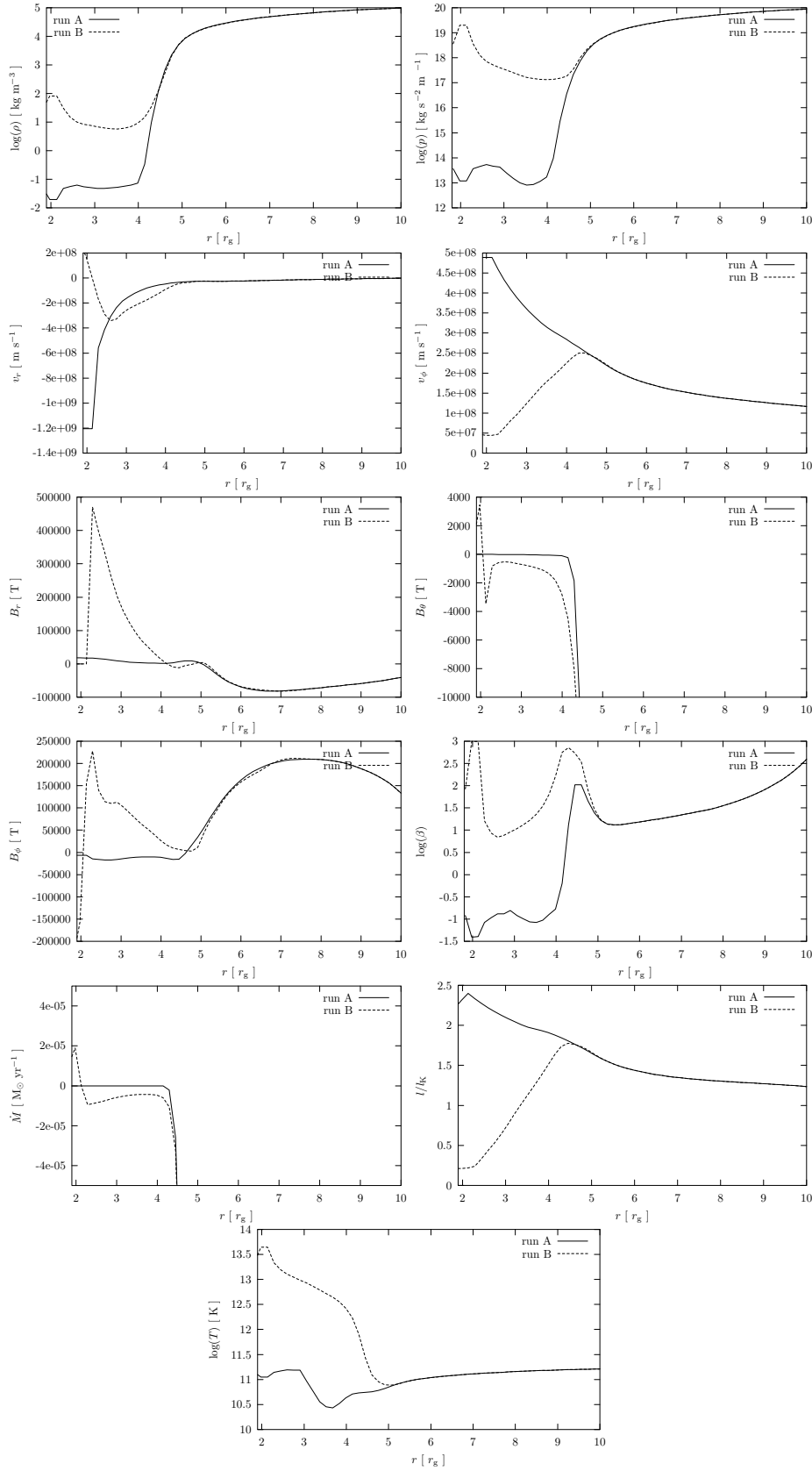


Figure 7.8: Structure of the accretion flow after 2.2×10^{-3} s: density, pressure, radial and azimuthal velocity components, poloidal magnetic field components, azimuthal magnetic field component, plasma β , accretion rate, ratio of angular momentum to Keplerian angular momentum and temperature

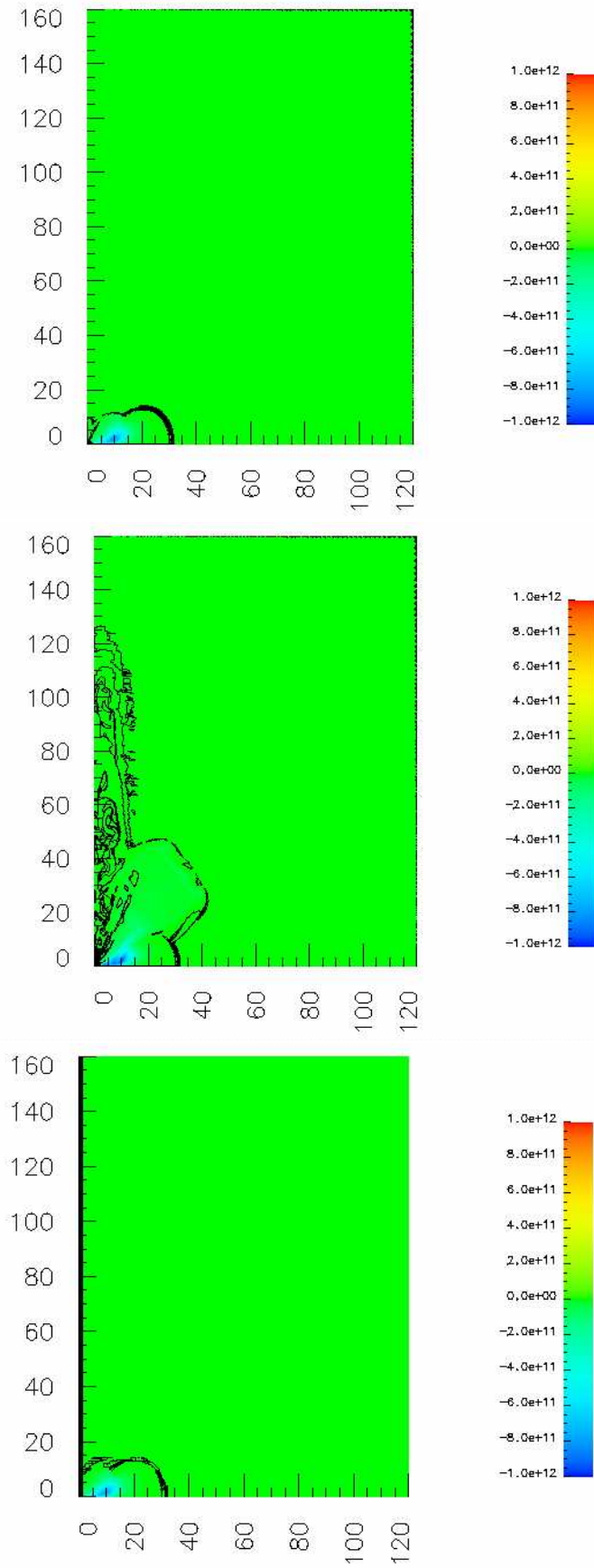


Figure 7.9: Plots of the total poloidal current $r B_\phi$ after 4.5×10^{-3} s for run A (left), run B (middle) and run C (right) with logarithmic contour lines from $I = 0$ to $I = 10^{12}$ A

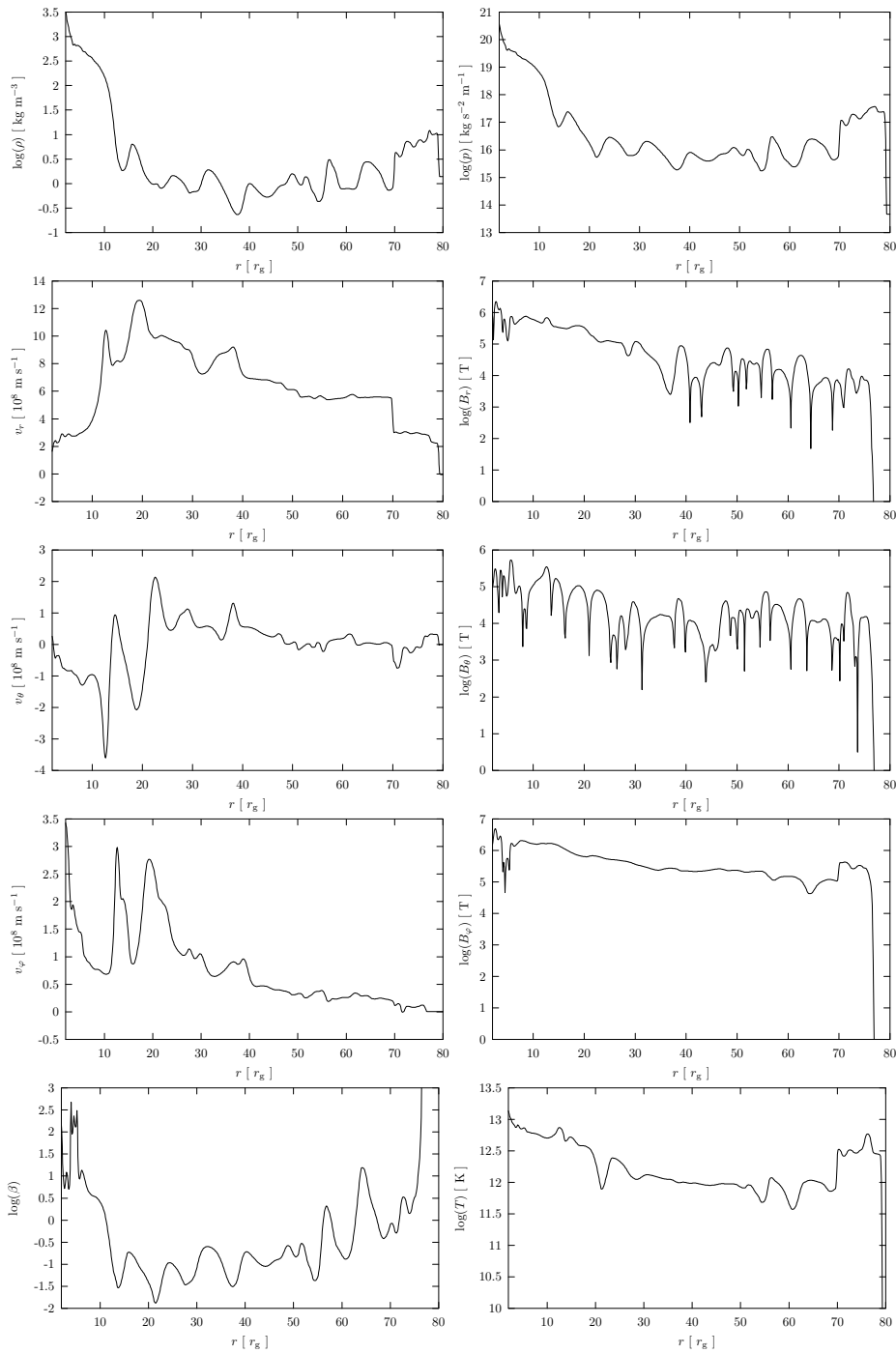


Figure 7.10: Structure of the ejection component after 7.5×10^{-3} s: density, pressure, radial and azimuthal velocity components, poloidal magnetic field components, azimuthal magnetic field component, plasma β , accretion rate, ratio of angular momentum to Keplerian angular momentum and temperature

in a dimensionless manner, all quantities can be normalized to naturally arising combinations which depend on parameters of the central object. This approach was presented in the other direction in section 7.1.1.

The natural length scale is the inner radius of the disk, in our simulation $2r_g$, the velocity scale is the Keplerian velocity at this radius (eq. 7.5). The appendant time scale is then the inverse of the Keplerian period. The magnetic field scale is given by the polytropic equation of state with the density scale and the plasma β (eq. 7.10). The density scale depends on the mass accretion rate and the natural mass flux scale.

The typical propagation velocity of the ejection component was $6 \times 10^8 \text{ m s}^{-1}$. The fact that it is superluminal should not disturb us at this moment as it was achieved with a non-relativistic code. As the velocity scale depends on the square root of the compactness M/R of the central object, this gives about 800 km s^{-1} for a symbiotic star. Assuming an accretion rate of $10^{-8} M_\odot \text{ yr}^{-1}$, the density of the jet would be of the order of $9 \times 10^{-14} \text{ kg m}^{-3}$ or $9 \times 10^{-17} \text{ g cm}^{-3}$. This is a number density of $5 \times 10^7 \text{ cm}^{-3}$. Both values, the velocity and the density, are consistent with jets in symbiotic stars.

With an polytropic index of $5/3$, the magnetic field components could be scaled to 10^{-7} T or 1 mG . Again this is very reasonable.

These estimates show that our model could be adapted to symbiotic stars in principle, but a more appropriate model should be calculated in the future anyways.

Chapter 8

Discussion and Outlook

As we have already discussed the main results in the corresponding chapters, we will only summarize them in a shorter way and will give impressions of the next steps to improve our investigations and models of the formation and propagation of jets in symbiotic stars.

8.1 What we have done

We have presented simulations of pulsed jets in symbiotic stars. Two main types of simulations were performed, namely a grid of eight adiabatic small scale simulations and one small scale simulation including radiative cooling effects. These models have been first investigated in terms of their structure and emission. The simulations have shown a global similarity in morphology and the resulting basic jet parameters among the adiabatic models, but large deviations of the model with cooling from them. Large differences in their internal structure have been listed and their implications on their observability have been discussed. We have shown by comparing our results with observational data, that – as formerly expected – only the model with cooling produces a reliable description of real jets in symbiotic stars.

We have introduced a new tool to examine the internal structure, the velocity and the density distribution of jets, if their jet axis is perpendicular to the line of sight as in the object MWC 560. By means of synthetical absorption line profiles we have investigated the influences of different model parameters, such as density and velocity of the pulses, or of geometrical properties as the inclination. From observations, we have derived real parameters of MWC 560. Again, we have shown that considering cooling effects is very important to model the real jet correctly. In the adiabatic models the derived jet temperatures were too high to allow for Ca II absorptions, which are, however, detected in the spectrum of MWC 560. This ionization problem has almost completely been solved in the model with cooling, except for a small insufficiency in our cooling treatment.

Driven by the assumption of the occurrence of new effects due to the transition from an underdense to an overdense jet, we have performed one adiabatic large scale simulation and two large scale simulations with radiative cooling. Surprisingly, this new effect was not detected. Instead of that, the conclusion that the radial extent of the cooled jet remains constant has been disproven. The jet was even inflating including its knotty structure which improves the ability of the model to explain observations of jets in symbiotic stars with regard to their emission.

In the second part of this thesis, we have changed our focus from the propagation of jets in symbiotic stars to their emission and formation process. We have shortly reviewed the different processes assumed to be capable to accelerate and collimate the jet. By analytic estimates we have tried to decide which of the two main mechanisms – formation by MHD processes or formation by thermal pressure in the boundary layer (BL) – is more reliable to explain the observed parameters of jets. As they have given a slight preference of the BL mechanism, we have setup numerical simulations of a compact object with solid surface accreting matter from a rotating torus. Indeed,

they have shown an additional ejection component which could be collimated into a jet by a global magnetic field which was, however, omitted in our simulations. By another analytic estimates we have calculated the implications for jets in symbiotic stars and have proven that reliable jet parameters can be achieved.

8.2 What we have to do

A common feature – or drawback – of our simulations dealing with the propagation of jets in symbiotic stars was the two-dimensional treatment assuming axisymmetry. It is obvious, however, that the problem to be solved is fully three-dimensional due to the presence of the companion star. We have discussed that – at least in the models with cooling – the influence of this dimensional reduction should be only marginal. But to prove this, we have to perform new fully three-dimensional large scale simulations with the approximated cooling.

The torus simulations to show the influence of a solid surface were performed with parameters, as e.g. mass or size of the central object, which were not really suitable for symbiotic stars, but for a hypothetical black hole with solid surface. As the equations of magnetohydrodynamics can be made dimensionless, however, we were able to rescale the problem to our objects of interest. The next step would be to setup simulations with the suitable parameters and to look whether this scenario keeps on holding. To achieve this, we have to construct a rotating torus at larger distances from the central object and to adjust and vary its parameters to study accretion with different accretion rates.

Again also in these simulations, a two-dimensional treatment was used. The full description in three dimension could reveal new effects or details which we have to look for in new simulations. Another point is the amount of physics in our models. We used the equations of *ideal* MHD neglecting any cooling effects. Depending on the accretion rate, however, the boundary layer material can become optically thick which has to be taken into account. The additional equations in the flux-limited diffusion ansatz can not be solved anymore by *NIRVANA* and a new tool has to be used as e.g. *FLASH*. A new branch of simulations will be necessary. As cooling effects reduce the internal energy of the material and therefore also reduce its thermal pressure, it has to be shown, whether this new jet formation scenario is still reliable then.

Appendix A

The numerical codes

In this chapter, we describe the employed computer codes with the incorporated equations.

A.1 NIRVANA_C

With the code *NIRVANA* (Ziegler & Yorke 1997) we solve the following set of the hyperbolic differential equations of ideal hydrodynamics

$$\frac{\partial \rho}{\partial t} + \nabla(\rho \mathbf{v}) = 0 \quad (\text{A.1a})$$

$$\frac{\partial(\rho \mathbf{v})}{\partial t} + \nabla(\rho \mathbf{v} \otimes \mathbf{v}) = -\nabla p - \rho \nabla \Phi \quad (\text{A.1b})$$

$$\frac{\partial e}{\partial t} + \nabla(e \mathbf{v}) = -p \nabla \mathbf{v} + \Lambda(T; \rho_i) \quad (\text{A.1c})$$

$$p = (\gamma - 1) e. \quad (\text{A.1d})$$

Thereby ρ is the gas density, e the energy density, \mathbf{v} the velocity and γ the ratio of the specific heats at constant pressure and volume. *NIRVANA* uses second order accurate finite-difference and finite-volume methods and explicit time-stepping.

This code was modified by Thiele (2000) to calculate energy losses due to non-equilibrium cooling by radiative emission processes. The microphysics is introduced via the cooling term Λ in the energy equation and the following interaction equations for the species. When cooling is important, the above equations are supplemented by a species network

$$\frac{\partial \rho_i}{\partial t} + \nabla(\rho_i \mathbf{v}) = \sum_{i=1}^{N_s} \sum_{j=1}^{N_s} k_{ij}(T) \rho_i \rho_j \quad (\text{A.2})$$

with ρ_i the species densities satisfying $\rho = \sum_{i=1}^{N_s} \rho_i$ for the total density. k_{ij} are the rate coefficients for two-body reactions which are functions of the fluid temperature T and for which analytic expressions are used (Thiele 2000). The rate coefficients describing ionization of Cen (1992) and Shull & van Steenberg (1982) and those describing recombination of Verner & Ferland (1996), Shull & van Steenberg (1982) and Abel et al. (1997) are considered. The summations go over the N_s both atomic and molecular species included in the chemistry model. *NIRVANA_C* can handle up to 36 species (Thiele 2000).

In the optically thin case, the cooling rate is a function of the species densities and temperature, $\Lambda = \Lambda(T; \rho_i)$ (Sutherland & Dopita 1993). When cooling is very efficient, the chemistry network is solved in a time-implicit way (Thiele 2000). This code has been extensively tested in Thiele (2000) and Krause (2001).

When chemistry is solved dynamically with the full set of non-equilibrium equations, the various ionization states and concentration densities ρ_i of each element are calculated from the chemistry equations. They are used explicitly in the cooling functions as

$$\Lambda(T; \rho_i) = \sum_{i=1}^{N_s} \sum_{j=1}^{N_s} e_{ij}(T) \rho_i \rho_j + \Lambda_{BS}(T) \quad (\text{A.3})$$

with e_{ij} the cooling rates from two-body reactions between species i and j . Cooling rates due to ionization (Cen 1992; Shull & van Steenberg 1982), due to recombination (Verner & Ferland 1996; Cen 1992; Shull & van Steenberg 1982; Abel et al. 1997) and due to line cooling (Cen 1992; Pottasch 1984) are used. Λ_{BS} is the cooling function due to Bremsstrahlung. In this case, the equation of state has to be given in the form

$$T = \frac{\gamma - 1}{k_B} \frac{e}{\sum_{i=1}^{N_s} n_i}. \quad (\text{A.4})$$

The code in its present form can handle collisional excitation, collisional ionization, recombination, metal-line cooling and Bremsstrahlung.

A.2 NIRVANA2.0

NIRVANA2.0 Ziegler (2002) solves the equations of visco-resistive, compressible MHD

$$\frac{\partial \rho}{\partial t} + \nabla \cdot (\rho \mathbf{v}) = 0 \quad (\text{A.5})$$

$$\frac{\partial (\rho \mathbf{v})}{\partial t} + \nabla \cdot (\rho \mathbf{v} \otimes \mathbf{v}) = -\nabla p + \frac{1}{\mu} (\nabla \times \mathbf{B}) \times \mathbf{B} + \nabla \cdot \sigma - \rho \nabla \Phi \quad (\text{A.6})$$

$$\frac{\partial e}{\partial t} + \nabla \cdot (e \mathbf{v}) = -p \nabla \cdot \mathbf{v} + \sigma : \nabla \mathbf{v} + \frac{\eta}{\mu^2} |\nabla \times \mathbf{B}|^2 + \nabla \cdot (\kappa \nabla T) \quad (\text{A.7})$$

$$p = (\gamma - 1) e \quad (\text{A.8})$$

$$\frac{\partial \mathbf{B}}{\partial t} = \nabla \times (\mathbf{v} \times \mathbf{B} - \frac{\eta}{\mu} \nabla \times \mathbf{B}) \quad (\text{A.9})$$

$$\sigma_{ij} = \nu (\nabla v_{ij} + \nabla v_{ji} - \frac{2}{3} \nabla v \delta_{ij}) \quad (\text{A.10})$$

with the magnetic field \mathbf{B} , the gravitational potential Φ , dynamic viscosity ν , electrical resistivity η , magnetic permeability μ and thermal conductivity κ .

Appendix B

Publications

Parts of this thesis has been presented in the following publications (in chronological order):

- 1. Numerical Simulations of the pulsed Jet of MWC 560**
M. Stute, M. Camenzind, H. M. Schmid
in: "Symbiotic stars probing stellar evolution", Eds. R. L. M. Corradi, J. Mikolajewska, and T. J. Mahoney, ASP conference proceedings, Volume 303 (2003)
astro-ph/0210488
- 2. Formation and Propagation of Jets around Compact Objects**
M. Stute, M. Camenzind
in: "High Performance Computing in Science and Engeneering '03", Eds. E. Krause, W. Jäger, M. Resch, Springer, Berlin, Heidelberg (2003)
- 3. Hydrodynamical simulations of the jet in the symbiotic star MWC 560.**
I. Structure, emission and synthetic absorption line profiles
M. Stute, M. Camenzind, H. M. Schmid
accepted for publication in A & A
- 4. Large scale simulation of a cooled, pulsed jet in Symbiotic Stars**
M. Stute, M. Camenzind
in: "High Performance Computing in Science and Engeneering '04", Eds. E. Krause, W. Jäger, M. Resch, Springer, Berlin, Heidelberg (2004), in press

List of Figures

1.1	Examples of astrophysical jets	11
1.2	Sketch of a symbiotic star system	12
2.1	HST image of the jet and counter-jet of R Aquarii	18
2.2	Chandra image of the jet and counter-jet of R Aquarii	18
2.3	Outer and inner nebulosity around R Aquarii	19
2.4	Multi-component jet of CH Cygni	20
2.5	Jet absorption line structure	22
2.6	Anti-correlation between the high and low velocity components	23
2.7	Geometry of the outflow interpreting the observations	24
3.1	Sketch of the reduction from 3D to 2.5D simulations	27
3.2	Color plot of the density at day 380 for model i and ii	31
3.3	Color plot of the density at day 380 for model iii and iv	32
3.4	Color plot of the density at day 380 for model v and vi	33
3.5	Color plot of the density at day 380 for model vii and viii	34
3.6	Aspect ratio of the bow shocks; residuals from the linear function	35
3.7	Shape of the bow shock for the model i	36
3.8	Evolution of the pulses for model i	36
3.9	Slice of the Mach number for models i and vii and of the parallel velocity	37
3.10	Slice of the density, pressure and temperature	38
3.11	Radial profiles of the parallel and radial velocity component and Mach number	39
3.12	Radial profiles of the logarithm of density, pressure and temperature	40
3.13	Color plot of the density at day 74 for model i without and including cooling	41
3.14	Logarithm of temperature of the model i with cooling	42
3.15	Evolution of the pulses for model i with cooling	42
3.16	Slice of the Mach number and parallel velocity	44
3.17	Slice of the density, pressure and temperature	45
3.18	Radial profiles of the parallel and radial velocity and Mach number	46
3.19	Radial profiles of the density, pressure and temperature	47
3.20	Logarithm of temperature of the model i	49
3.21	Logarithm of Bremsstrahlung emission of the model i	49
3.22	Logarithm of Synchrotron emission of the model i	50
3.23	Logarithm of HI line emission of the model i	50
3.24	Logarithm of Bremsstrahlung emission of the model i with cooling	51
3.25	Logarithm of synchrotron emission of the model i with cooling	52
3.26	Logarithm of HI line emission of the model i with cooling	52
3.27	Evolution of different luminosities	53
4.1	Adiabatic model i for a pulsed jet at day 444: density and velocity	57
4.2	Pulsed jet model i with radiative cooling at day 74: density and velocity	58
4.3	Four different absorption regions	60

4.4	Synthetic absorption line profile for three different radii ;model i	61
4.5	Synthetic absorption line profile for three different radii; model i with cooling . . .	62
4.6	Synthetic absorption line profile for model i under different inclinations	62
4.7	Synthetic absorption line profile for model i with cooling under different inclinations	63
4.8	Equivalent width of the jet absorption	63
4.9	Theoretical absorption line profiles for values of the velocity bin size	65
4.10	Theoretical absorption line profiles for different values of the temperature threshold	66
4.11	Time variability of the high (negative) velocity component	67
4.12	Theoretical absorption line profile of model i for values of z_{\max}	69
4.13	Sequence of absorption line profiles for models i–iii	70
4.14	Sequence of absorption line profiles for model iv	71
4.15	Sequence of absorption line profiles for model i with cooling	71
5.1	Comparison of density and temperature plots	75
5.2	Size of the bow shock in parallel and radial direction	77
5.3	Evolution of the pulses for model i apc	78
5.4	Slice of the parallel velocity and Mach number	79
5.5	Slice of the logarithm of density, pressure and temperature	80
5.6	Logarithm of density of model i apc	81
5.7	Radial profiles of the parallel and radial velocity and Mach number	82
5.8	Radial profiles of the logarithm of density, pressure and temperature	83
5.9	Logarithm of Bremsstrahlung emission for model i apc	84
5.10	Logarithm of H I line emission for model i apc	84
5.11	Sequence of absorption line profiles for model i apc	85
5.12	Sequence of absorption line profiles for model iv apc	85
6.1	Schematic sketch of the accretion disk and the magnetic field	90
6.2	Schematic sketch of jet formation mechanism through star-disk-interaction	91
6.3	$f_m = f_m(\Gamma)$, $f_E = f_E(\Gamma)$ and $v_a/v_{\text{esc}} = v_a/v_{\text{esc}}(\Gamma)$	94
7.1	Sketch of the boundary conditions used by Casse & Keppens (2002)	99
7.2	Density anomalies created by the corner of the box	101
7.3	Plots of the density of three runs	102
7.4	Time evolution of the accretion rate	103
7.5	Poloidal slice of mass accretion/outflow rate	104
7.6	Time evolution of the ejection peaks and the accretion disk	104
7.7	Efficiency of the ejection mechanism in the two ejection peaks	105
7.8	Structure of the accretion flow	106
7.9	Plots of the total poloidal current	107
7.10	Structure of the ejection component	108

List of Tables

3.1	Parameters of the jet pulses	28
3.2	Axial and radial extent of the bow shock after 380 days and its aspect ratio	29
3.3	Slope of the radial vs. axial extent of the bow shock in the linear regime	30

Bibliography

- Abel, T., Anninos, P., Zhang, Y., Norman, M. L. 1997, *New Astron.* **2**, 181
- Aller, L. H., *Physics of Thermal Gaseous Nebulae*, (Astrophysics and space science library v. 112, D. Reidel Publishing Company, Dordrecht, 1984)
- Armitage, P. J. 2002, *MNRAS* **330**, 895
- van Belle, G. T., Lane, B. F., Thompson, R. R., Boden, A. F., Colavita, M. M., Dumont, P. J., Mobley, D. W., Palmer, D., Shao, M., Vasisht, G. X., Wallace, J. K., Creech-Eakman, M. J., Koresko, C. D., Kulkarni, S. R., Pan, X. P., Gubler, J. 1999, *A. J.* **117**, 521
- Bacciotti, F. 1997, in: *IAU Symp. 182: Herbig-Haro Flows and the Birth of Stars*, eds. B. Reipurth & C. Bertout, Kluwer Academic Publishers, p. 73
- Balbus, S. A., Hawley, J. F. 1991, *Ap. J.* **376**, 214
- Berman, L. 1932, *Pub. Astr. Soc. Pac.* **44**, 318
- Blandford, R. D., Payne, D. G. 1982, *MNRAS* **199**, 883
- Blondin, J. M., Fryxell, B. A., Königl, A. 1990, *Ap. J.* **360**, 370
- Bond, H. E., Pier, J., Pilachowski, C., Slowak, M., Szkody, P. 1984, *Bull. Am. Astr. Soc.* **16**, 516
- Buckley, D. A. H. 1992, in: *IAU Symp. 151: Evolutionary Processes in Interacting Binary Stars*, eds. Y. Kondo, R. F. Sistero, R. S. Polidan, Kluwer Academic Publishers, p. 421
- Burgarella, D., Livio, M., O'Dea, C., *Astrophysical Jets*, Proceedings of the Astrophysical Jets Meeting, Baltimore (Cambridge University Press, 1993)
- Brand, J., Blitz, L. 1993, *A & A* **275**, 67
- Breitmoser, E., Camenzind, M. 2000, *A & A* **361**, 207
- Camenzind, M. 1990, *RvMA* **3**, 234
- Camenzind, M. 1997, in: *IAU Symp. 182: Herbig-Haro Flows and the Birth of Stars*, eds. B. Reipurth & C. Bertout, Kluwer Academic Publishers, p. 241
- Campbell, C. G., *Magnetohydrodynamics in Binary Stars*, (Kluwer Academic Publishers, Dordrecht, 1977)
- Carvalho, J. C., O'Dea, C. P. 2002, *Ap. J. S.* **141**, 337
- Casse, F., Keppens, R. 2002, *Ap. J.* **581**, 988
- Casse, F., Keppens, R. 2004, *Ap. J.* **601**, 90
- Cen, R. 1992, *Ap. J. S.* **78**, 341

- Clarke, D. A., Norman, M. L., Burns, J. O. 1986, *Ap. J. L.* **331**, L63
- Crocker, M. M., Davis, R. J., Spencer, R. E., Eyres, S. P. S., Bode, M. F., Skopal, A. 2002, *MNRAS* **335**, 1100
- Crocker, M. M., Davis, R. J., Eyres, S. P. S., Bode, M. F., Taylor, A. R., Skopal, A., Kenny, H. T. 2001, *MNRAS* **326**, 781
- Crudace, R., Voges, W., Böhringer, H., Collins, C. A., Romer, A. K., MacGillivray, H., Yentis, D., Schuecker, P., Ebeling, H., De Grandi, S. 2002, *Ap. J. S.* **140**, 239
- De Villiers, J.P., Hawley, J. F., Krolik, J. H., Hirose S. 2004, *submitted to Ap. J.*, astro/ph 0407092
- Dopita, M. A., Sutherland, R. S., *Astrophysics of the diffuse universe*, (Springer, Berlin, New York, 2003)
- Dumm, T., Schild, H. 1998, *New Astron.* **3**, 137
- Ezuka, H., Ishida, M., Makino, F. 1998, *Ap. J.* **499**, 388
- Eyres, S. P. S., Bode, M. F., Skopal, A., Crocker, M. M., Davis, R. J., Taylor, A. R. 2002, *MNRAS* **335**, 526
- Ferrari, A. 1998, *Ann. Rev. Astr. Ap.* **36**, 539
- Ferreira, J. 2004, in: *10th Aussois School on Stellar Physics 2000, Star Formation and the Physics of Young Stars*, eds. J. Bouvier & J.-P. Zahn
- Ferreira, J., Casse, F. 2004, *Ap. J.* **601**, 139
- Fleming, W. P. 1912, *Ann. Harv. Coll. Obs.* **56**, 165
- Frank, J., King, A. R., Raine, D. J., *Accretion power in Astrophysics*, (Cambridge University Press, 1985)
- Getman, K. V., Feigelson, E. D., Townsley, L., Bally, J., Lada, C. J., Reipurth, B. 2002, *Ap. J.* **575**, 354
- Hogg, F. S. 1932, *Pub. Astr. Soc. Pac.* **44**, 328
- Hogg, F. S. 1934, *Pub. Am. Astr. Soc.* **8**, 14
- Hollis, J. M., Michalitsianos, A. G., Kafatos, M., McAlister, H. A. 1985, *Ap. J.* **289**, 765
- Hollis, J. M., Lyon, R. G., Dorband, J. E., Feibelman W. A. 1985, *Ap. J.* **475**, 231
- Garcia, P. J. V., Cabrit, S., Ferreira, J., Binette, L. 2001, *A & A* **377**, 609
- Goodson, A.P., Böhm, K.-H., Winglee, R.M. 1999, *Ap. J.* **524**, 142
- Kato, Y., Mineshige, S., Shibata, K. 2004, *Ap. J.* **605**, 307
- Kellogg, E., Pedelty, J. A., Lyon, R. G. 2001, *Ap. J.* **563**, 151
- Kenyon, S. J., *The Symbiotic Stars*, (Cambridge University Press, 1986)
- Kirk, J. G., Melrose, D. B., Priest, E. R., *Plasma Astrophysics*, (Springer-Verlag, Berlin, Heidelberg, 1994)
- Kössl, D., Müller, E., 1988, *A & A* **206**, 204
- Krasnopolsky, R., Li, Z.-Y., Blandford, R. D. 1999, *Ap. J.* **526**, 631

- Krasnopolsky, R., Li, Z.-Y., Blandford, R. D. 2003, *Ap. J.* **595**, 631
- Krause, M. 2001, in: *High Performance Computing in Science and Engineering 2001*, eds. E. Krause, W. Jäger, Springer, Berlin, Heidelberg, New York, p. 329
- Krause, M. 2002, *On the interaction of jets with the dense medium of the early universe*, *PhD Thesis*, University of Heidelberg
- Krause, M., Camenzind, M. 2001, *A & A* **380**, 789
- Kuiper, G. P. 1940, *Pub. Am. Astr. Soc.* **10**, 57
- Landau, L. D., Lifshitz, E. M., *Course of Theoretical Physics, Volume 6, Fluid Mechanics*, (Pergamon Press, 1959)
- Lasota, J.-P. 2001, *New A. R.* **45**, 449
- Maran, S. P., Michalitsianos, A. G., Oliverson, R. J., Sonneborn, G. 1991, *Nature* **350**, 404
- Mikolajewski, M., Mikolajewska, J., Tomov, T., 1987, *AP & SS* **131**, 733
- Mirabel, I. F., Rodriguez, L. F. 1999, *ARA & A* **37**, 409
- Meier, S. R., Rudy, R. J., Lynch, D. K., Rossano, G. S., Erwin, P. , Puetter, R. C. 1996, *A. J.* **111**, 476
- Menzel, D. H. 1946, *Physica* **12**, 768
- Merrill, P. W. 1919, *Pub. Astr. Soc. Pac.* **31**, 305
- Merrill, P. W. 1936, *Ap. J.* **83**, 272
- Merrill, P. W., Burwell, C. G. 1943, *Ap. J.* **98**, 153
- Merrill, P. W., Humason, M. L. 1932, *Pub. Astr. Soc. Pac.* **44**, 56
- Mundt, R., Brugel, E. W., Bührke, T. 1987, *Ap. J.* **319**, 275
- Mürset, U., Schmid, H. M. 1999, *A & AS* **137**, 473
- Norman, M. L., Smarr, L., Winkler, K.-H. A., Smith, M. D. 1982, *A & A* **113**, 285
- Norman, M. L., Winkler, K.-H. A., Smarr, L. 1983, in: *Astrophysical Jets*, eds. A. Ferrari & A. G. Pacholchik, Dordrecht: Reidel, p.227
- Paczyński, B., Wiita, P. J. 1980, *A & A* **88**, 23
- Paresce, F., Hack, W. 1994, *A & A* **287**, 154
- Pelletier, G., Pudritz, R.E. 1992, *Ap. J.* **394**, 117
- Plaskett, H. H. 1928, *Pub. DAO Victoria* **4**, 119
- Popham, R., Sunyaev, R. A. 2001, *Ap. J.* **547**, 355
- Pottasch, S. R., *Planetary nebulae : a study of late stages of stellar evolution*, (Astrophysics and space science library v. 107, D. Reidel Publishing Company, Dordrecht, 1984)
- Pudritz, R.E., Norman, C.A. 1986, *Ap. J.* **301**, 571
- Rayburn, D. R. 1977, *MNRAS* **179**, 603

- Rybicki, G. B., Lightman, A. P., *Radiative Processes in Astrophysics*, (John Wiley & Sons, New York, 1979)
- Sanduleak, N., Stephenson, C. B. 1973, *Ap. J.* **185**, 899
- Saxton, C. J., Bicknell, G. V., Sutherland, R. S. 2002, *Ap. J.* **579**, 176
- Scheck, L., Aloy, M. A., Marti, J. M., Gomez, J. L., Müller, E. 2002, *MNRAS* **331**, 615
- Schmid, H. M., Kaufer, A., Camenzind, M., Rivinius, Th., Stahl, O., Szeifert, T., Tubbesing, S., Wolf, B. 2001, *A & A* **377**, 206
- Shakura, N. I., Sunyaev, R. A. 1973, *A & A* **24**, 337
- Shore, S. N., Aufdenberg, J. P., Michalitsianos, A. G. 1994, *A. J.* **108**, 671
- Shu, F. H., *The Physics of Astrophysics*, (University Science Books, Mill Valley, 1992)
- Shull, J. M., van Steenberg, M. 1982, *Ap. J. S.* **48**, 95
- Steffen, W., Gomez, J. L., Williams, R. J. R., Raga, A. C., Pedlar, A. 1997, *MNRAS* **286**, 1032
- Steinacker, A., Papaloizou, J. C. B. 2002, *Ap. J.* **571**, 413
- Stone, J. N., Norman, M. L. 1993, *Ap. J.* **413**, 198
- Soker, N., Lasota, J.-P. 2004, submitted to *A & A*
- Soker, N., Regev, O. 2003, *A & A* **406**, 603
- Sokoloski, J. L., Bildsten, L. 1999, *Ap. J.* **517**, 919
- Sokoloski, J. L., Bildsten, L., Ho, W. C. G. 2001, *MNRAS* **326**, 553
- Solf, J., Ulrich, H. 1985, *A & A* **148**, 274
- Stencel, R. E., Michalitsianos, A. M., Kafatos, M., Boyarchuk, A. A. 1982, *Ap. J. L.* **253**, L77
- Sutherland, R. S., Dopita, M. A. 1993, *Ap. J. S.* **88**, 253
- Tanuma, S., Yokoyama, T., Kudoh, T., Shibata, K. 2003, *Ap. J.* **582**, 215
- Taylor, A. R., Seaquist, E. R., Mattei, J. A. 1986, *Nature* **319**, 38
- Thiele, M. 2000, *Numerical simulations of protostellar jets*, *PhD Thesis*, University of Heidelberg
- Tomov, T., Kolev, D. 1997, *A & AS* **122**, 43
- Tomov, T., Kolev, D., Georgiev, L., Zamanov, R., Antov, A., Bellas, Y. 1990, *Nature* **346**, 637
- Ustyugova, G. V., Lovelace, R. V. E., Romanova, M. M., Colgate, S. A. 2000, *Ap. J.* **541**, L21
- Ustyugova, G. V., Koldoba, A. V., Romanova, M. M., Chechetkin, V. M., Lovelace, R. V. E. 1995, *Ap. J.* **439**, L39
- Ustyugova, G. V., Koldoba, A. V., Romanova, M. M., Chechetkin, V. M., Lovelace, R. V. E. 1999, *Ap. J.* **516**, 221
- Verner, D. A., Ferland, G. J. 1996, *Ap. J. S.* **103**, 467
- Voigt, H. H., *Abriss der Astronomie*, (BI-Wiss.-Verlag, Mannheim, Wien, Zürich, 1991)
- Wallerstein, G. 1986, *Pub. A.S.P.* **98**, 118

Warner, B., *Cataclysmic Variable Stars*, (Cambridge University Press, 1995)

Williams, A. G., Gull, S. F. 1985, *Nature* **313**, 34

Ziegler, U., Yorke, H. 1997, *Comp. Phys. Comm.* **101**, 54

Ziegler, U. 2002, *A & A* **386**, 331

Danksagung

Zu guter Letzt möchte ich mich bei allen bedanken, die mich und diese Arbeit unterstützt haben, die in der einen oder anderen Art und Weise zum Gelingen dieser Arbeit beigetragen haben:

Ein herzliches Dankeschön geht an ...

- ... Max Camenzind* — *für die Aufnahme als Doktorand in seiner Gruppe, dafür, daß er dieses hochinteressante Thema bereitstellte, für seine allgegenwärtige Hilfe und die vielen, stets erhellenden Diskussionen*
- ... Hans Martin Schmid* — *dafür, daß er mich auf das spannende Forschungsgebiet der Symbiotischen Sterne stieß, für das Erstellen des Zweitgutachtens, für viele Anregungen, um diese Arbeit zu verbessern, und dafür, daß er immer einen guten Grund lieferte, das wunderschöne Zürich zu besuchen*
- ... meine Eltern* — *für einfach alles, besonders dafür, daß sie mich immer unterstützten und mir das Studium in Physik und Astronomie ermöglichten*
- ... meine Frau Almut* — *für die wundervollen, gemeinsamen Jahre, in denen sie mir, meiner Arbeit und meinen Arbeitszeiten immer größtes Verständnis entgegenbrachte*
- ... José* — *dafür, daß er immer die Maschine in der Gruppe am Laufen hielt – und für seine badische Unterstützung gegen schwäbische Infiltration in unsere Gruppe (“Gell, Volker??”) :-)*
- ... Martin* — *für seine unzähligen und geduldigen Einführungen in NIRVANA und Jetphysik*
- ... die gesamte Theorie-Gruppe* — *für ihre familiäre Atmosphäre*
- ... die Mitarbeiter der Landessternwarte* — *für das sehr gute Arbeitsklima; besonders an Otmar Stahl für nicht-wenige Hilfestellungen, wenn die Rechner oder Drucker nicht das machten, was sie sollten bzw. was ich wollte*
- ... und alle Kantinengänger* — *denn geteiltes Leid ist halbes Leid :-)*

